Mathematical Modelling in Sedimentation. Lecture Notes, Escuela de Primavera de Análisis Numérico (EPANUM 2019), Universidad de Concepción, 21-25 October 2019 (57 pp).

5 authors, including:

Raimund Bürger
Universidad de Concepción, Concepción, Chile
281 PUBLICATIONS   **5,556** CITATIONS

SEE PROFILE

Julio Careaga
University of Bío-Bío
24 PUBLICATIONS   **121** CITATIONS

SEE PROFILE

Victor Osores
Universidad Católica del Maule
9 PUBLICATIONS   **28** CITATIONS

SEE PROFILE

Luis M Villada
University of Bío-Bío
33 PUBLICATIONS   **312** CITATIONS

SEE PROFILE

MATHEMATICAL MODELLING IN SEDIMENTATION[*]

RAIMUND BÜRGER[A], JULIO CAREAGA[B], STEFAN DIEHL[B], VÍCTOR OSORES[A],
AND LUIS MIGUEL VILLADA[C]

ABSTRACT. Mathematical models that describe continuous thickening that may be employed for simulation, design and control are usually given as nonlinear, time-dependent partial differential equations that in one space dimension include strongly degenerate convection-diffusion-reaction equations with discontinuous coefficients, and in two or more dimensions, coupled flow-transport problems or first-order systems of balance equations arising from a shallow water approach. It is the purpose of these notes, subdivided into three sections, to provide a survey of published results on models of batch and continuous sedimentation of ideal and flocculated suspensions (Section 1), to outline a recent theory of sedimentation of ideal suspensions in vessels with variable cross-sectional area (in particular, cones) and its application to solving the problem of flux identification (Section 2), and to review mathematical models of polydisperse sedimentation, including a recently formulated multilayer shallow water formulation (Section 3).

1. Introduction

1.1. **Mathematical engineering research in sedimentation.** The topic of research on sedimentation is motivated in Chile, and some other mining countries mostly located on the southern hemisphere, by applications to mineral processing. In Chile, the most import economic activity is mining of copper. The deposits typically contain 0.4% to 1% of copper. One important step of the production of copper consists in the process of flotation, which roughly speaking means that finely ground copper ores are mixed with water and a reagent that turns the metalliferous (valuable) particles hydrophobic while the (valueless) so-called gangue particles are hydrophilic. These properties are exploited for the concentration of copper ores by flotation, that is, bubbles are injected into the pulp to which the hydrophobic particles attach, and which eventually form a foam (froth) that is skimmed and further processed for the concentration of copper. On the other hand, this process produces a tremendous amount of tailings, that is a suspension of water with finely divided solid (gangue) particles. Most copper mines are located in desert areas where water is a scarce resource, and therefore one wishes to recover the largest amount possible of process water from the tailings. This is done by specialized settling tanks, so-called thickeners, also called clarifier-thickeners that are operated continuously (see Figure 1). Mathematical models are urgently required for the description, simulation, design and control of such equipment.

[A]CI^{2}MA and Departamento de Ingeniería Matemática, Facultad de Ciencias Físicas y Matemáticas, Universidad de Concepción, Casilla 160-C, Concepción, Chile. E-Mail: `rburger@ing-mat.udec.cl`, `victorosores@udec.cl`.

[B]Centre for Mathematical Sciences, Lund University, P.O. Box 118, S-221 00 Lund, Sweden. E-Mail: `julio.careaga@math.lth.se`, `stefan.diehl@math.lth.se`.

[C]Departamento de Matemática, Facultad de Ciencias, Universidad del Bío-Bío, Casilla 5-C, Concepción, Chile. E-Mail: `lvillada@ubiobio.cl`.

FIGURE 1. Thickeners at Escondida Copper Mine, Chile, whose purpose is the recovery of water from tailings suspensions after flotation.

The research on mathematical model of sedimentation at Universidad de Concepción dates back to the 1970s, and was initiated by Fernando Concha, now professor emeritus, and for a long time academic at the Department of Metallurgical Engineering of the Faculty of Engineering at Universidad de Concepción. The involvement of mathematicians started in the early 1980s with the collaboration of María Cristina Bustos, then an academic at the Institute of Mathematics and later at the Department of Mathematical Engineering of UdeC. She prepared her doctoral thesis, finished in 1984, under the guidance of Wolfgang L. Wendland, then a professor of mathematics at Technische Hochschule Darmstadt, Germany. W.L. Wendland assumed a new position at Universität Stuttgart, Germany, in 1986. The author joined his group as a doctoral student in 1993, and finished his doctoral studies in 1996. During this time, and later on in various positions as a research assistant, he started to collaborate also with the group at UdeC, and made contributions of his own on the topic of models of sedimentation and related solid-fluid operations. Eventually he joined UdeC as a Full Professor of the Department of Mathematical Engineering in 2005.

Very similar models describe the operation of secondary settling tanks (SSTs) that are part of the so-called activated sludge process (ASP), which is the main process of operation of wastewater treatment (WWT) plants (WWTPs; nowadays called water resource recovery facilities (WRRFs)). Thus, research on models of sedimentation also covers these applications, and the author has fruitfully collaborated in this direction with the group of professor Stefan Diehl at Lund University, Sweden, and further collaborators.

It is the purpose of these to outline some recent contributions to the development, numerical solution, and calibration of models of sedimentation of ideal, flocculated, and polydisperse suspensions, where the simplest case, namely that of batch settling of monodisperse suspension, is illustrated in Figure 3. We are especially interested in models of batch and continuous sedimentation processes of ideal, flocculated and polydisperse suspensions described by spatially one-dimensional,
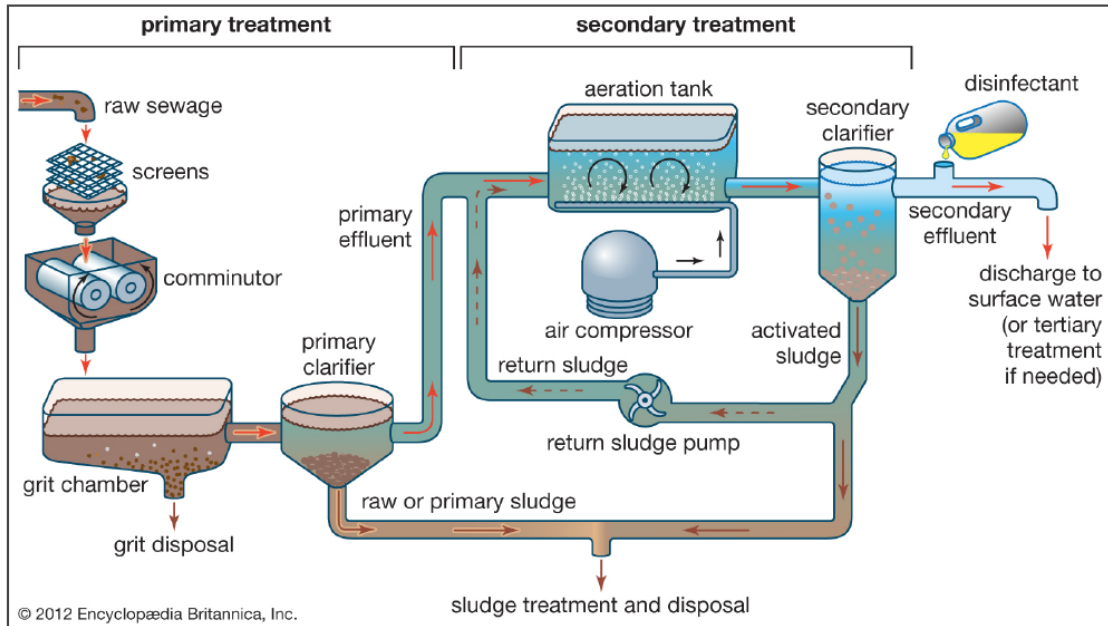
activated-sludge method

FIGURE 2. The Activated Sludge Process (ASP) in the application of wastewater treatment/water resource recovery.

time-dependent partial differential equations (PDEs). The models are designed to capture basic settling, consolidation, segregation and related processes under continuous feed and discharge operations. The mathematical interest in these models arises from non-standard "ingredients" (such as degenerate diffusion, discontinuous coefficient functions, and hyperbolicity problems) that require original mathematical research in analysis and numerical analysis. Results ensure, for example, the well-posedness of mathematical models (that is, the existence, uniqueness, and continuous dependence on data of a solution) and convergence of numerical schemes. Thus, over the years it has been possible to construct a closed model framework suitable for upscaling laboratory data in applications. Tools for the design, simulation and control of thickeners, clarifiers, and related equipment have been developed. A more recent focus has been placed on parameter identification problems and extensions to flotation and reactive settling.

1.2. **Historical comments.** To put the original research problem into the proper historical perspective of the engineering application, we first mention that extensive historical accounts are provided in [1,2]. The exploitation of the difference in density between solid particles and fluid for operations of washing ores can be traced back at least to the ancient Egyptians [3]. The use of settling tanks, operated in a batch or semi-continuous manner, for processes that can now be identified as classification, clarification and thickening, was described in detail in Georgius Agricola's book *De Re Metallica*, first published in 1556 [1,2], see Figure 4. The most important technological invention that would rationalize the settling process is the continuous thickener, introduced by J.V.N. Dorr, a chemist, cyanide mill owner, consulting engineer and plant designer, in the early twentieth century [4–6] (see Figure 5). A continuous thickener is essentially a cylindrical settling tank into which the feed suspension to be separated is fed continuously, the sediment forming by
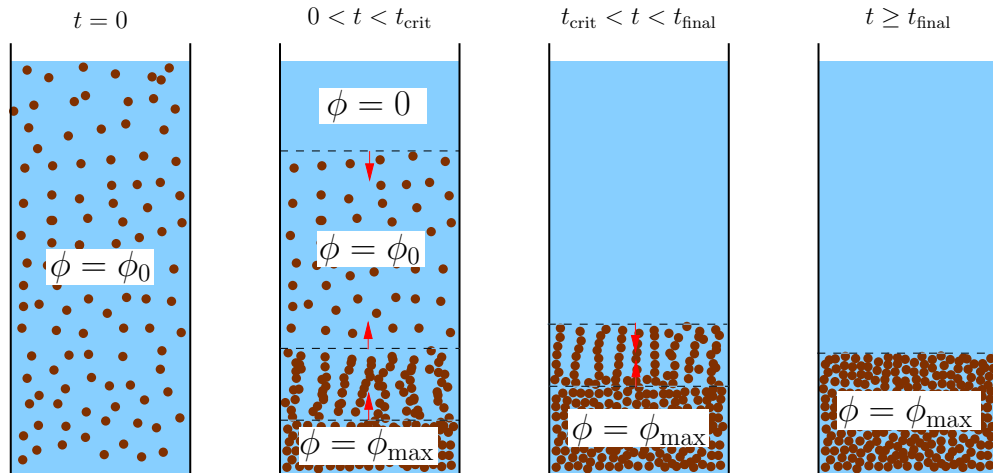
FIGURE 3. Schematic of the sedimentation of a monodisperse suspension of small solid particles in a viscous fluid: (left) suspension at initial solids volume fraction ϕ_0, (middle left) formation of a clear liquid (supernatant) region ($\phi = 0$) and a densely packed sediment ($\phi = \phi_{\max}$), showing a descending suspension-supernate interface and a rising sediment-suspension interface, which meet at a critical time t_{crit}, (middle right) compaction of the sediment after critical time t_{crit}, but before the system has attained steady state, (right) final steady state with particles at rest and sediment at maximum packing solids volume fraction $\phi_{\max}$.
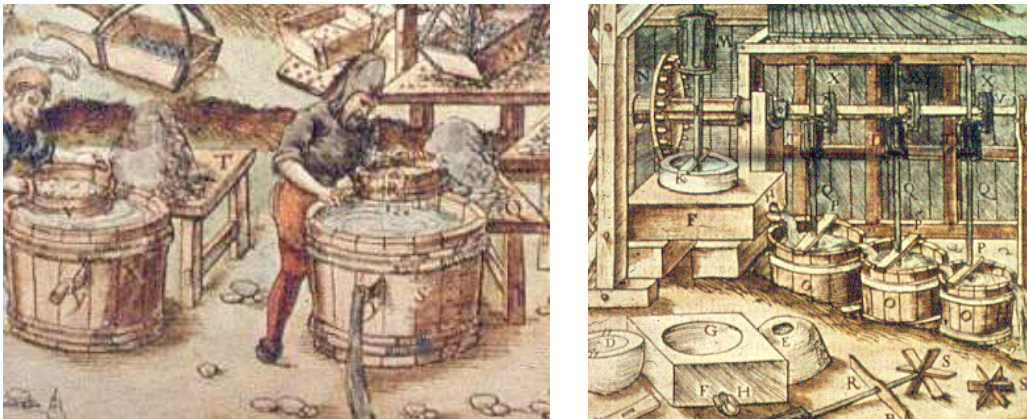

FIGURE 4. Sieving and washing operations illustrated by G. Agricola (*De Re Metallica*, Freiberg, Saxony, 1556).

settling of particles is removed continuously, and the clear liquid produced is removed by a circumferential launder (see Figure 6). This design is widely used today in mineral processing and in secondary settling tanks in wastewater treatment. The invention of the clarifier-thickener was soon followed by efforts to mathematically model its operation. Coe and Clevenger recognized in 1916 [7] that understanding the dynamics of the batch settling process of a suspension at different solids concentrations is fundamental for effective thickener design and control. Their drawing of a
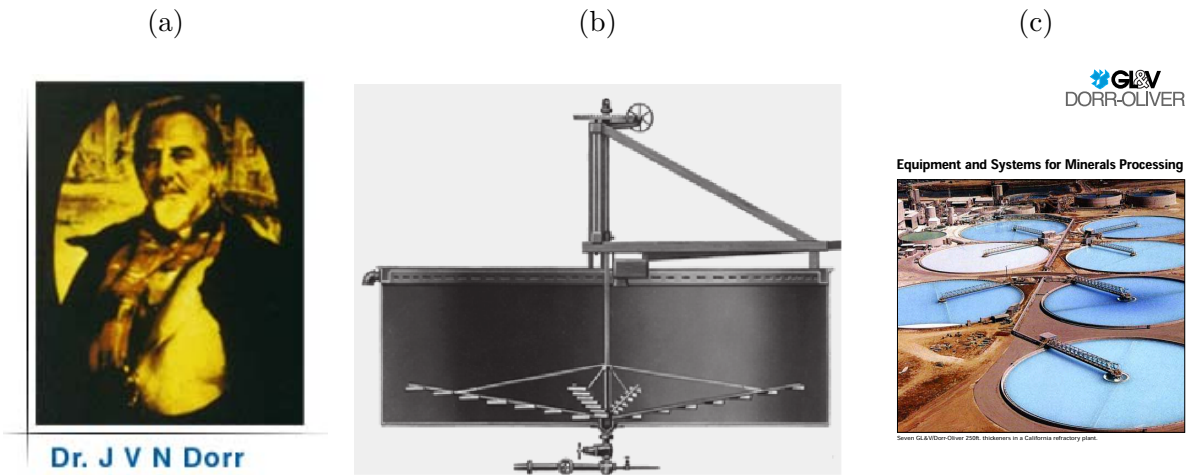
FIGURE 5. (a) John Van Nostrand Dorr (1872–1962), inventor of the continuous thickener, (b) illustration of the Dorr thickener (from [6]), (c) modern advertisement of a Dorr-Oliver thickener.
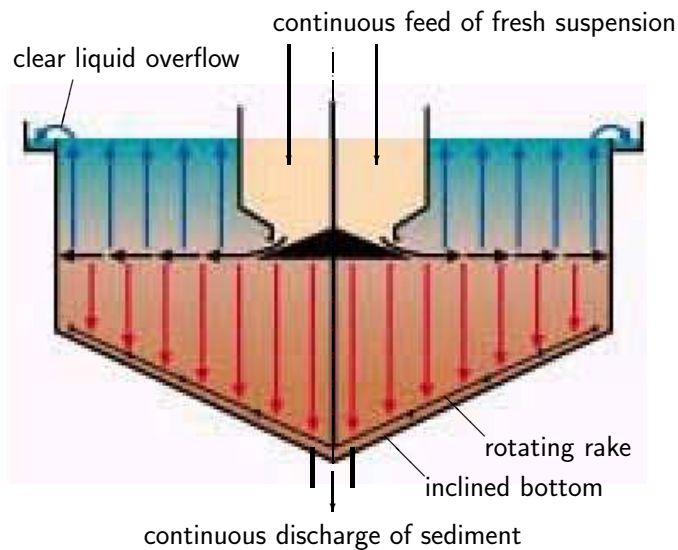
FIGURE 6. Schematic of a continuously operated clarifier-thickener.

succession of snapshots of a settling column shown in our Figure 7 has become the leading paradigm of batch settling in a column.

1.3. **Hindered settling.** The starting point of the mathematical modelling of sedimentation is the well-known Stokes formula [8], which states that the settling velocity of a sphere of size (diameter) d and density ρ_s in an unbounded fluid of density ρ_f and viscosity μ_f is given by

$$v_\infty = \frac{(\rho_s - \rho_f)d^2}{18\mu_f}, \tag{1.1}$$

FIGURE 7. Settling experiments conducted by Coe and Clevenger [7].

where g denotes acceleration of gravity. The settling velocity of a particle in a concentrated suspension is, however, smaller than (1.1) due to the hindrance exerted by the presence of other particles. This effect can be expressed as an increase in viscosity of the suspension. Explicit formulas describing the phenomenon of hindered settling are of the type
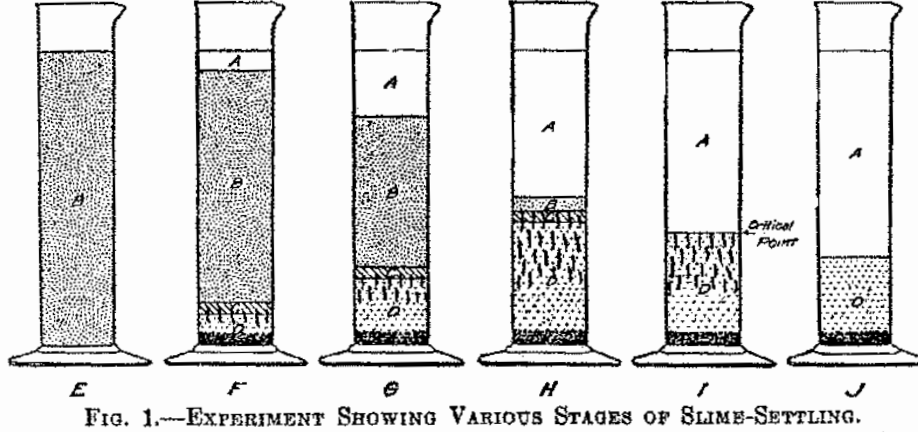
$$v_{\mathrm{settl}} = v_\infty \mathcal{V}(\phi)$$

where the hindered settling factor $\mathcal{V} = \mathcal{V}(\phi)$ should satisfy $\mathcal{V}(0) = 1$, $\mathcal{V}(\phi_2) < \mathcal{V}(\phi_1)$ for for $\phi_1 < \phi_2$ and $\mathcal{V}(\phi_{\max}) = 0$. A formula for the dilute limit $\phi/\phi_{\max} \ll 1$ was derived more than a century ago by A. Einstein [9], and in the 1940s,

$$v_{\mathrm{settl}} = v_\infty \mathcal{V}(\phi)$$

was postulated for both dilute and concentrated suspensions (see, e.g., [10–12]).

1.4. **Kinematic model of sedimentation.** We now formulate a simple PDE-based model of sedimentation based on the conservation of mass of the solid and liquid components. To this end we consider the solids and the fluid as superimposed continuous phases associated with velocities v_{s} and v_{f}. It is then assumed that the relative velocity (or slip velocity) $v_{\mathrm{r}} := v_{\mathrm{s}} - v_{\mathrm{f}}$ is given by a constitutive equation

$$v_{\mathrm{r}} = v_\infty V(\phi),$$

where by kinematic side considerations (not detailed here) the hindered settling factor $V(\phi)$ is related to $\mathcal{V}(\phi)$ introduced above by $\mathcal{V}(\phi) = (1 - \phi)V(\phi)$. The algebraic form of $V(\phi)$ depends on the material under consideration, and the generic expected behaviour is $V(0) = 1$, $V(\phi_{\max} = 1) = 0$, and $V'(\phi) < 0$.

To formulate the governing partial differential equation, we define the volume-average velocity

$$q = \phi v_{\mathrm{s}} + (1 - \phi)v_{\mathrm{f}}.$$

Then the one-dimensional conservation of mass partial differential equations for the solids phase, occupying volume fraction ϕ, and the liquid phase, occupying volume fraction $1 - \phi$, can be written
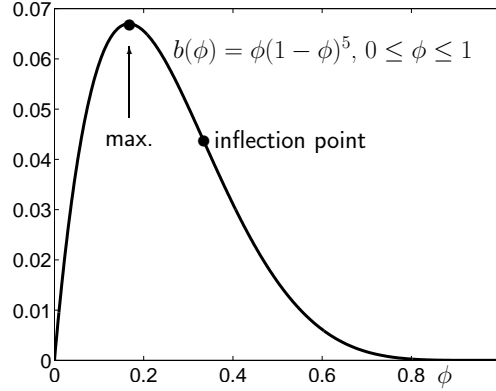
FIGURE 8. Richardson-Zaki flux plot with $n = n_{\mathrm{RZ}} = 5$.

as

$$\frac{\partial \phi}{\partial t} + \frac{\partial}{\partial x}(\phi v_{\mathrm{s}}) = 0, \quad \frac{\partial (1 - \phi)}{\partial t} + \frac{\partial}{\partial x}\big((1 - \phi)v_{\mathrm{f}}\big) = 0.$$

Observe that summing both balance equations we obtain $\partial q/\partial x = 0$, that is, in the absence of sources and sinks q is constant: for a closed column: $q = 0$; and otherwise q is controllable: $q = q(t)$. On the other hand, from the definitions of v_{r} and q we derive that the solids flux ϕv_{s} can be written as

$$\phi v_{\mathrm{s}} = \phi q + \phi(1 - \phi)v_{\mathrm{r}}.$$

Thus, we arrive at the final one-dimensional equation

$$\frac{\partial \phi}{\partial t} + \frac{\partial}{\partial x}\big(\phi q + b(\phi)\big) = 0,$$

where we define the so-called batch flux density function

$$b(\phi) = \phi(1 - \phi)v_{\mathrm{r}} = v_{\infty}\phi(1 - \phi)V(\phi).$$

A common semi-empirical expression is Richardson-Zaki formula [13]:

$$b(\phi) = \begin{cases} v_{\infty}\phi(1 - \phi)^{n_{\mathrm{RZ}}} & \text{for } 0 \leq \phi \leq \phi_{\max}, \\ 0 & \text{otherwise.} \end{cases}$$

See Figure 8 for an example with $n_{\mathrm{RZ}} = 5$.

1.5. **Batch settling of an ideal suspension: some mathematical aspects.** The previous discussion elucidates that the proper mathematical frame of the kinematic theory of sedimentation are first-order, nonlinear, scalar conservation laws. For instance, we may consider the case of batch settling. According to the theory of first-order scalar conservation laws, solution values of the first-order conservation law

$$\frac{\partial \phi}{\partial t} + \frac{\partial b(\phi)}{\partial x} = 0, \quad \phi(x, 0) = \phi_0(x) \tag{1.2}$$

propagate along straight lines with slope $b'(\phi)$ in an x versus t diagram. If b depends nonlinearly on ϕ (as is the case in models of sedimentation), then the characteristics will in general intersect after
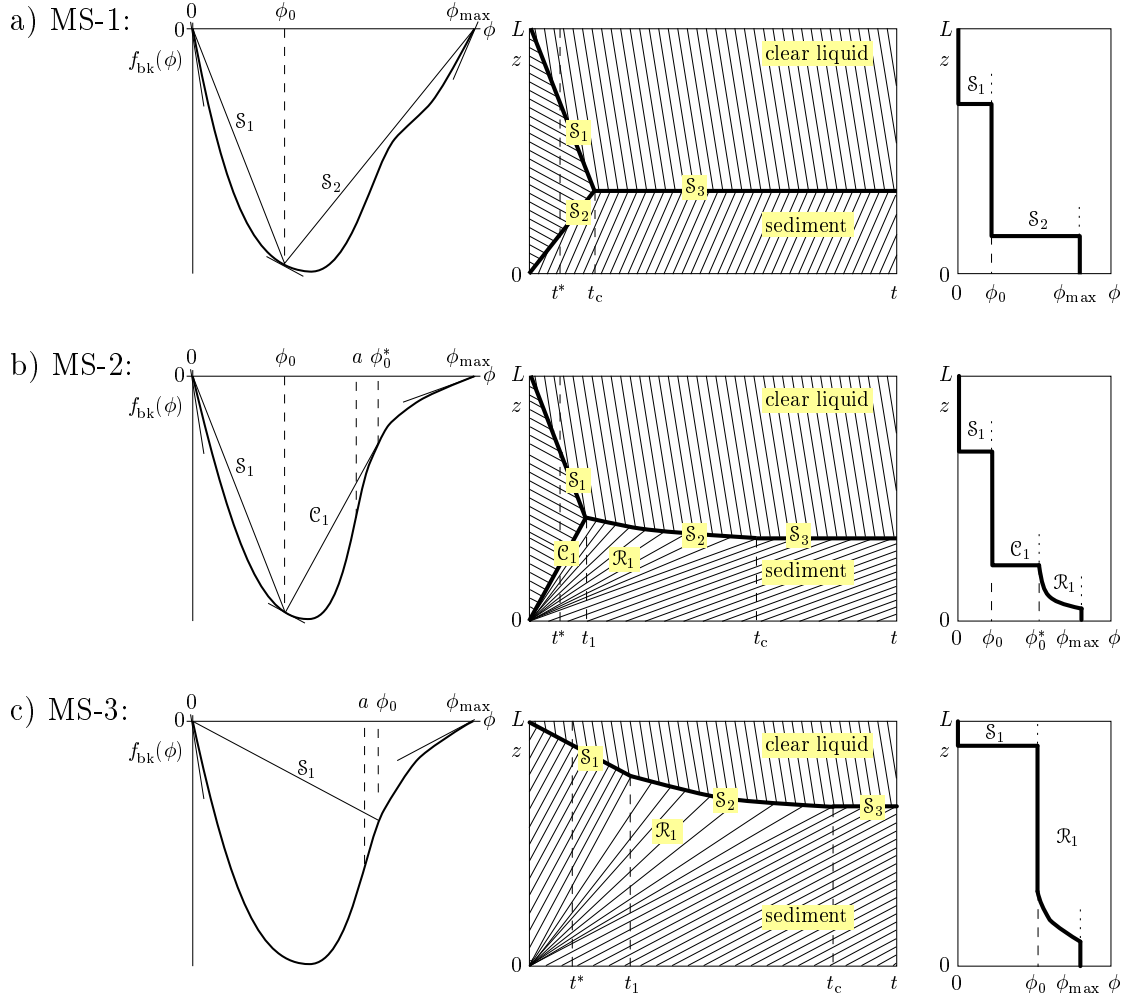
FIGURE 9. Construction of solutions to the problem of batch sedimentation of an ideal suspensions, after [14].

finite time, and the solution becomes discontinuous. It is well known that a discontinuity between two adjacent ϕ-values ϕ^- and ϕ^+ propagates at the following speed (Rankine-Hugoniot condition):

$$s = \frac{b(\phi^-) - b(\phi^+)}{\phi^- - \phi^+} = \text{slope of chord } \overline{\left(\phi^-, b(\phi^-)\right), \left(\phi^+, b(\phi^+)\right)}.$$

Such a discontinuity is, moreover, admissible (and is then called a *shock*) if the chord that joins the points $(\phi^-, b(\phi^-))$ and $(\phi^+, b(\phi^+))$ in an $b(\phi)$ versus ϕ plot runs completely above the graph of $b(\phi)$ if $\phi^+ < \phi^-$ and completely below the graph of $b(\phi)$ if $\phi^- < \phi^+$ (this is a consequence of Oleinik's jump entropy condition.) The construction of solutions is illustrated in Figure 9. See [14] for more details.

It was Kynch's specific contribution [15] that he explicitly *solved* the governing equation (1.2) under the assumption $v_s = v_\infty V(\phi)$, for initially constant concentrations. In mathematical terms, if the function b has support on the interval $(0, \phi_{\max})$, then the settling of an initially homogeneous

suspension of concentration $\phi_0 \in (0, \phi_{\max})$ in a column of depth L can be described by the initial-value problem (1.2) defined by the piecewise constant initial datum

$$\phi(x, 0) = \begin{cases} 0 & \text{for } x < 0, \\ \phi_0 & \text{for } 0 < x < L, \\ \phi_{\max} & \text{for } x > L \end{cases} \tag{1.3}$$

corresponding to two adjacent Riemann problems. Kynch [15] applied the method of characteristics and resolving cases of intersection by discontinuities based on physical principles that agree with theoretically motivated entropy conditions to be introduced much later. One piece of insight these constructions could provide is the explanation why fairly dilute and concentrated suspensions would settle with a sharp interface and a zone of continuous transition of concentration separating the growing sediment from the bulk suspension; namely, the former situation gives rise to a kinematic shock (in ϕ) and the latter to a rarefaction.

Kynch's efforts were followed by systematic classifications of qualitatively different solutions to (1.2), (1.3) [16, 17]. Based on work by Ballou [18], K.S. Cheng [19] and Liu [20] (see [21]), Bustos and Concha [22] and Diehl [23] appropiately embedded these constructions into the theory of entropy solutions of a scalar conservation law with non-convex flux. The interest Kynch's theory immediately caused in mineral processing, wastewater treatment (where it has become known as the *solids flux theory*) and other applicative areas has been widely discussed in some reviews (e.g., [1, 24]). Clearly, to make this theory applicable to the settling of a given suspension one must assume that the factor $V = V(\phi)$ is known. The reliable identification of this factor or equivalently, of the function $b = b(\phi)$, from experimental data is a current research problem in itself [25–27], to which we come back in Section 2.7.

The model is very similar to the well-known Lighthill-Whitham-Richards (LWR) model for traffic flow. In fact, in textbooks on hyperbolic conservations, the LWR model forms the preferred example, since the typical flux $b(\phi) = \phi(1 - \phi)$ arising in that model is convex and allows for simpler construction of solutions, and the initial value problem (Riemann problem) for such an equation is easier to handle, than for the problem (1.2), (1.3) with b non-convex. The construction of solutions for the direct problem of (1.2) with piecewise constant initial data and constant ϕ_0 (1.3) is in any case well understood and for decades has formed standard material for engineering textbooks including [28, 29].

Summarizing we can say that the kinematic sedimentation model provides a complete description of the settling process ranging from the dilute limit to high concentrations. In particular, sharp interfaces such as the suspension-supernate interface, and under determined circumstances a sharp sediment-suspension interface are produced. Certain "easy" cases, such as the settling of an initially homogeneous suspension in a cylindrical vessel, allow the construction of an explicit solution in closed form since iso-concentration lines and characteristics coincide and are straight lines. Additional effects, such as sediment compressibility and variability of particle sizes and densities, are not considered.

1.6. **Sedimentation with compression.** In many applications in mineral processing, suspensions of finely divided solids are flocculated, that is by addition of a chemical reagent (flocculant) and applying suitable mechanisms such as shear, turbulence or mixing it is achieved that solid particles form clusters (flocs) that contain an amount of water, and that settle faster than individual particles, which accelerates the separation process. On the other hand, the flocs form a layer of compressible sediment (so-called self-weight consolidation) that is characterized by *curved* iso-concentration lines: in a height versus time plot, these lines emerge successively from the vessel bottom and eventually
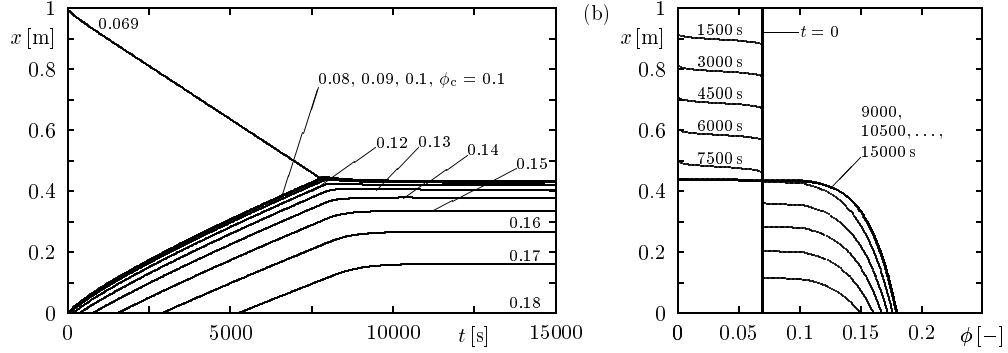
FIGURE 10. Numerical simulation of batch settling, corresponding to $q = 0$, $\phi_c = 0.1$, $\phi_0 = 0.07$, and $n = 5$ [49].

become horizontal as an equilibrium state is achieved. Clearly, such curved iso-concentration lines cannot be produced by solutions of the first-order conservation law (1.2). One way to describe the effect of sediment compressibility consists in extending the PDE (1.2) by a term that accounts for effective solid stress. The result of a rigorous derivation (see, e.g., [21,30,31]) can be formulated as follows.

It is assumed that there is a material-dependent critical concentration or gel point ϕ_c at which the solid particles (flocs) touch each other. If $\phi > \phi_c$, there is permanent contact between the flocs and solid stresses can be transmitted. We characterize the suspension by two model functions, $b(\phi)$ and the effective solid stress function $\sigma_e(\phi)$. The latter is assumed to satisfy

$$\sigma_e'(\phi) := \frac{\mathrm{d}\sigma_e(\phi)}{\mathrm{d}\phi} \begin{cases} = 0 & \text{for } \phi \leq \phi_c, \\ > 0 & \text{for } \phi > \phi_c; \end{cases}$$

a common semi-empirical formula with parameters to be determined is

$$\sigma_e(\phi) = \begin{cases} 0 & \text{for } \phi \leq \phi_c, \\ \sigma_0\big((\phi/\phi_c)^k - 1\big) & \text{for } \phi > \phi_c. \end{cases}$$

While for ideal suspensions (that do not exhibit sediment compressibility) we have

$$v_r = \frac{b(\phi)}{\phi(1 - \phi)},$$

we now obtain the solid-fluid relative velocity for sedimentation with compression as

$$v_r = \frac{b(\phi)}{\phi(1 - \phi)}\left(1 + \underbrace{\frac{1}{\Delta\varrho g\phi}\frac{\partial\sigma_e(\phi)}{\partial x}}_{\text{sediment compressibility term}}\right).$$

Inserting this expression into the solids continuity equation

$$\frac{\partial\phi}{\partial t} + \frac{\partial(\phi v_s)}{\partial x} = 0,$$

which in view of $\phi v_s \equiv \phi q + \phi(1 - \phi)v_r$ we may rewrite as

$$\frac{\partial\phi}{\partial t} + \frac{\partial}{\partial x}\big(\phi q + \phi(1 - \phi)v_r\big) = 0 \qquad \text{(in a closed vessel: } q = 0\text{)},$$
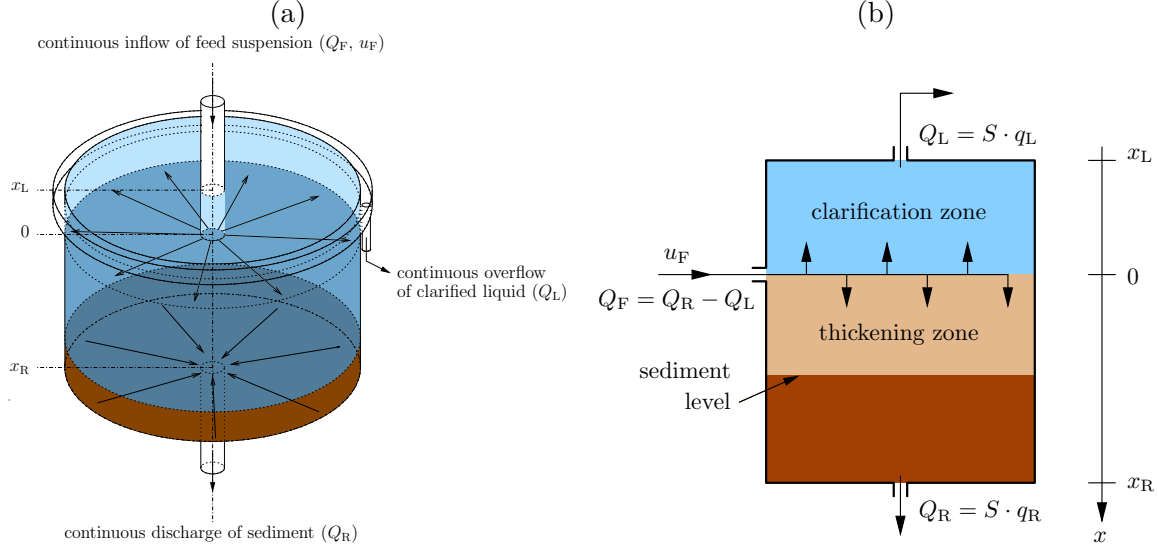
FIGURE 11. (a) Schematic view of a clarifier-thickener (CT; technical details are omitted), (b) one-dimensional idealized clarifier-thickener model.

we obtain

$$\frac{\partial \phi}{\partial t} + \frac{\partial}{\partial x}\big(\phi q + b(\phi)\big) = \frac{\partial}{\partial x}\left(\frac{b(\phi)\sigma'_\mathrm{e}(\phi)}{\Delta \varrho g \phi}\frac{\partial \phi}{\partial x}\right)$$
$$= \frac{\partial}{\partial x}\left(a(\phi)\frac{\partial \phi}{\partial x}\right) = \frac{\partial^2 A(\phi)}{\partial x^2},$$

(1.4)

where we define the diffusion coefficient

$$a(\phi) := \frac{b(\phi)\sigma'_\mathrm{e}(\phi)}{\Delta \varrho g \phi}\begin{cases} = 0 & \text{for } \phi \le \phi_\mathrm{c} \text{ and } \phi \ge \phi_\mathrm{max}, \\ > 0 & \text{for } \phi_\mathrm{c} < \phi < \phi_\mathrm{max} \end{cases}$$

and its primitive

$$A(\phi) := \int_0^\phi a(s)\,ds.$$

The final equation (1.4) is strongly degenerate parabolic, since

$$a(\phi)\begin{cases} = 0 & \text{for } \phi \le \phi_\mathrm{c} \text{ and } \phi \ge \phi_\mathrm{max}, \\ > 0 & \text{for } \phi_\mathrm{c} < \phi < \phi_\mathrm{max}. \end{cases}$$

A numerical example is shown in Figure 10.

1.7. **Clarifier-thickener models.** To extend the theory of batch settling of ideal or flocculated suspensions from batch settling (say, in a column) to continuous sedimentation in a clarifier-thickener, a new clarifier-thickener model for flocculated suspensions was formulated in [32] as a combination of the first-order models for ideal suspensions with the sedimentation-consolidation theory, which contributes a strongly degenerate diffusion term. The result is an initial-value problem of a strongly degenerate parabolic-hyperbolic partial differential equation, in which both the convective flux and the diffusion term depend discontinuously on spatial position (height or depth) x.
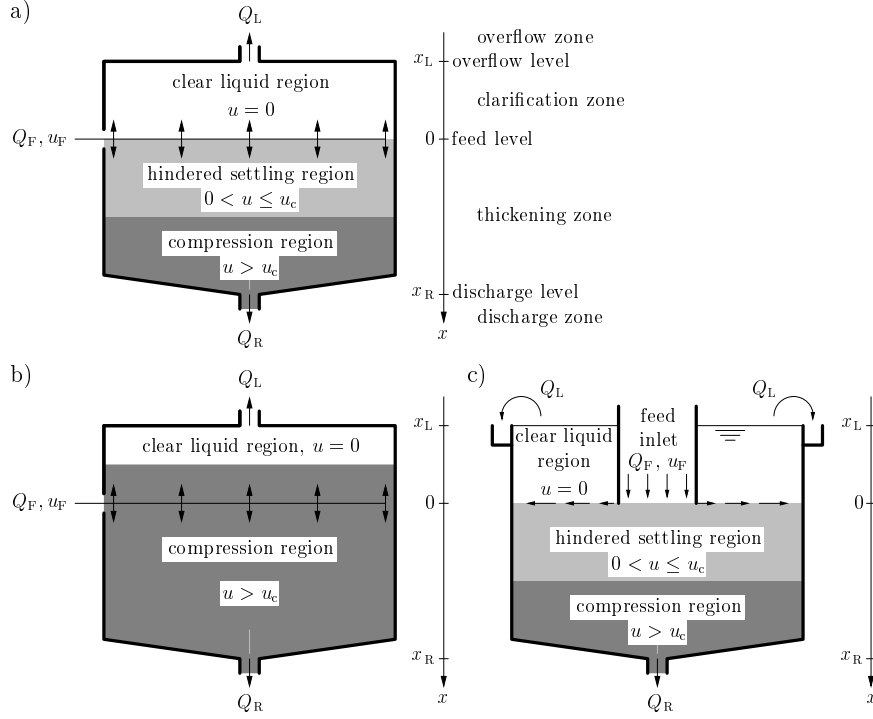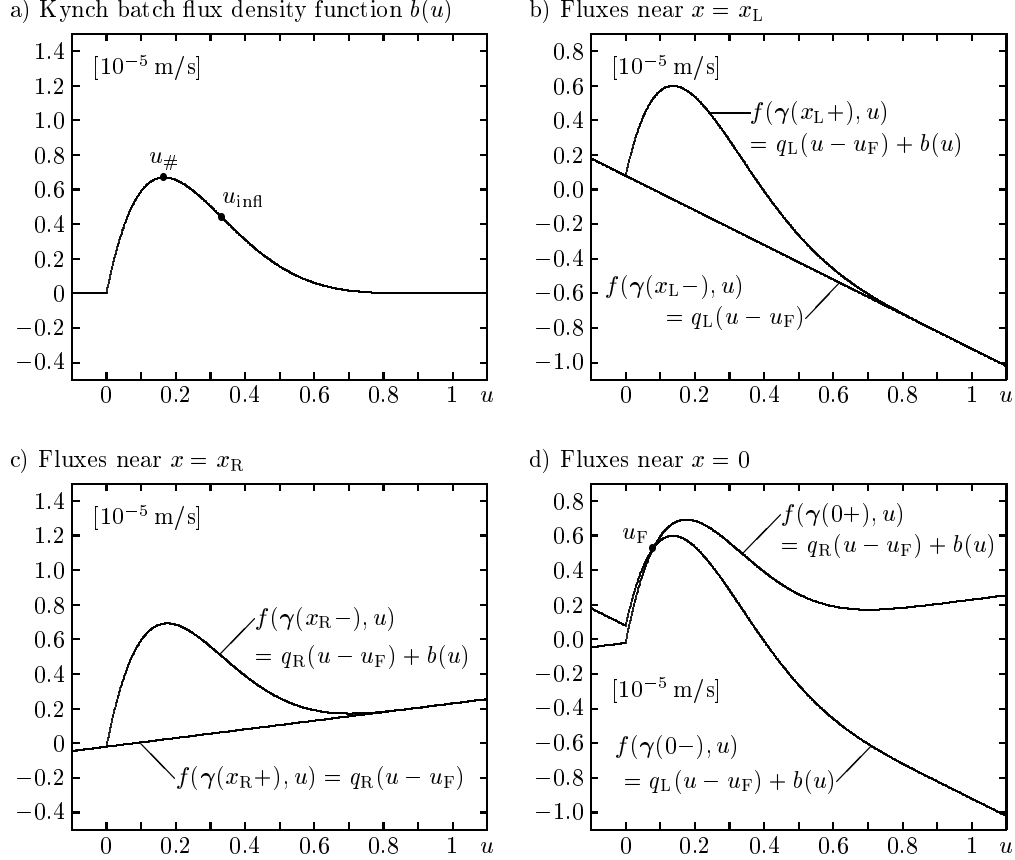
FIGURE 12. Modes of steady operation of a clarifier-thickener: (a) conventional operation (sediment level below feed level), (b) high-rate operation (sediment level above feed level), (c) variant of representation of conventional operation showing the feed inlet.

Clearly, solutions of such an equation are in general discontinuous. To outline the model, we consider a continuously operated axisymmetric clarifier-thickener vessel as drawn in Figure 11 (a). We denote by x a downward-increasing depth variable, and we assume that all flow variables depend on depth x and time t only. This means in particular that ϕ is assumed to be constant across each horizontal cross-section. We subdivide the clarifier-thickener vessel into four different zones: the thickening zone ($0 < x < x_R$), which is usually the unique zone considered in conventional analyses of continuous sedimentation, the clarification zone ($x_L < x < 0$) located above, the underflow zone ($x > x_R$) and the overflow zone ($x < x_L$). The vessel is continuously fed at depth $x = 0$, the feed level, with fresh feed suspension at a volume feed rate $Q_F(t) \geq 0$. The concentration of the feed suspension is $\phi_F(t)$. The prescribed volume underflow rate, at which the thickened sediment is removed from the unit, is $Q_R(t) \geq 0$. Consequently, the overflow rate is $Q_L(t) = Q_F(t) - Q_R(t)$, where we assume that the two control functions $Q_F(t)$ and $Q_R(t)$ are chosen such that $Q_L(t) > 0$. For a vessel with constant cross- sectional area S, we define the velocities $q_L(t) := -Q_L(t)/S$ and $q_R(t) := Q_R(t)/S$.

Of course, the solids concentrations in the underflow and overflow cannot be prescribed, and are part of the solution. Furthermore, we distinguish between the four above-mentioned zones in the clarifier-thickener, which are a property of the equipment modeled, and the clear liquid, hindered settling, and compression regions, in which a suspension at a given point of time has the concentrations zero, $0 < \phi \leq \phi_c$, and $\phi > \phi_c$, respectively. Thus, the time-dependent location of the regions is a property of a particular flow, that is, of the solution to the problem. Note that the

a) Kynch batch flux density function $b(u)$

b) Fluxes near $x = x_{\mathrm{L}}$

c) Fluxes near $x = x_{\mathrm{R}}$

d) Fluxes near $x = 0$

FIGURE 13. Plot of the function $g(x, \phi)$, after [45].

compression region is not confined to the thickening zone. These notions are stated to emphasize that the model includes two different stationary modes of operation that are usually distinguished in the applicative literature: conventional operation, as shown in Figures 12 (a) and (c), when the sediment level (where $\phi = \phi_{\mathrm{c}}$) is located below the feed level, and high-rate (also known as high-capacity) operation, when the feed suspension is pumped into the sediment, as seen in Figure 12 (b). The second case can be produced by letting the sediment level (and thus the compression region) rise into the clarification zone [33]. For sake of simplicity, we also neglect the action of the rake provided in most industrial thickeners, which rotates above the gently sloped floor of the thickener to move the concentrated sediment towards the discharge opening (references that handle this point include [34–38]).

To formulate the mathematical model, we collect the previous considerations and utilize the one-dimensional clarifier-thickener conceptual model of Figure 11 (b). It is assumed that the regions $x < x_{\mathrm{L}}$ and $x > x_{\mathrm{R}}$ correspond to the advective transport of the overflow and the underflow through pipes, in which the solid and the fluid move at the same velocity. Thus, v_{r} is "switched off" for $x < x_{\mathrm{L}}$ and $x > x_{\mathrm{R}}$, which means that the levels $x = x_{\mathrm{L}}$ and $x = x_{\mathrm{R}} = 1$ are transitions to convective transport. The final mathematical model is then based on considering two of the constants or time-dependent functions q_{R}, q_{L}, and $q_{\mathrm{F}} := q_{\mathrm{R}} - q_{\mathrm{L}}$, as well as the feed concentration

ϕ_{F}, as control variables. The model is then defined by the partial differential equation

$$\frac{\partial \phi}{\partial t} + \frac{\partial g(x, \phi)}{\partial x} = \frac{\partial}{\partial x}\left(\gamma_1(x)\frac{\partial A(\phi)}{\partial x}\right), \quad x \in \mathbb{R}, \quad t > 0, \tag{1.5}$$

along with the initial condition

$$\phi(x, 0) = \phi_0(x), \quad x \in \mathbb{R},$$

and the following definition of the convective flux:

$$g(x, \phi) := \begin{cases} q_{\mathrm{L}}(\phi - \phi_{\mathrm{F}}) & \text{for } x < x_{\mathrm{L}}, \\ q_{\mathrm{L}}(\phi - \phi_{\mathrm{F}}) + b(\phi) & \text{for } x_{\mathrm{L}} < x < 0, \\ q_{\mathrm{R}}(\phi - \phi_{\mathrm{F}}) + b(\phi) & \text{for } 0 < x < x_{\mathrm{R}}, \\ q_{\mathrm{R}}(\phi - \phi_{\mathrm{F}}) & \text{for } x > x_{\mathrm{R}}. \end{cases}$$

If we define the discontinuous parameters $\boldsymbol{\gamma} := (\gamma_1, \gamma_2)$, where

$$\gamma_1(x) := \begin{cases} 1 & \text{for } x \in (x_{\mathrm{L}}, x_{\mathrm{R}}), \\ 0 & \text{otherwise}, \end{cases}, \qquad \gamma_2(x) := \begin{cases} q_{\mathrm{L}} < 0 & \text{for } x < 0, \\ q_{\mathrm{R}} > 0 & \text{for } x > 0, \end{cases}$$

and rewrite the flux density in the form

$$f(\boldsymbol{\gamma}(w), \phi) := g(x, \phi) = \gamma_1(x)b(\phi) + \gamma_2(x)(\phi - \phi_{\mathrm{F}}),$$

then (1.5) takes the form

$$\frac{\partial \phi}{\partial t} + \frac{\partial}{\partial x}f(\boldsymbol{\gamma}(x), \phi) = \frac{\partial}{\partial x}\left(\gamma_1(x)\frac{\partial A(\phi)}{\partial x}\right). \tag{1.6}$$

Figure 13 shows a plot of the function $g(x, \phi)$.

The equation (1.6) exhibits some non-standard properties. In particular, the flux function depends discontinuously on x, and the equation changes its type between first-order hyperbolic and second-order parabolic at the sediment level $\phi = \phi_{\mathrm{c}}$. The equation is strongly degenerate parabolic. Moreover, the degenerate diffusion term is "switched off" outside $[x_{\mathrm{L}}, x_{\mathrm{R}}]$. Another research problem is the characterization of admissible discontinuities of the concentration ϕ across the jumps of $\boldsymbol{\gamma}$. The current analysis (see [32,39]) is based on the assumption that $A(\phi)$ is continuous across the discontinuities at $x = x_{\mathrm{L}}, 0, x_{\mathrm{R}}$. Uniqueness and convergence of a simple finite difference scheme were shown in [32].

1.8. **Steady states and numerical simulations.** For practical purposes, two different kinds of quantitative results related to the clarifier-thickener model are of interest, namely firstly the description of stationary solutions that represent states of operation without any control actions, and secondly, transient simulations of scenarios such as fill-up of the unit or the response of the model to variations of the operating conditions.

The construction of steady states means seeking stationary solutions of (1.6). Roughly speaking, one omits the time derivative $\partial\phi/\partial t$ in that equation to obtain a second-order ordinary differential equation for ϕ as a function of x. Integrating this equation once, and fixing a suitable boundary condition, one obtains a first-order ordinary equation that can be integrated in x-direction to eventually obtain $\phi(x)$. This procedure is, however, subject to a number of limitations such as jump conditions across $x = x_{\mathrm{L}}$, 0, and x_{R}, and entropy (admissibility) conditions that ensure that the resulting stationary solutions are also entropy solutions according to the solution concept for the transient case. One can prove [32] that the consequence of satisfaction of these conditions is that the corresponding concentration profiles increase downwards (provided that the density of
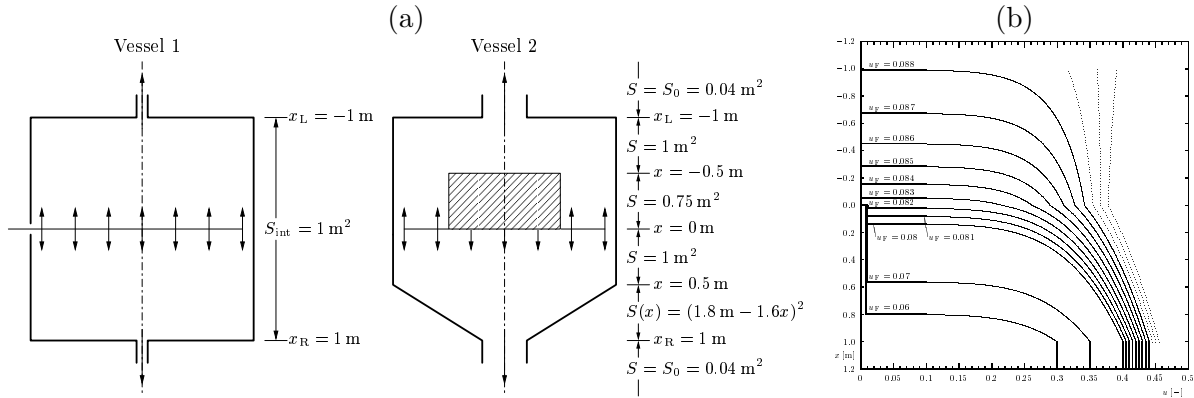
FIGURE 14. Clarifier-thickener model: (a) vessels used for steady-state calculations and numerical simulation, (b) construction of steady states in the cylindrical vessel of (a), taken from [32].
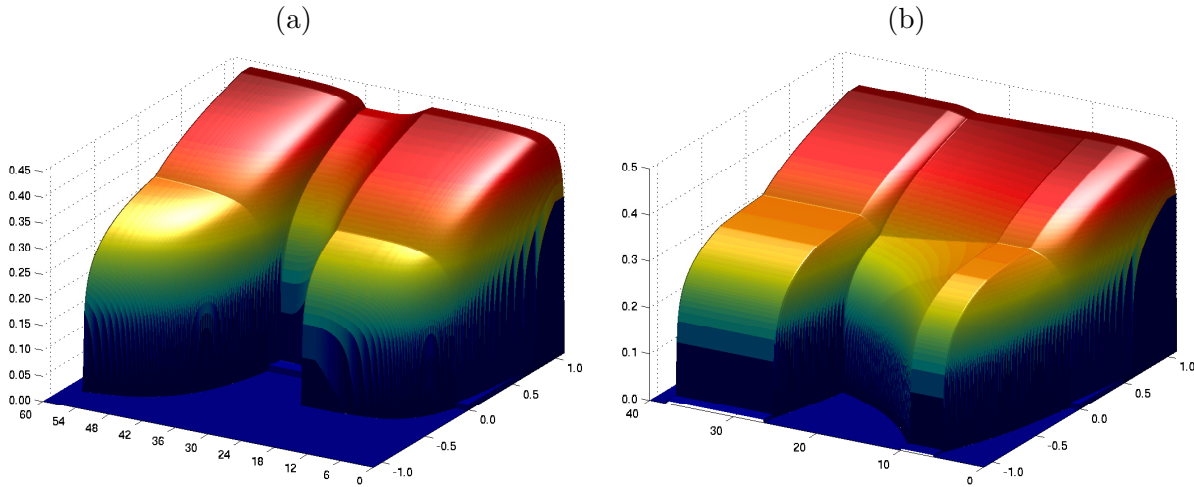

FIGURE 15. Simulation of a continuous clarifier-thickener under stepwise changes of ϕ_F: $0.086 \to 0.08 \to 0.088 \to 0$ (a) in vessel 1, (b) in vessel 2.

solid particles or flocs is larger than that of the liquid, which is the case in applications in mineral processing). Figure 14 (b) illustrates steady states for the cylindrical vessels of Figure 14 (a) for a given material, characterized by the model functions discussed above, and set values of the bulk flows Q_F, Q_L and Q_R, but where the feed concentration ϕ_F is varied. One observes that stationary profiles for relatively small values of ϕ_F can be accommodated in the thickening zone, while steady states for larger values of ϕ_F are only feasible in high-rate (or high-capacity) mode of operation. For values larger than about $\phi_F = 0.088$ steady states (for the given values of the remaining parameters) cannot be accommodated in the unit, or one observes loss of monotonicity in the appropriate sense, which points at violation of the entropy condition.

In [32] a suitable numerical scheme for the numerical solution of the transient model was defined, and its convergence was analyzed. A hands-on description of a variant of that scheme for a slightly extended model of a secondary settling tank, with all necessary details, is provided in [40]. We
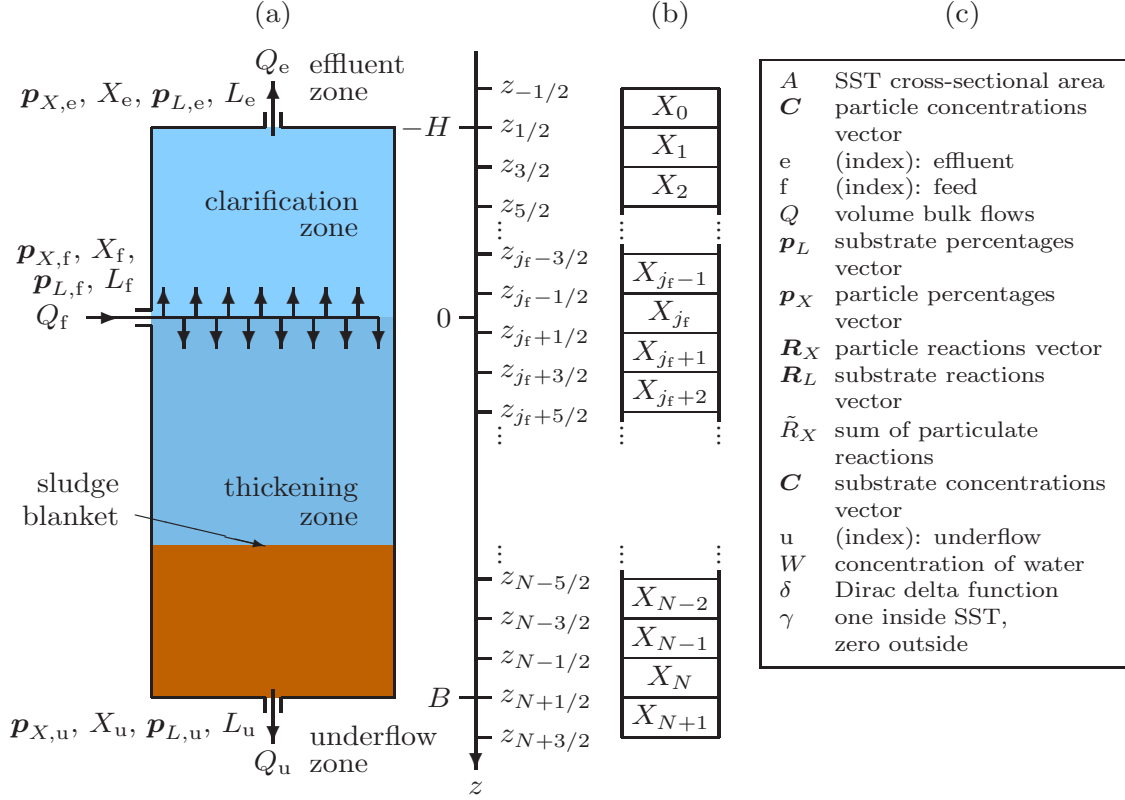
FIGURE 16. (a) An ideal secondary settling tank (SST) with variables of the feed inlet, effluent and underflow indexed with f, e and u, respectively [42]. The sludge blanket (concentration discontinuity) separates the hindered settling and compression regions. (b) Subdivision into computational cells. (c) Nomenclature.

here present one pair of simulations in Figure 15. Figure 15 (a) corresponds to a simulation that starts with an empty unit whose dimensions are those of the cylindrical one of Figure 14 (a). The unit is fed with suspension at $\phi_F = 0.086$. This corresponds to a steady state of high-capacity mode of operation. The steady state is attained after $t = 24$, where for physically relevant values of parameters and model functions (see [32]) time is measured in units of 10^6 seconds. Varying ϕ_F in a stepwise fashion as indicated in the caption of Figure 15 produces transitions between several steady states. In Figure 15 we display the corresponding solution for the vessel shown in Figure 14 (a) that has variable cross-sectional area. We observe that the same applied feed and bulk flows lead to solutions with nonzero overflow solids concentrations.

1.9. **Reactive settling.** Models of continuously operated settling tanks form a topic for well-posedness and numerical analysis even in one space dimension due to the spatially discontinuous coefficients of the underlying strongly degenerate parabolic, nonlinear model PDE (1.6). Such a model was recently extended [41, 42] to multi-component particles that react with several soluble constituents of the liquid phase. This process of so-called "reactive settling" takes place in the secondary settling tank (SST) within the Activated Sludge Process (ASP), see Figure 2. The fundamental balance equations contain the mass percentages of the components of both phases. The equations are reformulated in [42] as a system of nonlinear PDEs that can be solved by an

explicit numerical difference scheme. The scheme itself is not described in this contribution since space is limited. It combines a difference scheme for conservation laws with discontinuous flux, similar to that of [32], with numerical percentage propagation for multi-component flows [43].

The main variables are explained in Figure 16. The unknowns are X, L, $\boldsymbol{p}_X$ and $\boldsymbol{p}_L$ as functions of z and t. The solid and fluid densities, ρ_X and ρ_L, are assumed constant. The model keeps track of k_X particulate and k_L liquid components ($k_L - 1$ substrates and water), whose concentrations are collected in vectors $\boldsymbol{C}$ and $\boldsymbol{S}$ along with W, or equivalently, percentage vectors $\boldsymbol{p}_X$ and $\boldsymbol{p}_L$:

$$\boldsymbol{C} = \boldsymbol{p}_X X = \begin{pmatrix} p_X^{(1)} \\ \vdots \\ p_X^{(k_X)} \end{pmatrix} X, \quad \boldsymbol{p}_L L = \begin{pmatrix} p_L^{(1)} \\ \vdots \\ p_L^{(k_L)} \end{pmatrix} L = \begin{pmatrix} \boldsymbol{S} \\ W \end{pmatrix} = \begin{pmatrix} S^{(1)} \\ \vdots \\ S^{(k_L-1)} \\ W \end{pmatrix},$$

where $p_X^{(1)} + \cdots + p_X^{(k_X)} = 1$ and $p_L^{(1)} + \cdots + p_L^{(k_L)} = 1$. The governing system of equations can be formulated as follows:

$$\partial_t X + \partial_z F_X = \delta(z)\frac{X_{\mathrm{f}}Q_{\mathrm{f}}}{A} + \gamma(z)\tilde{R}_X(X), \quad F_X := Xq + \gamma(z)\big(f(X) - \partial_z D(X)\big),$$

$$\partial_t(\boldsymbol{p}_X X) + \partial_z(\boldsymbol{p}_X X) = \delta(z)\frac{\boldsymbol{p}_{X,\mathrm{f}}X_{\mathrm{f}}Q_{\mathrm{f}}}{A} + \gamma(z)\boldsymbol{R}_X,$$

$$L = \rho_L(1 - X/\rho_X),$$

$$\partial_t(\bar{\boldsymbol{p}}_L L) + \partial_z(\bar{\boldsymbol{p}}_L L) = \delta(z)\frac{\bar{\boldsymbol{p}}_{L,\mathrm{f}}X_{\mathrm{f}}Q_{\mathrm{f}}}{A} + \gamma(z)\bar{\boldsymbol{R}}_L, \quad F_L := \rho_L\left(q - \frac{F_X}{\rho_X}\right),$$

$$p_L^{(k_L)} = 1 - \big(p_L^{(1)} + \cdots + p_L^{(k_L-1)}\big)$$

(1.7)

for $z \in \mathbb{R}$ and $t > 0$, along with suitable initial conditions. The convective flux function F_X contains the spatially discontinuous bulk velocity $q(z,t)$, the hindered-settling flux function f given by

$$f(\phi) = \phi v_{\mathrm{hs}}(\phi). \tag{1.8}$$

and the sediment compressibility function

$$D(\phi) = \int_0^\phi \frac{\rho_X v_{\mathrm{hs}}(s)\sigma_{\mathrm{e}}'(s)}{g(\rho_X - \rho_L)}\,\mathrm{d}s, \tag{1.9}$$

where ρ_X and ρ_L denote the constant solid and fluid mass densities and σ_{e}' is the derivative of the so-called effective solid stress function $\sigma_{\mathrm{e}} = \sigma_{\mathrm{e}}(\phi)$ that satisfies

$$\sigma_{\mathrm{e}}'(\phi) = \frac{\mathrm{d}\sigma_{\mathrm{e}}(\phi)}{\mathrm{d}\phi} = \begin{cases} = 0 & \text{for } \phi \leq \phi_{\mathrm{c}}, \\ > 0 & \text{for } \phi > \phi_{\mathrm{c}}, \end{cases}$$

where ϕ_{c} denotes a critical concentration above which solid particles are assumed to form a porous network capable of supporting solid stress. Moreover, $\bar{\boldsymbol{p}}_L = \bar{\boldsymbol{p}}_L(z,t)$ is a vector of components of the liquid phase formed by the first $k_L - 1$ components of $\boldsymbol{p}_L$. The reaction term vectors are denoted by $\boldsymbol{R}_X$ and $\bar{\boldsymbol{R}}_L$, and lastly $\tilde{R}_X$ is the sum of all components of the vector $\boldsymbol{R}_X$.

The model (1.7) may include a full biokinetic Activated Sludge Model (ASMx; see [44]) at every depth z within $\boldsymbol{R}_X$ and $\bar{\boldsymbol{R}}_L$, and is based on the idea that hindered and compressive settling depend on the total particulate concentration (flocculated biomass) X modelled by the first equation. The particular formulation (1.7) has two advantages. Firstly, for a numerical method with explicit time stepping such as the one advanced in [42], the new value of X is obtained by solving the first equation in (1.7) only. Then $\boldsymbol{p}_X$ is updated by the second equation of (1.7), etc. Secondly, this
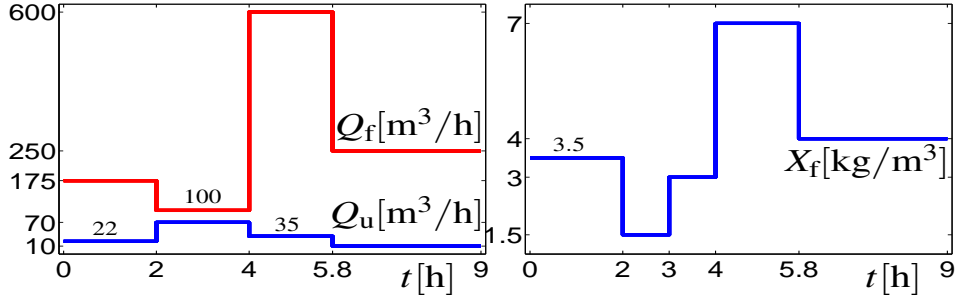
FIGURE 17. Piecewise constant functions Q_f and Q_u (feed and underflow volume rates) and X_f (solids feed concentration) for the numerical example of reactive settling (Figure 18).

formulation yields the invariant region property of the numerical scheme (see [42, Theorem 4.1]), which states that the solution stays in

$$\tilde{\Omega} := \big\{ \boldsymbol{\mathcal{U}} \in \mathbb{R}^{k_X + k_L + 2} : 0 \le \boldsymbol{p}_X, \boldsymbol{p}_L \le 1, \ 0 \le X \le X_{\max}, $$
$$\rho_L - r X_{\max} \le L \le \rho_L, \ p_X^{(1)} + \cdots + p_X^{(k_X)} = 1, \ p_L^{(1)} + \cdots + p_L^{(k_L)} = 1 \big\}$$

(vectors in inequalities should be interpreted component-wise), provided that the spatial meshwidth and the time step satisfy a suitable CFL condition.

We have no proof that an exact solution of system (1.7) stays in $\tilde{\Omega}$ if the initial datum does since the well-posedness (existence and uniqueness) analysis of the model is not yet concluded, and a suitable concept of a (discontinuous) exact solution is not yet established. However, it is reasonable to expect that an exact solution of (1.7) should also assume values within $\tilde{\Omega}$. To support this conjecture, we mention first that the invariant region property proved in [42] holds uniformly for approximate solutions, and therefore will hold for any limit to which the scheme converges as discretization parameters tend to zero. This standard argument has been used for related models in [32, 45, 46]. With the properties of the reaction term here, namely that $\tilde{R}_X = 0$ if $X = 0$ or $X = X_{\max}$, the invariance property of the numerical scheme follows by a monotonicity argument [42, Lemma 4.3]. The convergence of that scheme with a reaction term being a function of X only (and utilizing that it is zero for $X = 0$ or $X = X_{\max}$) can be established by modifying the proof in [32].

1.10. **Numerical example.** We present a numerical example. To specify the function f given by (1.8), we utilize

$$v_{\mathrm{hs}}(\phi) = v_0 / \big(1 + (\phi/\bar{\phi})^r \big), \quad \bar{\phi}, r > 0,$$

where $v_0 > 0$ is a constant that denotes the settling velocity of single particle in unbounded fluid, and $\phi_{\max}$ denotes a maximum solids concentration (see [47] for references), with volume fraction ϕ replaced by the equivalent local density X and the parameters $\bar{X} = 3.87 \, \mathrm{kg \, m^{-3}}$ and $r = 3.58$. The function D that describes sediment compressibility is specified by (1.9), where we choose $\sigma_{\mathrm{e}} = 0$ for $X < X_{\mathrm{c}}$ and $\sigma_{\mathrm{e}}(X) = \alpha(X - X_{\mathrm{c}})$ for $X > X_{\mathrm{c}}$ with $\alpha = 0.2 \, \mathrm{m^2 \, s^{-2}}$ and $X_{\mathrm{c}} = 5 \, \mathrm{kg \, m^{-3}}$. The velocity q is defined in terms of the given bulk flows as

$$q(z, t) = \frac{1}{A} \cdot \begin{cases} Q_{\mathrm{e}}(t) = Q_{\mathrm{f}}(t) - Q_{\mathrm{u}}(t) & \text{for } z < 0, \\ Q_{\mathrm{u}}(t) & \text{for } z > 0, \end{cases} \quad \text{where } A = 400 \, \mathrm{m^2}.$$
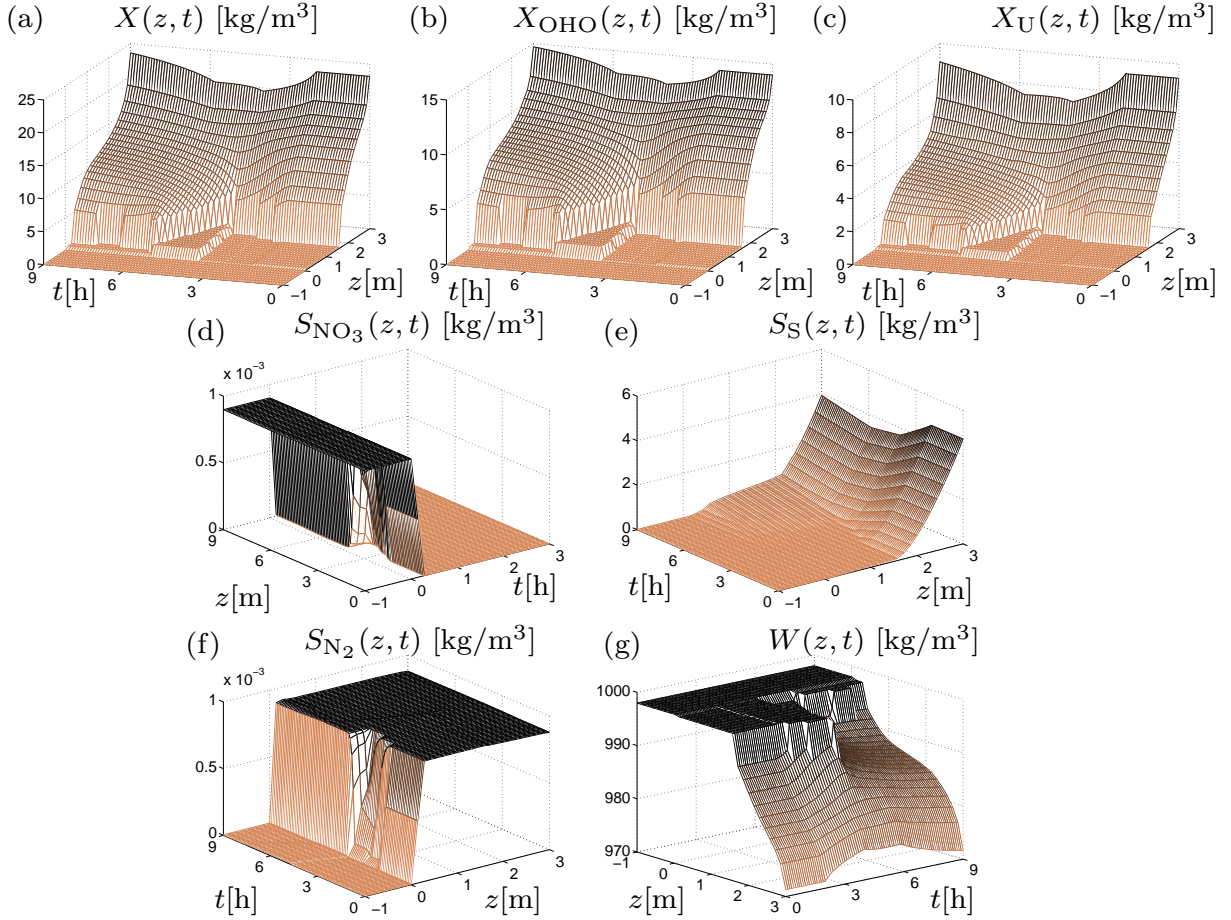
FIGURE 18. Simulation of reactive settling (denitrification) in an SST under variations of Q_u, Q_f and X_f (see Figure 17). Constants are standard in ASM1 [44] or arise in a strongly reduced model [41]: $b = 6.94 \times 10^{-6}\,\mathrm{s}^{-1}$, $f_p = 0.2$, $K_{NO_3} = 5.0 \times 10^{-4}\,\mathrm{kg\,m}^{-3}$, $X_{max} = 30\,\mathrm{kg\,m}^{-3}$, (the maximum solids concentration), $\mu_{max} = 5.56 \times 10^{-5}\,\mathrm{s}^{-1}$, $v_0 = 1.76 \times 10^{-3}\,\mathrm{m\,s}^{-1}$, $\rho_X = 1050\,\mathrm{kg\,m}^{-3}$, $\rho_L = 998\,\mathrm{kg\,m}^{-3}$, $g = 9.8\,\mathrm{m\,s}^{-2}$ (acceleration of gravity) and $Y = 0.67$ (yield factor).

We use a reduced biological model of denitrification, distinguishing $k_X = 2$ particulate components with concentrations X_{OHO} (ordinary heterotrophic organisms) and X_U (undegradable organics), and $k_L = 4$ liquid components, namely the substrates S_{NO_3} (nitrate), S_S (readily biodegradable substrate) and S_{N_2} (nitrogen), and water, such that $\boldsymbol{p}_X X = \boldsymbol{C} = (X_{OHO}, X_U)^{\mathrm{T}}$ and

$\boldsymbol{S} = (S_{\mathrm{NO_3}}, S_{\mathrm{S}}, S_{\mathrm{N_2}})^{\mathrm{T}}$. The reaction terms are then given by

$$\boldsymbol{R}_L = X_{\mathrm{OHO}} \begin{pmatrix} -\dfrac{1-Y}{2.86Y}\mu(\boldsymbol{S}) \\ (1-f_{\mathrm{p}})b - \dfrac{1}{Y}\mu(\boldsymbol{S}) \\ \dfrac{1-Y}{2.86Y}\mu(\boldsymbol{S}) \\ 0 \end{pmatrix}, \qquad \boldsymbol{R}_X = X_{\mathrm{OHO}} \begin{pmatrix} \mu(\boldsymbol{S}) - b \\ f_{\mathrm{p}}b \end{pmatrix},$$

$$\mu(\boldsymbol{S}) := \mu_{\max} \frac{S_{\mathrm{NO_3}}}{K_{\mathrm{NO_3}} + S_{\mathrm{NO_3}}} \frac{S_{\mathrm{S}}}{K_{\mathrm{S}} + S_{\mathrm{S}}},$$

where $\mu(\boldsymbol{S})$ is the so-called growth rate function. (Values of constants are given in the caption of Figure 18.) The resulting summed reaction terms are

$$\tilde{R}_X = \left(\mu(\boldsymbol{S}) - (1-f_{\mathrm{p}})b\right) X_{\mathrm{OHO}}, \quad \tilde{R}_L = \left((1-f_{\mathrm{p}})b - \frac{\mu(\boldsymbol{S})}{Y}\right) X_{\mathrm{OHO}}.$$

We choose the volumetric flows Q_{f} and Q_{u} and the feed concentration X_{f} as piecewise constant functions of t (see Figure 17), and let $\boldsymbol{p}_{X,\mathrm{f}}$ and $\boldsymbol{p}_{L,\mathrm{f}}$ be constant.

The whole simulation is shown in Figure 18. The initial steady state is kept during two hours of the simulation. There is a sludge blanket, i.e., a discontinuity from a low concentration up to $X = X_{\mathrm{c}}$. At $t = 4\,\mathrm{h}$, the step change of control functions causes a rapidly rising sludge blanket that nearly reaches the top of the SST around $t = 5.8\,\mathrm{h}$, when the control variables are changed again. The fast reactions imply that the soluble $\mathrm{NO_3}$ is quickly converted to $\mathrm{N_2}$ in regions where the bacteria OHO are present, which is below the sludge blanket.

2. Settling in vessels with varying cross-sectional area

2.1. **Motivation.** As we discussed in the previous section, the sedimentation of small particles in viscous fluid is a fundamental unit operation in mineral processing, wastewater treatment, medicine, geophysics, volcanology, etc., and mathematical models are needed for the simulation, design and control of processes and equipment. Thee focus is on macroscopic descriptions with unit-scale, long-time phenomena, so we seek continuum descriptions of solid/liquid phases. As we have seen, even in the simplest setting, common models lead to nonlinear time-dependent PDE. Their mathematical and numerical analysis has stimulated original research. In this section, we emphasize that mathematical models and numerical methods are accepted only if nonlinear coefficient functions can be calibrated, that is, adjusted to real scenarios, which immediately poses the so-called inverse problem (of parameter/function identification from real data).

Advanced models for clarifier-thickeners (also known as secondary settling tanks) for units with a constant cross-sectional area A can be formulated as

$$\frac{\partial \phi}{\partial t} + \frac{\partial}{\partial x}\left(\frac{Q(x)}{A}\phi + \gamma(x)f(\phi)\right)$$
$$= \frac{\partial}{\partial x}\left(\gamma(x)\frac{\partial D(\phi)}{\partial x}\right) + \delta(x)\frac{Q_{\mathrm{F}}}{A}(\phi - \phi_{\mathrm{F}}), \quad x \in \mathbb{R}, \quad t > 0,$$

where $Q(x)$ is the piecewise constant bulk flow, the discontinous parameter γ assumes the values $\gamma = 1$ inside and $\gamma = 0$ outside the unit; and $D(\phi)$ is a strongly degenerating function that describes sediment compressibility. Moreover, Q_{F} and ϕ_{F} are feed parameters. This model has been used in a number of papers in mineral processing and sanitary engineering, see e.g. [32, 40, 45, 48–52].

In this section we are concerned with the problem of identifying the function f from settling experiments, and advance the new idea that tests should be conducted in a vessel with varying cross-sectional area, for instance in a cone, an equipment that is widely used in sanitary engineering.
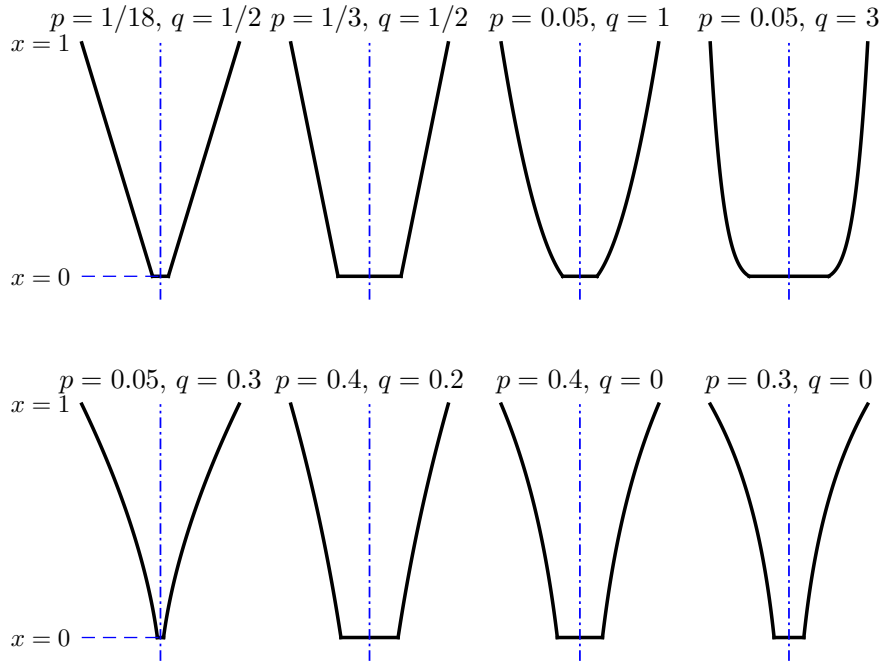
$p = 1/18, q = 1/2$ $p = 1/3, q = 1/2$ $p = 0.05, q = 1$ $p = 0.05, q = 3$

$x = 1$

$x = 0$

$p = 0.05, q = 0.3$ $p = 0.4, q = 0.2$ $p = 0.4, q = 0$ $p = 0.3, q = 0$

$x = 1$

$x = 0$

FIGURE 19. Examples of axisymmetric vessels described by (2.1) for several valued of the parameters p and q.

(a) (b) (c)
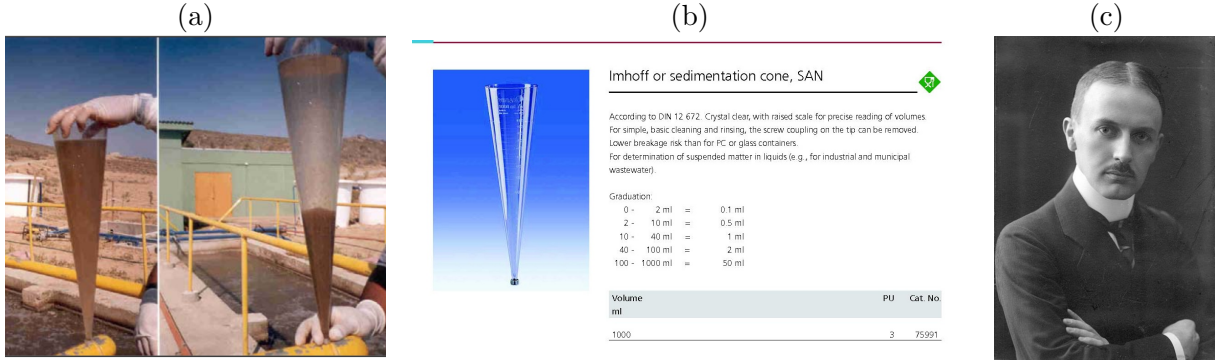
FIGURE 20. (a), (b): full cone: $p = 0$, $q = 1/2$, known as *Imhoff cone* in WWT, (c) Karl Imhoff (1876–1965): German civil engineer, author, and a pioneer of WWT; *Handbook of Urban Drainage*, 1906–present, translated into 20 languages.

To this end, and summarizing results from [48, 53, 54], we first outline the construction of solutions to the model problem of settling of an ideal suspension in a cone, and then describe how reading off the trajectory of the suspension-supernate interface through experiments provides information on the flux function f for a whole interval of ϕ-values, in contrast to the conventional batch test in a column.

2.2. **Model problem and new contribution.** We consider the following model problem that describes the settling of a suspension of an initially homogeneous suspension of volume fraction ϕ_0

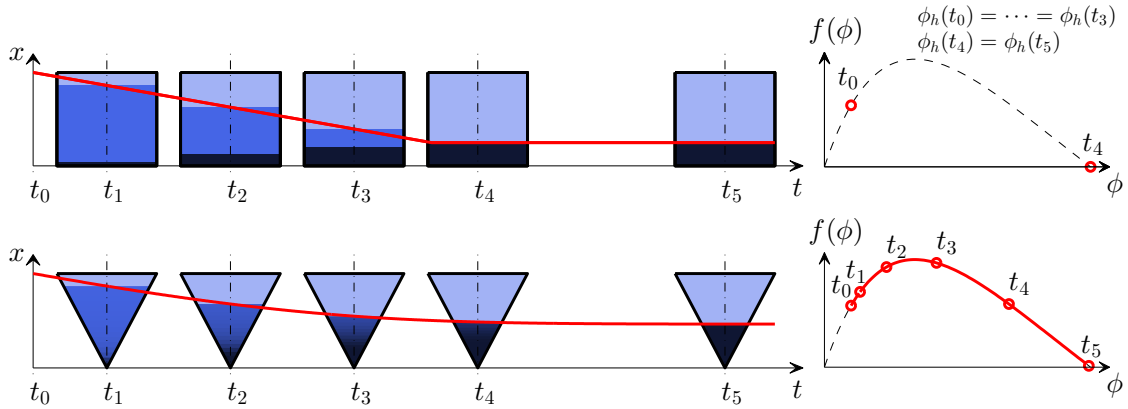FIGURE 21. Schematic of settling of a suspension in a cylinder (top) and in a cone (bottom). In the conical case, the concentration ϕ beneath the suspension-supernate interface gradually increases, so that the velocity of descent of that interface decreases, while in the cylindrical case that concentration and velocity are constant. As a consequence, that velocity of descent depends on a whole interval of ϕ-values and corresponding flux values $f(\phi)$. It is therefore possible to reconstruct the function $\phi \mapsto f(\phi)$ on a whole interval, which may be as large as $(\phi_0, \phi_{\max}]$, where ϕ_0 is the initial concentration, from a single batch test, while the cylindrical case permits only to obtain one point $(\phi_0, f(\phi_0))$ in addition to $(\phi_{\max}, f(\phi_{\max}))$, so a separate test has to be performed for each initial concentration [54, 79].

in a vessel of normalized height one, where $A(x)$ is the cross-sectional area at height x:

$$\frac{\partial}{\partial t}\big(A(x)\phi\big) - \frac{\partial}{\partial x}\big(A(x)f(\phi)\big) = 0, \quad 0 < x < 1, \quad t > 0,$$
$$\phi(x, 0) = \phi_0 \quad \text{for } 0 < x < 1,$$
$$\phi(0^+, t) = \phi_{\max} = 1, \tag{IBVP}$$
$$\phi(1^-, t) = 0 \quad \text{for } t > 0.$$

Here the flux function f is assumed to be non-negative with $f \in C^2$ such that $f(0) = f(1) = 0$, with a single maximum at ϕ^{M}, and an inflection point $\phi_{\mathrm{infl}} \in (\phi^{\mathrm{M}}, 1]$, such that $f''(\phi) < 0$ for $\phi < \phi_{\mathrm{infl}}$ and $f''(\phi) > 0$ for $\phi > \phi_{\mathrm{infl}}$. The cross-sectional area $A := A(x)$ is assumed to be invertible with $A'(x) \geq 0$. To be specific, we assume that there exist constants $p \geq 0$ and $q \geq 0$ with $(p^2 + q^2 \neq 0)$ such that

$$A(x) = \left(\frac{p + qx}{p + q}\right)^{1/q} \quad \text{for } 0 \leq x \leq 1. \tag{2.1}$$

Figure 19 shows some rotationally symmetric vessels for selected choices of p and q. Of particular interest is the case $p = 0$, $q = 1/2$ that correponds to a full cone since a cone is a commonly used equipment in wastewater treatment (the so-called "Imhoff cone", see Figure 20).

The novelty of our contributions is as follows. In [53] we construct explicit entropy solutions to (IBVP) by the method of characteristics, including numerical approximation of curved shock trajectories. In contrast to the cylindrical case, characteristics and iso-conce f with one inflection point, while the available previous solution of the problem by Anestis [55]: only applies to $V(\phi) =$

$1 - \phi$, that is $f(\phi) = \phi(1 - \phi)$; this function does not have an inflection point. It turns out [53] that there are three qualitatively different solutions, in dependence of ϕ_0. The analysis predicts that the propagation velocity of the suspension-supernate velocity is variable, and that the trajectory of this curve is a height versus time plot reflects the portion of the curve $\phi \mapsto f(\phi)$ for the range of ϕ-values adjacent to the curve. (This sharply contrasts with the cylindrical case in which this velocity is constant.) Under determined circumstances, the trajectory of this curve can be converted into the flux curve, which opens the way to a new method of flux identification if the suspension under study, and for which the material specific curve $\phi \mapsto f(\phi)$ is sought, is allowed to settle in a cone, see Figure 21.

2.3. Method of characteristics and jump condition.

To elucidate the method of characteristics as applied to the governing PDE in (IBVP), let us consider first the general quasilinear, first-order PDE

$$a(x, t, u)\frac{\partial u}{\partial t} + b(x, t, u)\frac{\partial u}{\partial x} = c(x, t, u), \quad (x, t) \in \Omega \subset \mathbb{R}^2. \tag{2.2}$$

We assume that this equation is supplied with a curve of the form

$$\Gamma : \nu \mapsto (x_0(\nu), t_0(\nu), U_0(\nu)) \in \mathbb{R}^3, \tag{2.3}$$

where ν belongs to a real interval. Then solving the initial-boundary value problem (2.2), (2.3) amounts to finding a surface

$$S = \left\{ (x, t, u(x, t)) \middle| (x, t) \in \Omega \right\} \subset \mathbb{R}^3$$

with the properties that $\Gamma \subset S$ and u is a solution of (2.2). The essence of the method of characteristics to solve the problem is outlined e.g. in [56, 57]. Roughly speaking, the method means that for each point $(x_0(\nu), t_0(\nu), U_0(\nu)) \in \Gamma$, one solves the following ordinary differential equations (the so-called characteristic equations) for $\eta \geq \eta_0$: , where $a = a(x(\nu, \eta), t(\nu, \eta), U(\nu, \eta))$, etc.:

$$\frac{\partial t}{\partial \eta} = a(x(\nu, \eta), t(\nu, \eta), U(\nu, \eta)), \quad \eta > \eta_0; \quad t(\nu, \eta_0) = t_0(\nu),$$

$$\frac{\partial x}{\partial \eta} = b(x(\nu, \eta), t(\nu, \eta), U(\nu, \eta)), \quad \eta > \eta_0; \quad x(\nu, \eta_0) = x_0(\nu), \tag{2.4}$$

$$\frac{\partial U}{\partial \eta} = c(x(\nu, \eta), t(\nu, \eta), U(\nu, \eta)), \quad \eta > \eta_0; \quad U(\nu, \eta_0) = U_0(\nu).$$

Their solutions are the characteristics of (2.2). If we can obtain $\nu = \nu(x, t)$ and $\eta = \eta(x, t)$ from the solution of (2.4), then the solution of (2.2), (2.3) is given by

$$\Omega \ni (x, t) \mapsto u = u(x, t) = U(\nu(x, t), \eta(x, t)) \in \mathbb{R}.$$

For the particular case of the initial value problem of a scalar conservation law

$$\frac{\partial u}{\partial t} + \frac{\partial g(u)}{\partial x} = 0, \quad x \in \mathbb{R}, \quad t > 0; \quad u(x, 0) = u_0(x), \quad x \in \mathbb{R}$$

we obtain

$$a \equiv 1, \quad b \equiv g'(u), \quad c \equiv 0; \quad \nu = x, \quad \eta = t,$$

such that in smooth regions,

$$u(x, t) = u_0(x - g'(u(x, t))t),$$

which means that the solution u is constant along straight characteristics

$$x(t) = x_0 + (t - t_0)g'\big(u(x_0, t_0)\big).$$

Clearly, in the case of a nonlinear conservation law ($g' \not\equiv 0$) characteristics carrying values $u^- \neq u^+$ may intersect, even for smooth u_0. This is handled by inserting a discontinuity that must travel at the speed given by the so-called Rankine-Hugoniot condition (jump condition)

$$S(u^-, u^+) := \frac{g(u^+) - g(u^-)}{u^+ - u^-}.$$

A discontinuity is said to be admissible if $S(u^-, u^+) \leq S(u^-, u)$ for all u between u^- and u^+.

2.4. Characteristics and entropy solutions for the model problem.

We now turn to the application of the method of characteristics to the model problem (IBVP). To this end, we rewrite the partial differential equation in (IBVP) as

$$\frac{\partial \phi}{\partial t} - f'(\phi)\frac{\partial \phi}{\partial x} = \frac{A'(x)}{A(x)}f(\phi) \ \Rightarrow \ a \equiv 1, \ b = -f'(\phi), \ c = \frac{A'(x)}{A(x)}f(\phi),$$

which means that we may choose t as a parameter along characteristics. Furthermore, assume that an initial curve $\Gamma : (x, t, \phi) = (\xi, \tau, \varphi)$ is given. Then $x = X(t)$ and $\phi = \Phi(t)$ satisfy the characteristic equations

$$\begin{cases} X'(t) &= -f'(\Phi), \quad t > \tau; \\ X(\tau) &= \xi, \end{cases} \quad \begin{cases} \Phi'(t) &= \dfrac{A'(X)}{A(X)}f(\Phi), \quad t > \tau; \\ \Phi(\tau) &= \varphi, \end{cases}$$

which means that $A' > 0$ implies that $\Phi' > 0$ along characteristics (in other words, concentration increases along characteristics). For the particular case of $A(x)$ given by (2.1), we get the characteristic system

$$\frac{t - \tau}{p + qx} = f(q)\int_\varphi^\phi \frac{\mathrm{d}\Phi}{f(\Phi)^{1+q}}, \quad \frac{f(\phi)}{f(\varphi)} = \left(\frac{p + q\xi}{p + qx}\right)^{1/q}. \tag{2.5}$$

To elucidate the implications of these equations, let us focus on the initial datum $(x, t, \phi) = (\xi, 0, \phi_0)$. Then (2.5) takes the form

$$\psi(x, t) := \frac{t}{p + qx} = f(\phi)^q \int_{\phi_0}^\phi \frac{\mathrm{d}\Phi}{f(\Phi)^{1+q}} =: Q(\phi) \tag{2.6}$$

This equation holds for small times, and describes the evolution of the concentration within the suspension between the supernate-suspension interface and the interfaces propagating upward from the bottom. To obtain ϕ at a given position from (2.6), written as $\psi(x, t) = Q(\phi)$, one must in principle invert the function $\phi \mapsto Q(\phi)$ to obtain

$$\phi(x, t) = Q^{-1}\big(\psi(x, t)\big). \tag{2.7}$$

From this equation we immediately read off that wherever the solution is defined by (2.7), ϕ is constant on the curves $\psi = \mathrm{const}$.

For a (truncated) cone, we have $q = 1/2$, and the iso-ψ-curves ($\Leftrightarrow$ iso-ϕ-curves) are straight lines intersecting at the vertex $x = -p/q$ for $t = 0$. On the other hand,

$$Q(\phi) = f(\phi)^{1/2}\int_{\phi_0}^\phi \frac{\mathrm{d}\Phi}{f(\Phi)^{3/2}}. \tag{2.8}$$
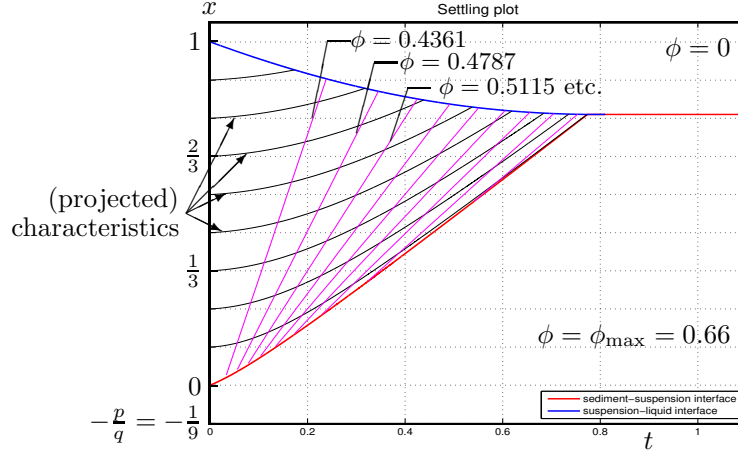
FIGURE 22. Construction of the entropy solution to the problem of settling of an ideal suspension with the quadratic flux $f(\phi) = \phi(1 - \frac{\phi}{\phi_{\max}})$, $\phi_{\max} = 0.66$, with initial concentration $\phi_0 = 0.35$, $q = 1/2$, $p = 1/18$, in a cone segment corresponding to $q = 1/2$ and $p = 1/18$. Note that this construction is covered the theory by Anestis [55].

This integral cannot be evaluated (let alone inverted) in closed form in general. However, for $f(\phi) = \phi(1 - \phi/\phi_{\max})$ this is possible, and we get

$$Q(\phi) = \left(\phi \left(1 - \frac{\phi}{\phi_{\max}} \right) \right)^{1/2} \left(\frac{4\dfrac{\phi}{\phi_{\max}} - 2}{\left(\phi - \dfrac{\phi^2}{\phi_{\max}}\right)^{1/2}} - \frac{4\dfrac{\phi_0}{\phi_{\max}} - 2}{\left(\phi_0 - \dfrac{\phi_0^2}{\phi_{\max}}\right)^{1/2}} \right).$$

In our works [53, 54] we use integrals $\int_{\phi_0}^{\phi} \ldots \, d\Phi$ (cf. (2.8)), in contrast to [55] where the expressions used are of the type. $\int_{f_0}^{f} \ldots \, d\tilde{f}$. Moreover we admit functions f with one inflection point, while Anestis [55] presupposes that f is quadratic.

The solution construction is completed by utilizing the jump condition. We rewrite the corresponding Rankine-Hugoniot condition as an ordinary differential equation that takes into account that the concentrations adjacent to a discontinuity are in general variable, and therefore the corresponding jump propagation speed is, in general, variable. Precisely, if $\phi^+(t)$ and $\phi^-(t)$ are solution values adjacent to a discontinuity $t \mapsto x_d(t)$, then

$$-x_d' = S(\phi^-, \phi^+) := \begin{cases} \dfrac{f(\phi^+) - f(\phi^-)}{\phi^+ - \phi^-} & \text{if } \phi^+ \neq \phi^-, \\ f'(\phi) & \text{if } \phi^+ = \phi^- =: \phi. \end{cases} \tag{RH}$$

Moreover, the jumo must satisfy the jump entropy condition (admissibility condition)

$$S(u, \phi^-) \geq S(\phi^+, \phi^-) \text{for all } u \text{ between } \phi^+ \text{ and } \phi^-. \tag{EJ}$$

Definition 2.1 (Entropy solution of (IBVP))**.** *A function $\phi = \phi(x, t)$ is an* entropy solution *of* (IBVP) *if ϕ is C^1 everywhere with the exception of a finite number of curves $x_d(t) \in C^1$ of discontinuities. At each jump, $\phi^{\pm} := \phi(x_d(t)^{\pm}, t)$ satisfy* (RH) *and* (EJ)*.*
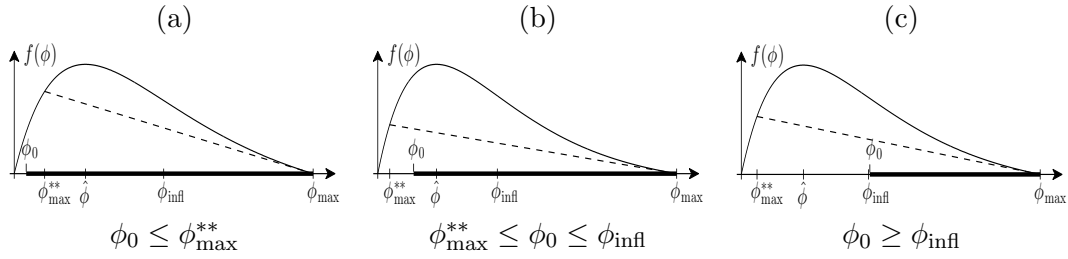
FIGURE 23. Cases of an (a) low, (b) intermediate and (c) high initial concentration ϕ_0 for the construction of the entropy solution to (IBVP), for a given flux density function f with inflection point ϕ_{infl} [53].

FIGURE 24. Solution to the problem of settling of an ideal suspension with flux parameter $r_{\mathrm{V}} = 4$, initial concentration $\phi_0 = 0.04$ (Case L), in a cone segment corresponding to $q = 1/2$ and $p = 1/18$. (a) Characteristics and discontinuities in the x versus t plane, (b) solution $\phi = \phi(x,t)$, (c) comparison of the constructed solution with a result produced by the Godunov scheme [53, 54].

For the case $f(\phi) = \phi(1 - \phi/\phi_{\mathrm{max}})$ we display in Figure 22 a sample construction of an entropy solution. Furthermore, we comment that the entropy solutions constructed here are also the unique entropy solns in the sense of Kružkov-type [58] entropy inequalities [57] that are defined by a particular entropy integral inequality On the other hand, monotone conservative difference schemes for scalar conservation laws (these are one-dimensional finite volume schemes, such as the Godunov scheme) converge to a Kružkov-type entropy solution [59] as discretization is refined. Thus we may verify the correctness of a solution construction by a numerical simulation, and use constructed solutions as reference solutions for efficient numerical solvers.

2.5. **Entropy solutions for $p > 0$.** In what follows, we focus on the case of a cone segment ($q = 1/2$) and assume first that $p > 0$, that is we assume that the cone is cut. The function f is assumed to have one inflection point ϕ_{infl}. For the solution construction we define [18]

$$\phi^* := \sup \left\{ u > \phi : S(\phi, u) \leq S(\phi, v) \ \forall v \in (\phi, u] \right\} \quad \text{for } \phi \in [0, \phi_{\mathrm{infl}}],$$

$$\phi^{**} := \inf \left\{ u < \phi : u^* = \phi \right\} \quad \text{for } \phi \in [\phi_{\mathrm{infl}}, \phi_{\mathrm{max}}].$$

The central result from [53] can then be stated as follows. There are three differently structured solutions corresponding to the respective cas of a low (L), medium (M), and high (H) value of ϕ_0, which are addressed in Figure 23.
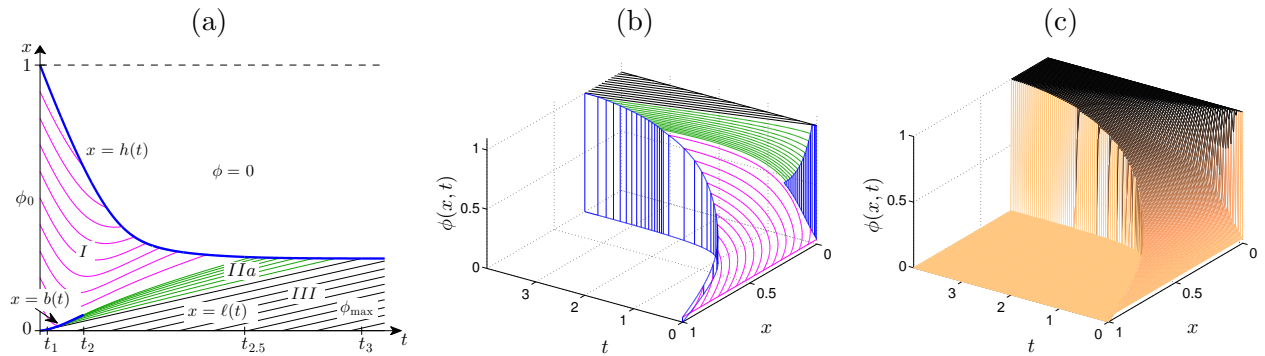
(a) (b)

FIGURE 25. Solution to the problem of settling of an ideal suspension with flux parameter $r_V = 4$, initial concentration $\phi_0 = 0.1$ (Case L), in a cone segment corresponding to $q = 1/2$ and $p = 1/3$. (a) Characteristics and discontinuities in the x versus t plane, (b) solution $\phi = \phi(x, t)$ [53, 54].

(a) (b)
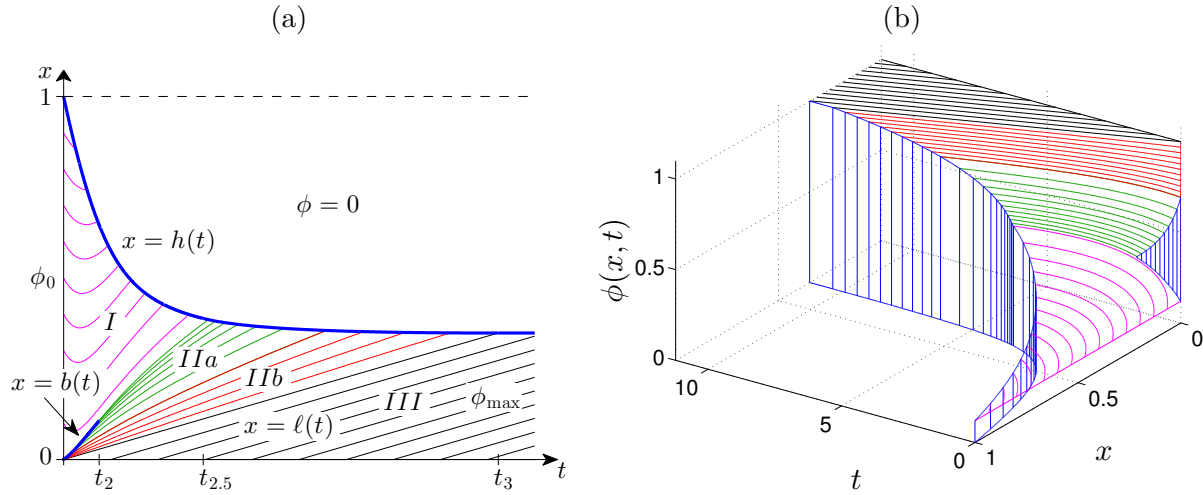
FIGURE 26. Solution to the problem of settling of an ideal suspension with flux parameter $r_V = 5$, initial concentration $\phi_0 = 0.12$ (Case M), in a cone segment corresponding to $q = 1/2$ and $p = 1/6$. (a) Characteristics and discontinuities in the x versus t plane, (b) solution $\phi = \phi(x, t)$ [53, 54].

The solutions are illustrated in Figures 24 to 27 [53, 54]. In each case an upper discontinuity $x = h(t)$ is defined for $0 \leq t \leq t_3$, where t_3 is the time at which the solution becomes stationary, and in Cases L and M a lower discontinuity $x = b(t)$ emerges from $x = 0$ at $t = t_1 > 0$, and may cease to exist at a time t_2 or merge with $h(t)$ at $t = t_{2.5}$. Regions I, IIa, etc. (denoted R_I, R_{IIa}, etc.) contain qualitatively different smooth solutions.
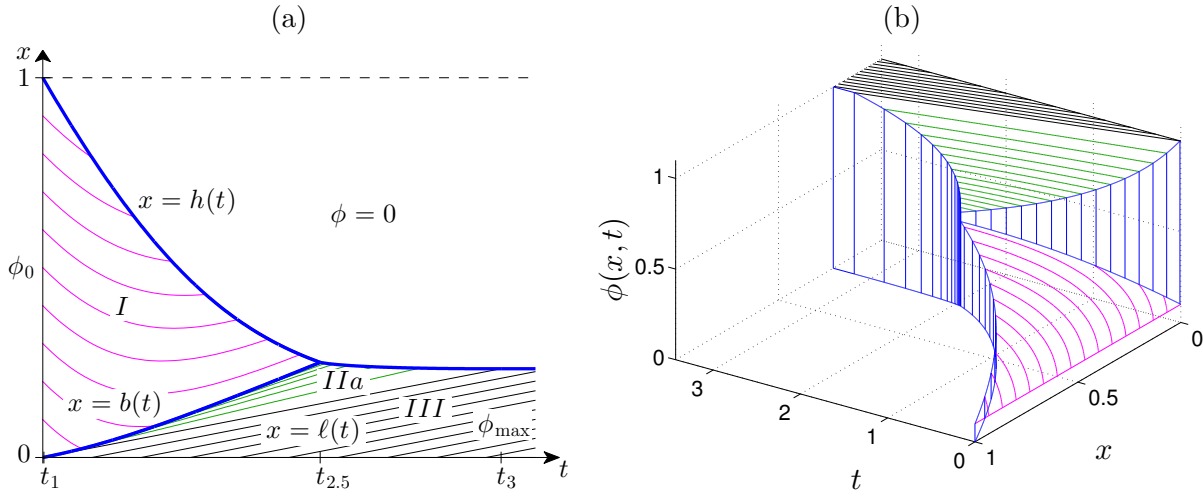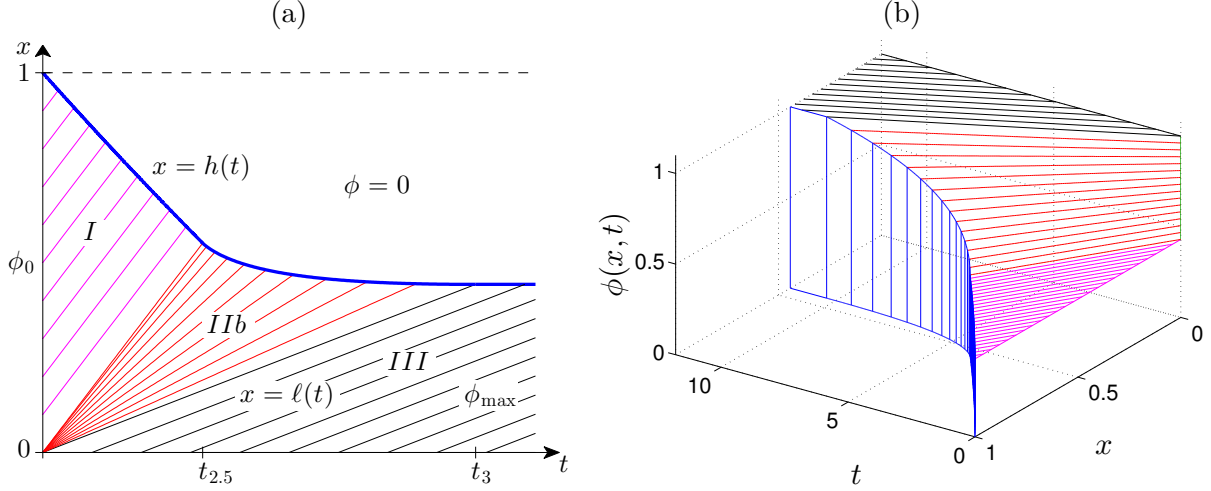
FIGURE 27. Solution to the problem of settling of an ideal suspension with flux parameter $r_V = 4.7$, initial concentration $\phi_0 = 0.43$ (Case H), in a cone segment corresponding to $q = 1/2$ and $p = 9.5$. (a) Characteristics and discontinuities in the x versus t plane, (b) solution $\phi = \phi(x,t)$ [53, 54].

The construction of the solution of a specific model case requires numerical methods to integrate the ordinary differential equations that define characteristics and curved shock trajectories. Nevertheless, it has been possible to obtain generic results on solution structure, and in particular on the conveexity of certain trajectories, that are summarized and illustrated in the following theorem.

Theorem 2.1 (Main theorem for $p, q > 0$ or $p > 0$ and $q \to 0^+$). *The entropy solution $\phi = \phi(x,t)$ of* (IBVP) *is piecewise smooth and has a decreasing shock $h(t)$, which is strictly convex for $0 < t < t_3$. Moreover:*

(i) *A discontinuity $b(t)$ rises from $x = 0$ if and only if $0 < \phi_0 < \phi_{\mathrm{infl}}$ (*Cases L and M*). It is a shock for $0 \leq t < t_1$, a contact for $t_1 \leq t < t_2$, and strictly convex for $0 \leq t < t_2$. Here h and b are smooth, except if $t_2 = t_{2.5}$ (i.e., h and b intersect); then h' jumps at $t = t_{2.5}$. If $t_2 < t_{2.5}$, then $b(t)$ dies at $t = t_2$.*

(ii) *$\partial\phi/\partial t > 0$ and $\partial\phi/\partial x < 0$ (weakly) except for $\phi = 0$ for $x > h(t)$ and $\phi = \phi_{\max}$ in R_{III}; and if $q = 0$, then $\partial\phi/\partial t > 0$ and $\partial\phi/\partial x = 0$ in R_{I}.*

(iii) *In R_{I}, $\phi(x,t) = Q^{-1}(\psi(x,t))$.*

Case H
$R_{\mathrm{IIa}} = \varnothing$
$R_{\mathrm{IIb}} \neq \varnothing$

Case M
$R_{\mathrm{IIa}} \neq \varnothing$
$R_{\mathrm{IIb}} \neq \varnothing$
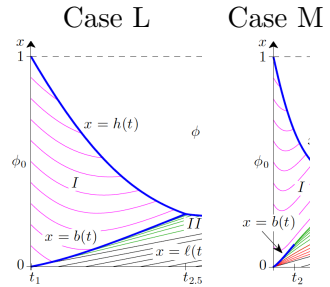
(iv) $R_{\mathrm{IIa}} = \varnothing$ if $\phi_{\mathrm{infl}} \leq \phi_0 < \phi_{\max}$ *(Case H)* *or if $P(\phi_{\mathrm{infl}}) \leq 0$ and $\phi_G < \phi_0 < \phi_{\mathrm{infl}}$. Otherwise, $\phi > \phi_{\mathrm{infl}}$ in R_{IIa}, and strictly concave characteristics emanate tangentially from $b(t)$ for $t_1 \leq t \leq t_2$.*
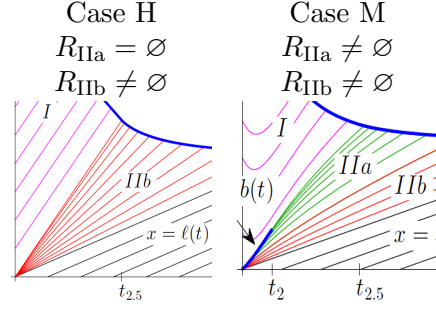
Case L
$R_{\mathrm{IIa}} \neq \varnothing$
$R_{\mathrm{IIb}} = \varnothing$

(v) $R_{\mathrm{IIb}} = \varnothing$ if $\phi_0 \leq \phi_{\max}^{**}$ *(Case L). Otherwise R_{IIb} is filled with concave characteristics emanating from $(x, t) = (0, 0)$ with initial values in $(\phi_0^*, \phi_{\max})$ in Case M, and in $(\phi_0, \phi_{\max})$ in Case H.*

2.6. Entropy solutions for $p = 0$ (full cone).

Let us now consider the case of a full cone ($p = 0$). Then the main theorem can be stated as follows (see [53, 54] for a proof).

Theorem 2.2 (Entropy solution in a full cone ($p = 0$)).

Case M

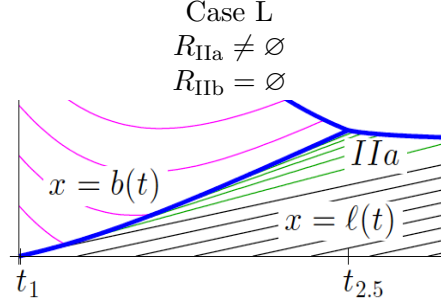(i) *Independently of ϕ_0: If $P(\phi_{\mathrm{infl}}) > 0$, then the solution is continuous under $0 \leq x \leq h(t)$ without bottom discontinuity b. (Here $P(\phi) := \dfrac{Q'(\phi)}{q f(\phi)^{q-1}}$.)*

Case L
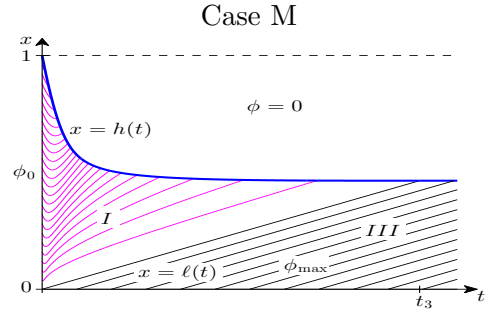
(ii) *For $\phi_0 \leq \phi_{\mathrm{infl}}$: If $P(\phi_{\mathrm{infl}}) \leq 0$, then the soln has both discontinuities, b is a straight line originating from the bottom, having the constant $\phi = \phi_G$ just above it, where $G(\phi_G) = 0$. $(G(\varphi) := S(\varphi, \varphi^-) + \dfrac{1}{qQ(\varphi)}.)$*
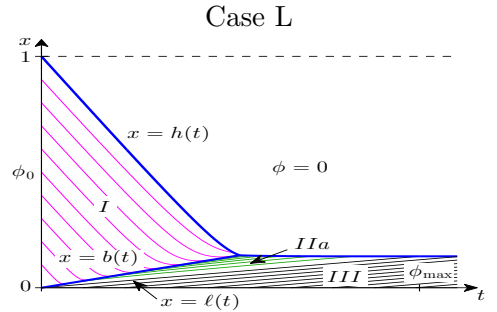
In [54] we discuss which of the aforementioned scenarios can be utilized to solve the flux identification problem of Figure 21. Roughly speaking, we are interested in those scenarios for which the interface $h(t)$ is defined by a unique ordinary differential equation, so that observations of $h(t)$ can unequivocally be converted into a portion of $\phi \mapsto f(\phi)$. This is not the case, for instance, in the scenario of Figure 26 since the definition of $h(t)$ changes between $t_{2.5}$ and t_3. In fact, no identification method for values of $\phi_h(t)$ (ϕ-values arising after endpoint $t_{2.5}$ of R_{I}) is feasible unless $t_{2.5} = t_3$,
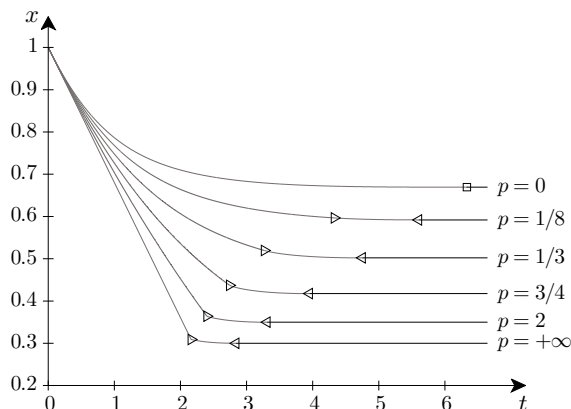
FIGURE 28. Positions of $t_{2.5}$ and t_3 (right-pointing triangle and left-pointing triangle, respectively) for $q = 1/2$ and several values of $p > 0$. The values coincide for $p = 0$ ($\square$) [54].

which happens as $p \to 0^+$, as is illustrated in Figure 28. The full curve $\phi \mapsto f(\phi)$, $\phi \in [\phi_0, \phi_{\max}]$, can be reconstructed only for $p = 0$.

2.7. **Flux identification (inverse problem).** In what follows, we assume that the settling of an initially homogeneous suspension of initial concentration ϕ_0 is described by model model (IBVP), where $A(x)$ is given by (2.1) for $p, q \geq 0$; and we assume that $0 \leq f \in C^2$; $f(0) = f(1) = 0$; f has one maximum $\hat{\phi}$ with $f'(\hat{\phi}) = 0$; and

$$f''(\phi) \begin{cases} < 0 & \text{for } \phi < \phi_{\text{infl}}, \\ > 0 & \text{for } \phi > \phi_{\text{infl}}, \end{cases} \quad \phi_{\text{infl}} \in (\hat{\phi}, 1].$$

The inverse problem we wish to solve has been addressed in Figure 21. For ease of reference, we formulate it as follows:

> Given the interface trajectory $[t_{\text{start}}, t_{\text{end}}] \ni t \mapsto h(t)$,
> find the portion of $\phi \mapsto f(\phi)$ corresponding to the interval of adjacent ϕ-values. 　　(IP)

To solve it, we observe that (under suitable circumstances) the upper discontinuity $h(t)$ and the ϕ-values $\phi_h = \phi(h^-(t), t)$ immediately below it satisfy the following relations for $0 \leq t \leq t_{2.5}$: the jump condition

$$f\big(\phi_h(t)\big) = -h'(t)\phi_h(t), \tag{2.9}$$

which is the Rankine-Hugoniot condition of a jump separating the ϕ-values $\phi_h(t)$ and zero of a discontinuity that moves at velocity $h'(t)$, and the equation

$$\psi\big(h(t), t\big) = Q\big(\phi_h(t)\big), \quad 0 \leq t \leq t_{2.5} \tag{2.10}$$

that describes the concentration below $h(t)$ (see (2.6) and (2.7)). Differentiating both equations (2.9) and (2.10) with respect to t, we obtain

$$f'\big(\phi_h(t)\big)\phi_h'(t) = -h''(t)\phi_h(t) - h'(t)\phi_h'(t),$$

$$\frac{\mathrm{d}\psi}{\mathrm{d}t}\big(h(t), t\big) = \Big(qf'\big(\phi_h(t)\big)Q\big(\phi_h(t)\big) + 1\Big)\frac{\phi_h'(t)}{f(\phi_h(t))}$$

$$\Rightarrow \quad \frac{\mathrm{d}\psi}{\mathrm{d}t}(h,t) = \left(q\psi(h,t)\left(-h''\frac{\phi_h}{\phi_h'} - h'\right) + 1\right)\frac{\phi_h'}{-h'\phi_h}$$

$$\Leftrightarrow \quad \frac{\phi_h'}{\phi_h} = \frac{1}{qh'\psi(h,t) - 1}\left(h'\frac{\mathrm{d}}{\mathrm{d}t}\big(\psi(h,t)\big) - q\psi(h,t)h''\right).$$

The last equation can be integrated, which leads to the following parametrized solution of (IP):

$$\phi_h(t) = \frac{\phi_0(p+q)^{1+1/q}}{(p+qh(t))^{1/q}(p+q\eta(t))}, \quad \eta(t) := h(t) - th'(t).$$

$$f(\phi_h(t)) = \frac{\phi_0(p+q)^{1+1/q}}{(p+qh(t))^{1/q}(p+q\eta(t))} \cdot \big(-h'(t)\big).$$

Theorem 2.3 (Parametrized solution of the inverse problem). *Assume $p \geq 0$, $q > 0$, and that ϕ_0 and the upper shock wave $x = h(t)$, $0 \leq t < t_{2.5}$, are known. Then (IP) has the parametrized solution*

$$\begin{pmatrix} \phi \\ f(\phi) \end{pmatrix} = \phi_0 \frac{(p+q)^{1+1/q}}{(p+qh(t))^{1/q}(p+q\eta(t))} \begin{pmatrix} 1 \\ -h'(t) \end{pmatrix}, \quad 0 \leq t \leq t_{2.5}, \tag{2.11}$$

where $\eta(t) := h(t) - th'(t)$.

Theorem 2.4 (Explicit solution of the inverse problem). *Assume that $p \geq 0$ and $q > 0$, which is the case of a (truncated or full) conical vessel, and that ϕ_0 and the upper shock wave $x = h(t)$, $0 \leq t < t_{2.5}$, are known. Then (IP) has the following explicit solution:*

$$f(\phi) = -\phi h'\left(\sigma^{-1}\left(\frac{\phi_0(p+q)^{1/q+1}}{\phi}\right)\right), \quad \phi_0 \leq \phi \leq \phi_h(t_{2.5}), \tag{EXF}$$

where $s(t) := (p+qh(t))^{1/q+1}$ and $\sigma(t) := s(t) - \dfrac{qt}{q+1}s'(t)$.

2.8. **Application to discrete data.** Theorems 2.3 and 2.4 allow us to define two alternative methods for solving the flux identification from discrete (e.g., measured) data that approximate the suspension-supernate interface in a cone. In both cases, we assume that the observed ("measured") interface trajectory is given by N data points

$$\big(t_1, h(t_1)\big), \ldots, \big(t_N, h(t_N)\big), \tag{2.12}$$

i.e., $h(t_j)$ is the observed interface height at time t_j, $j = 1, \ldots, N$.

Method 1 is based on formulating (IP) as a least-squares problem for h. This means we approximate the data points (2.12) by a piecewise cubic spline h_{spline} that is defined as

$$h_j(t) = a_j t^3 + b_j t^2 + c_j t + d_j, \quad j = 1, \ldots, J,$$

with coefficients a_j, b_j, c_j and d_j to be determined for $j = 1, \ldots, J$, where J is the number of subintervals that is supposed to satisfy $J \leq N/4$. According to Theorem 2.3, we impose $h_{\text{spline}} \in C^2$, $h'_{\text{spline}} < 0$, and $h''_{\text{spline}} > 0$. Then the task to determine the spline coefficients can be expressed as the following constrained least squares (quadratic programming) problem:

$$\begin{aligned} \text{minimize} \quad & J(\boldsymbol{p}) = (\boldsymbol{Q}\boldsymbol{p} - \boldsymbol{h})^{\mathrm{T}}(\boldsymbol{Q}\boldsymbol{p} - \boldsymbol{h}) \\ \text{subject to} \quad & \boldsymbol{R}\boldsymbol{p} = \boldsymbol{0}, \quad \boldsymbol{M}\boldsymbol{p} \leq \boldsymbol{b}, \end{aligned} \tag{QP1}$$

where $\boldsymbol{p}$ is the sought coefficient vector, $\boldsymbol{Q}$ is a particular block matrix whose rows contain properly placed evaluations of $(t^3, t^2, t, 1)$ at the measured times, the matrix $\boldsymbol{R}$ is related to constraints of continuity, and $\boldsymbol{M}$ is related to the inequalities of decreasing and convexity behavior. The precise

definitions are provided in [54, Appendix.3], and are similar to those of [60]. One can also prove (see [60]) that (QP1) has a unique solution $\boldsymbol{p}$, which define the cubic segments $h_j(t)$, $j = 1, \ldots, J$. Once these have been obtained, and noting that fr each cubic polynomial function

$$h'_j(t) = 3a_j t^2 + 2b_j t + c_j, \quad \eta_j(t) = -2a_j t^3 - b_j t + d_j,$$

we use the parametrized solution formula (2.11) to obtain

$$\begin{pmatrix} \phi_j(t) \\ f(\phi_j(t)) \end{pmatrix} = \frac{\phi_0(p+q)^{1+1/q}}{(p+qh_j(t))^{1/q}(p+q\eta_j(t))} \begin{pmatrix} 1 \\ -h'_j(t) \end{pmatrix}, \quad t_j \leq t \leq t_{j+1},$$

where $\{t_j\}$ represent the ends of each interval of the fit. This formula is aasily implemented, but has the disadvantage that no closed form for $\phi \mapsto f(\phi)$. Such a closed form is provided by the explicit solution formula (EXF), which relies on a function $t \mapsto \sigma(t)$ that can be easily inverted.

The corresponding procedure defines Method 2, which is based on formulating (IP) as a least squares problem as before *but for s*. Given data points (2.12), we now define the vector

$$\boldsymbol{s} := \left((p+qh(t_1))^{1+1/q}, \ldots, (p+qh(t_N))^{1+1/q} \right)^{\mathrm{T}},$$

and let s_{spline} be a piecewise cubic approximating spline defined on the j-th subinterval by $s_j(t) = a_j t^3 + b_j t^2 + c_j t + d_j$. We must now ensure that $s_{\mathrm{spline}} \in C^2$, $s'_{\mathrm{spline}} \leq 0$, and $s''_{\mathrm{spline}} > 0$. (One can show that s has these properties if and only if h has them.) The coefficients of $s_j(t)$ are obtained by solving a constrained least squares (quadratic programming) problem

$$\begin{aligned} \text{minimize} \quad & \tilde{J}(\boldsymbol{p}) = (\tilde{\boldsymbol{Q}}\boldsymbol{p} - \boldsymbol{s})^{\mathrm{T}}(\tilde{\boldsymbol{Q}}\boldsymbol{p} - \boldsymbol{s}) \\ \text{subject to} \quad & \tilde{\boldsymbol{R}}\boldsymbol{p} = \boldsymbol{0}, \quad \tilde{\boldsymbol{M}}\boldsymbol{p} \leq \tilde{\boldsymbol{b}}. \end{aligned} \tag{QP2}$$

similar to (QP1). Once the coefficient vector $\boldsymbol{p}$ has been obtained by solving (QP2), one uses (EXF) for σ_j and σ_j^{-1} on each interval and division points $\phi_j = \phi_p/\sigma_j(t_j)$ from s_j (here $\phi_p = \phi_0(p+q)^{1+1/q}$ is constant).

In Figure 29 we show as an example (from [54]) the flux identification from synthetic data in a cone obtained by Method 2. On the other hand, in Figure 30 we display results of the application of a variant of Method 1 to experimental data by White and Verdone [61]. That paper reports experiments of settling of magnesium hydroxide $Mg(OH)_2$ in water, involving the solids density $\rho_s = 2344.6 \, \text{kg/m}^3$ and initial concentrations of $C_0 = 50$, 60 and 70 g/l that correspond to $\phi_0 = C_0/\rho_s = 0.0213$, 0.0256 and 0.0299. Here the parametric formula (2.11) leads to closer estimations of cone data. We first non-dimensionalize the data (via $v_\infty = 10^{-4} \, \text{m/s}$). and fit the decreasing and strictly convex function

$$\bar{h}(t) = \frac{a}{t+b} + ct + d.$$

This yields the final flux

$$\tilde{f}(C) = \frac{e^{1-C/\rho_s} - 1}{e - 1} \frac{v_0 C}{1 + (C/\bar{C})^n} \tag{2.13}$$

with $v_0 = 3.5784 \times 10^{-4} \text{m/s}$, $\bar{C} = 49.570 \, \text{g/l}$ and $n = 2.6227$. Finally, some settling experiments with activated sludge form the wastewater treatment plant in Västeras, Sweden (pop=118,000) were conducted [62], see Figures 31 to 33.
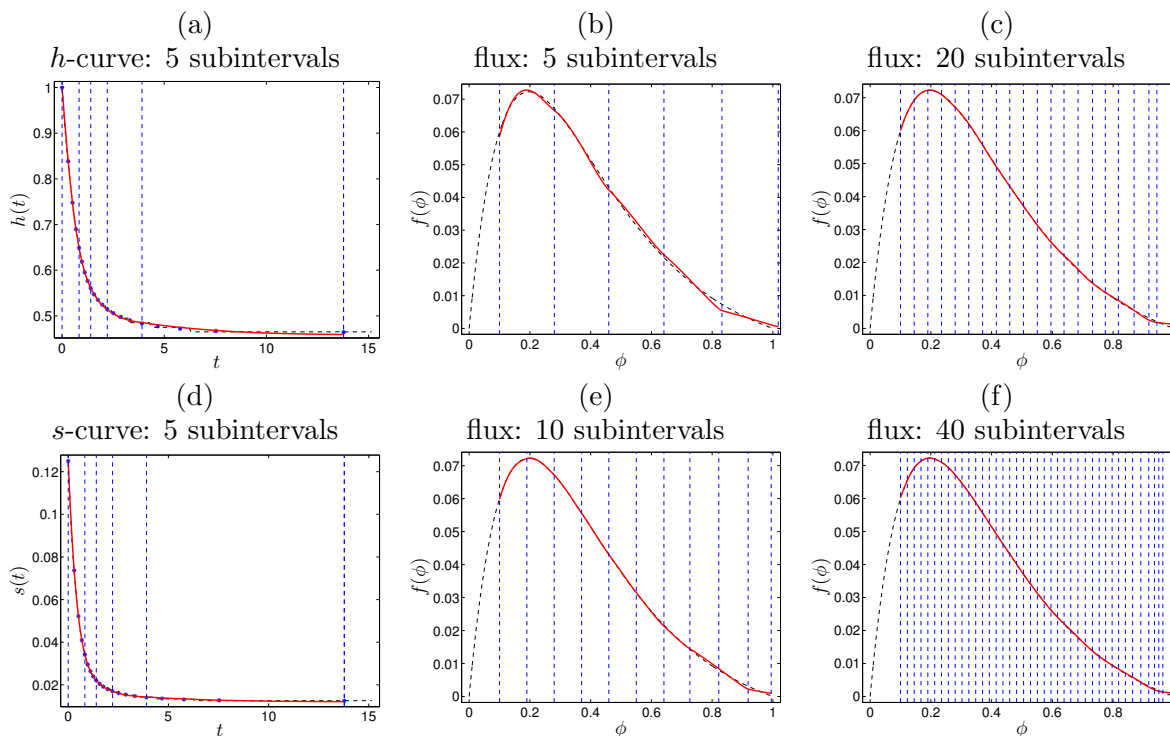
FIGURE 29. Flux identification from synthetic data in a cone obtained by Method 2 for a flux parameter $r_V = 5$ and initial concentration $\phi_0 = 0.1$ [54].

3. ON MODEL OF SEDIMENTATION OF POLYDISPERSE SUSPENSIONS

3.1. **Introduction.** We are interested in the process of sedimentation of small solid particles in a viscous fluid under the influence of gravity, as is illustrated in Figure 3 for a monodisperse suspension, that is, for which the solid particles have equal size and density. Standard references to simple kinematic models that describe the settling of such a mixture include [14, 15, 24]. We now focus on so-called polydisperse suspensions, in which the solid particles belong to a finite number of classes (species) that have different sizes and densities. The different species segregate and form areas of different composition. In many applications, a spatially one-dimensional description of this process, with the space coordinate aligned with the body force (usually gravity) is sufficient. The mathematical frame of continuum descriptions of that kind is given by first-order systems of nonlinear conservation laws [30, 63, 64] whenever sediment compressibility is not in effect. Applications of spatially one-dimensional polydisperse sedimentation models are reviewed in [65]. They include geophysics [66–69], chemical engineering [70, 71], mineral processing [72], medicine [73], petroleum engineering [74], wastewater treatment [51, 75, 76], and other areas. The systems of conservation laws arising in these applications are of arbitrary size (namely, of N scalar equations for N unknowns, that is, the N volume fractions $\phi_1, \ldots, \phi_N$ as a function of position x and time t if we distinguish N solid particle species), but their fluxes are constructed in a systematic way. In some important cases it is the possible to prove that the resulting system is strictly hyperbolic for equal-density particles [63, 77]. The flux Jacobian does not admit a closed-form eigenstructure, but spectral schemes can still be implemented [78].
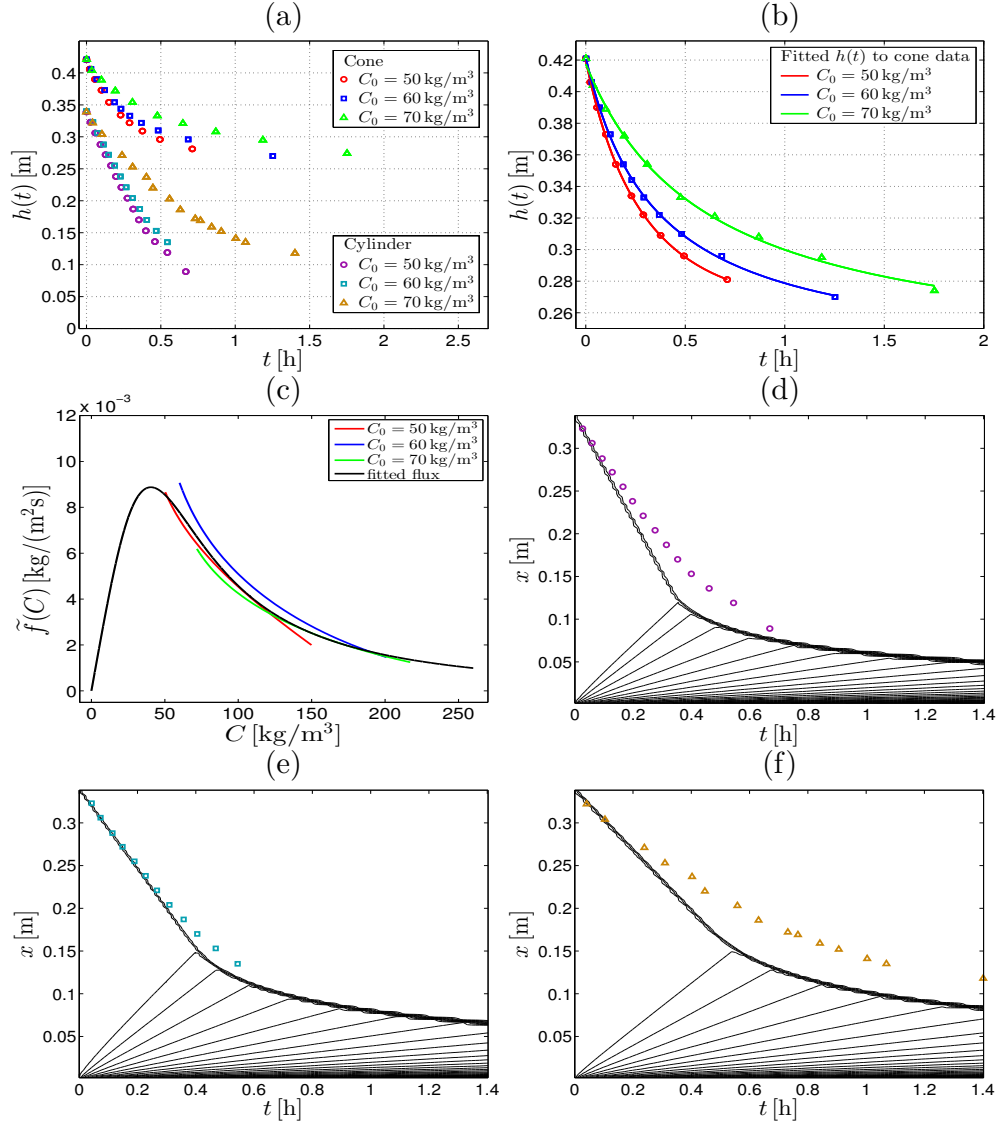
FIGURE 30. Application of a variant of Method 1 to experimental data by White and Verdone [61], see [54]: (a) experimental data of sedimentation of $Mg(OH)_2$ in water in a conical and cylindrical vessel, (b) fitted h-curves to cone data, (c) identified portions of flux function for each data set and fitted flux function $\tilde{f}(C)$ (see (2.13)), (d), (e), (f) fimulated batch tests in cylindrical vessel with $\tilde{f}(C)$ and cylinder data points from (a).

For the convective flow of a particulate suspension (e.g., in rivers and estuaries), that is for the description of vertical sedimentation superposed with a horizonal flow, two- or three-dimensional models are needes. These are computationally expensive since additional equations of motion need to be solved. However, certain simplification is possible for suspended sediment transport in shallow regimes, which can be described by a Saint-Venant or shallow water model combined with

Experimental setup   Experiment 1   Experiment 2
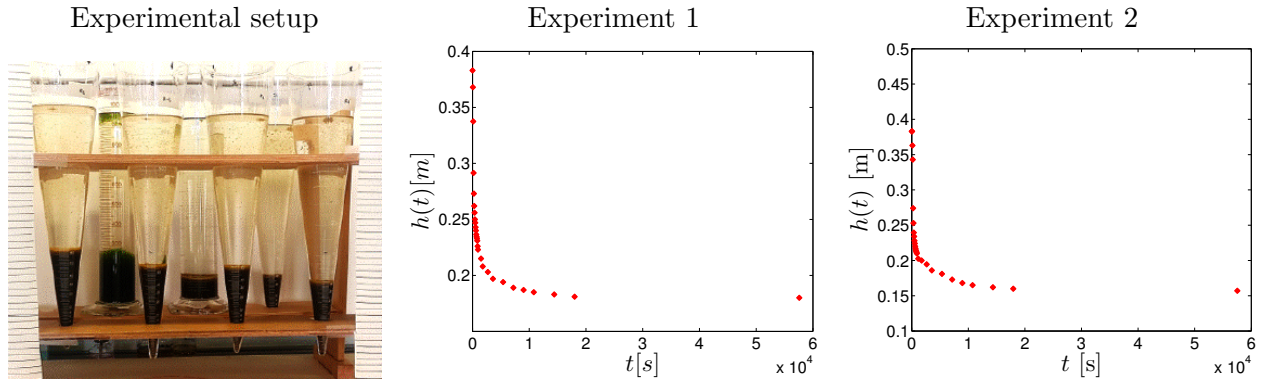
FIGURE 31. Settling experiments with activated sludge form the wastewater treatment plant in Västeras, Sweden (pop=118,000) [62].
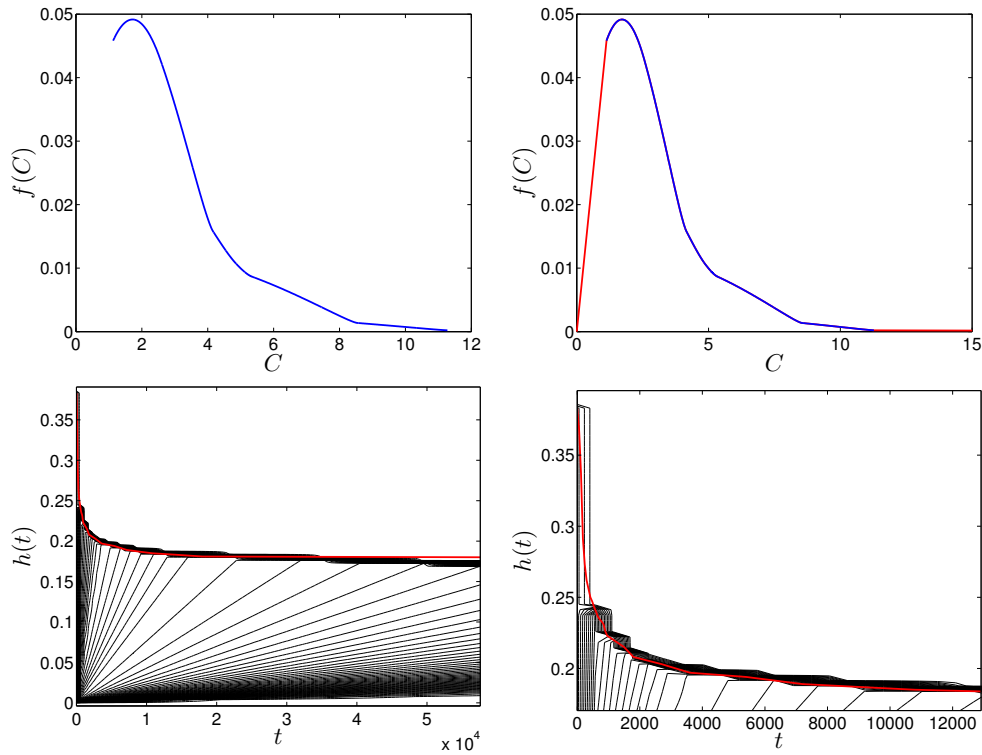
FIGURE 32. Settling experiments with activated sludge form the wastewater treatment plant in Västeras, Sweden (pop=118,000) [62].

passive transport equations for the different species. We herein consider a related model, namely a multilayer shallow water model for polydisperse sedimentation.

3.2. **Model of polydisperse sedimentation.** Let us first consider a multi-dimensional setup, where $\boldsymbol{x}$ denotes spatial position. It is assumed that the polydisperse suspensions consists of spherical solid particles that belong to N species of sizes $d_1 \geq \cdots \geq d_N$ and densities $\rho_1, \ldots, \rho_N$
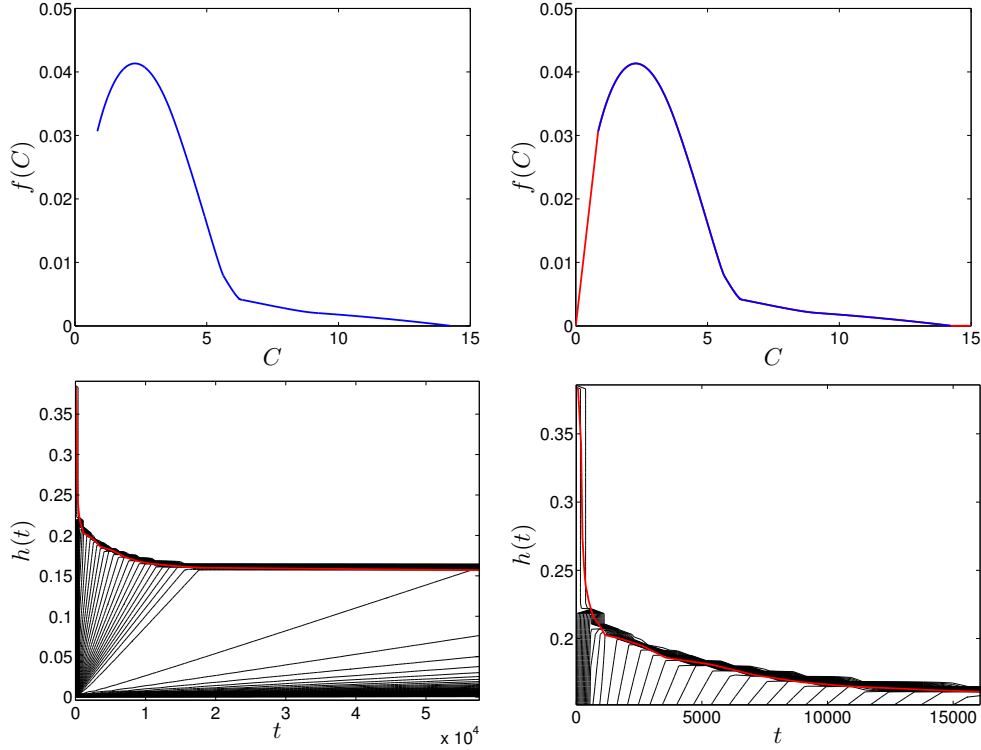
FIGURE 33. Settling experiments with activated sludge form the wastewater treat-
ment plant in Västeras, Sweden (pop=118,000) [62].

with the corresponding volume fractions $\phi_i = \phi_i(\boldsymbol{x}, t)$, $i = 1, \ldots, N$. Moreover, we define the total solids volume fraction $\phi := \phi_1 + \cdots + \phi_N$, where it is usually assumed that $0 \leq \phi \leq \phi_{\max}$, where $\phi_{\max}$ is a maximum packing density. This description presupposes that the particle sizes are relatively small, at least with respect to the diameter of the settling vessel, so that a continuum description is adequate but on the other hand colloidal effects are unimportant. Moreover, it is assumed that the fluid has density ρ_{f} and viscosity μ_{f}. If g denotes the acceleration of gravity, then the derived parameters used for the model formulation are

$$\mu = -\frac{g d_1^2}{18\mu_{\mathrm{f}}}, \quad \delta_j = \frac{d_j^2}{d_1^2}, \quad \bar{\rho}_j = \rho_j - \rho_{\mathrm{f}}, \quad \bar{\boldsymbol{\rho}} = \begin{pmatrix} \bar{\rho}_1 \\ \vdots \\ \bar{\rho}_N \end{pmatrix}, \quad \boldsymbol{\delta} = \begin{pmatrix} \delta_1 = 1 \\ \delta_2 \\ \vdots \\ \delta_N \end{pmatrix}, \quad \Phi = \begin{pmatrix} \phi_1 \\ \vdots \\ \phi_N \end{pmatrix}.$$

To formulate the balance equations in multiple dimensions, let us assume that $j = 0$ corresponds to the fluid and $j = 1, \ldots, N$ to the solid phases. We then obtain

$$\partial_t \phi_j + \nabla \cdot (\phi_j \boldsymbol{v}_j) = 0, \quad j = 0, \ldots, N, \tag{3.1}$$

$$\nabla \cdot \boldsymbol{q} = 0, \tag{3.2}$$

$$\rho_j \big(\partial_t(\phi_j \boldsymbol{v}_j) + \nabla \cdot (\phi_j \boldsymbol{v}_j \otimes \boldsymbol{v}_j)\big) = -\rho_j \phi_j g \boldsymbol{e}_z - \phi_j \nabla p, \quad j = 1, \ldots, N, \tag{3.3}$$

where $\boldsymbol{v}_j$ is the phase velocity of phase j ($j = 0, 1, \ldots, N$), $\boldsymbol{e}_z$ is the upward-pointing unit vector, and p is the pressure. The solids phase velocities are given by

$$\boldsymbol{v}_j = \boldsymbol{q} + v_j^{\mathrm{MLB}}(\Phi)\boldsymbol{e}_z, \quad j = 1, \ldots, N,$$

where v_j^{MLB} is the hindered settling function corresponding to the model introduced independently by Masliyah [80] and Lockett and Bassoon [81] ("MLB model"), namely

$$v_j^{\mathrm{MLB}}(\Phi) = \mu V(\phi)\left[\delta_j(\bar{\rho}_j - \bar{\boldsymbol{\rho}}^{\mathrm{T}}\Phi) - \sum_{l=1}^{N} \delta_l \phi_l(\bar{\rho}_l - \bar{\boldsymbol{\rho}}^{\mathrm{T}}\Phi)\right], \quad (3.4)$$

where V is a given function, sometimes called "hindered settling factor", that is assumed to satisfy

$$V(0) = 1, \quad V(\phi_{\max}) = 0, \quad V'(\phi) \le 0.$$

Finally, we remark that if the phase velocity $\boldsymbol{v}_j$ has a horizontal component $\boldsymbol{u}_j$ and a vertical component ϖ_j, $j = 0, \ldots, N$, then we assume that $\boldsymbol{u}_0 = \boldsymbol{u}_1 = \cdots = \boldsymbol{u}_N =: \boldsymbol{u}$.

If the particle species have equal density ρ_{s} (and differ in size only), then (3.4) reduces to

$$v_j^{\mathrm{MLB}} = \mu V(\phi)(1 - \phi)(\rho_{\mathrm{s}} - \rho_{\mathrm{f}})[\delta_j - \boldsymbol{\delta}^{\mathrm{T}}\Phi]. \quad (3.5)$$

Furthermore, in one space dimension, (3.2) implies that $\boldsymbol{q} = q$ is constant, with $q = 0$ for batch settling. Thus, for the description of settling in a column of height L we only need to solve the zero-flux initial-boundary value problem

$$\begin{aligned} &\partial_t \Phi + \partial_x \boldsymbol{f}(\Phi) = \boldsymbol{0}, \quad \boldsymbol{f}(\Phi) = (f_j(\Phi))_{j=1}^{N}, \quad f_j(\Phi) = \phi_j v_j(\Phi), \\ &\Phi(x, 0) = \Phi_0(x), \quad 0 \le x \le L; \quad \boldsymbol{f}(\Phi)|_{x=0} = \boldsymbol{f}(\Phi)|_{x=L} = \boldsymbol{0}. \end{aligned} \quad (\text{BSM})$$

This is a first-order nonlinear system of conservation laws whose solutions exhibit kinematic shocks (concentration discontinuities), in agreement with experimental evidence [82]. This model is discussed in Section 3.3.

On the other hand, if we still consider the one-dimensional case but assume that the sediment is compressible, then the governing model can be written as

$$\begin{aligned} &\partial_t \Phi + \partial_x \boldsymbol{f}(\Phi) = \partial_x\big(\boldsymbol{B}(\Phi)\partial_x\Phi\big), \quad (\text{DCM}) \\ &\Phi(x, 0) = \Phi_0(x), \quad 0 \le x \le L; \quad \boldsymbol{f}(\Phi) - \boldsymbol{B}(\Phi)\partial_x\Phi|_{x=0,L} = \boldsymbol{0}, \end{aligned}$$

where the term $\partial_x(\boldsymbol{B}(\Phi)\partial_x\Phi)$ describes a diffusive correction (DC) of the original kinematic model (see [30, 84, 85]). The diffusion matrix $\boldsymbol{B}(\Phi) = (\beta_{ij}(\Phi))_{i,j=1,\ldots,N}$ has the structure

$$\beta_{ij}(\Phi) = \gamma_{ij}(\Phi)\sigma_{\mathrm{e}}(\phi) + \alpha_{ij}(\Phi)\sigma_{\mathrm{e}}'(\phi)$$

with certain coefficient functions γ_{ij} and $\alpha_{ij}(\Phi)$ (whose precise algebraic definition is unimportant here), and where σ_{e} denotes the so-called effective solid stress function that is has the generic property

$$\sigma_{\mathrm{e}}(\phi), \sigma_{\mathrm{e}}'(\phi) \begin{cases} = 0 & \text{for } \phi \le \phi_{\mathrm{c}}, \\ > 0 & \text{for } \phi > \phi_{\mathrm{c}}, \end{cases} \quad \sigma_{\mathrm{e}}'(\phi) \text{ jumps at } \phi_{\mathrm{c}}, \quad (3.6)$$

corresponding to the assumption that effective solid stress can only be transmitted when the particles are in permanent contact, which in turn is assumed to occur when the total volume fraction ϕ exceeds a critical value ϕ_{c}, sometimes called "gel point". Clearly, under the assumption (3.6), the partial differential equation (PDE) in (DCM) is strongly degenerate. In fact, one can show [30] that the PDE of (DCM) is parabolic wherever $\sigma_{\mathrm{e}}(\phi)$ is active. This model is discussed in Section 3.7.

Finally, we consider an alternative formulation based on mass averaging. We define

$$\rho := \rho(\Phi) := \rho_0\phi_0 + \rho_1\phi_1 + \cdots + \rho_N\phi_N.$$

Then the mass average velocity of the mixture

$$\boldsymbol{v} := (u, v, w)^{\mathrm{T}} := \frac{1}{\rho}\sum_{m=0}^{N}\rho_m\phi_m\boldsymbol{v}_m = \frac{1}{\rho}\left[\left(\rho - \sum_{j=1}^{N}\rho_j\phi_j\right)\boldsymbol{v}_0 + \sum_{k=1}^{N}\rho_k\phi_k\boldsymbol{v}_k\right]$$

satisfies the global mass balance $\partial_t\rho + \nabla\cdot(\rho\boldsymbol{v}) = 0$. If we define the slip velocities $\boldsymbol{u}_i := \boldsymbol{v}_i - \boldsymbol{v}_0$ and the factor $\lambda_i := \rho_i\phi_i/\rho$ for $i = 1, \ldots, N$, then the solids mass balance equations can be rewritten as

$$\partial_t\phi_j + \nabla\cdot\left(\phi_j\left(\boldsymbol{u}_j + \boldsymbol{v} - \sum_{l=1}^{N}\lambda_l\boldsymbol{u}_l\right)\right) = 0, \quad j = 1, \ldots, N.$$

The governing model in final form is

$$\partial_t(\rho_j\phi_j) + \nabla\cdot(\rho_j\phi_j\boldsymbol{v}_j) = 0, \quad j = 1, \ldots, N,$$
$$\rho_j(\partial_t(\phi_j\boldsymbol{v}_j) + \nabla\cdot(\phi_j\boldsymbol{v}_j\otimes\boldsymbol{v}_j)) = \nabla\cdot\boldsymbol{T}_j^{\mathrm{E}} - \phi_j\nabla p - \phi_j\rho g\boldsymbol{k}, \quad j = 1, \ldots, N, \qquad (3.7)$$
$$\partial_t\rho + \nabla\cdot(\rho\boldsymbol{v}) = 0,$$

where

$$\boldsymbol{v}_j = \boldsymbol{v} + \tilde{v}_j^{\mathrm{MLB}}(\Phi)\boldsymbol{e}_z, \quad \tilde{v}_j^{\mathrm{MLB}}(\Phi) := \mu V(\phi)\left[\delta_j(\bar{\rho}_j - \bar{\boldsymbol{\rho}}^{\mathrm{T}}\Phi) - \sum_{l=1}^{N}\lambda_l\delta_l\phi_l(\bar{\rho}_l - \bar{\boldsymbol{\rho}}^{\mathrm{T}}\Phi)\right].$$

Summing up from 0 to N the equations (3.7) we have

$$\partial_t\left(\sum_{j=0}^{N}\rho_j\phi_j\boldsymbol{v}_j\right) + \nabla\cdot\left(\sum_{j=0}^{N}\rho_j\phi_j\boldsymbol{v}_j\otimes\boldsymbol{v}_j\right) = \nabla\cdot\boldsymbol{T} - \rho g\boldsymbol{k},$$

where the stress tensor of the mixture is given by

$$\boldsymbol{T} = \sum_{j=0}^{N}T_j = -p\boldsymbol{I} + \boldsymbol{T}^{\mathrm{E}}.$$

This model forms the basis of a multilayer shallow water formulation that is discussed in Section 3.11.

3.3. **Hyperbolicity and characteristic schemes.** It is possible to analyze the hyperbolicity for (BSM) and a wide class of models of the settling velocities v_i (including the MLB model) by the approach of the so-called secular equation [86], see [63, 77, 87], where we recall that the system of conservation laws

$$\partial_t\Phi + \partial_x\boldsymbol{f}(\Phi) = \boldsymbol{0} \qquad (3.8)$$

is called *hyperbolic* at a state $\Phi = \Phi_0$ if at that state, the eigenvalues of the flux Jacobian

$$\mathcal{J}_{\boldsymbol{f}}(\Phi) := (\partial f_i/\partial\phi_j)_{1\le i,j\le N}$$

are all real, and *strictly hyperbolic* if these are, moreover, pairwise distinct. For polydisperse sedimentation models, a particular result of the hyperbolicity analysis states that under determined conditions the eigenvalues of $\mathcal{J}_{\boldsymbol{f}}(\Phi)$, which are inaccessible in closed form, interlace with the given phase velocities v_i. This interlacing property is the basis of characteristic-wise (spectral, as opposed

to component-wise) high-resolution numerical schemes for the approximation of discontinuous so-lutions of (BSM) (see [78]). It particular it has turned out that spectral weighted essentially non-oscillatory schemes (WENO schemes; see [88–91]) are more accurate, and mostly more efficient, than their (easier to implement) component-wise (COMP) counterparts. Substantial further im-provements of efficiency are possible by adaptive techiques, for instance Adaptive Mesh Refinement (AMR) [96].

In the context of polydisperse sedimentation, the hyperbolicity of (3.8) is related to the stability of the separation of a polydisperse mixture, as is detailed in [64, 92]. Roughly speaking, stability in this context means that an initially homogeneous mixture of a given initial composition Φ_0 segregates under the formation of horizontal discontinuities and vertical gradients, and that blobs, fingers, and other structures related to instable separation do not occur. A linear stability analysis applied to (3.8) reveals that these phenomena are not amplified when $\mathcal{J}_{\boldsymbol{f}}(\Phi_0)$ has real eigenvalues only, that is (3.8) is hyperbolic at Φ_0. Since on the other hand, instabilities such as blobs and fingers have been observed for bidisperse mixtures ($N = 2$) only when particles with different densities are involved ($\rho_1 \neq \rho_2$), one should expect that a sound mathematical model should be be hyperbolic for equal-density particles, arbitrary N and $\delta_N \ll 1$. This was proved in [30] for the MLB model (precisely, for the version (3.5), (BSM)).

3.4. **Secular equation and interlacing property.** In many cases, one may exploit the system-atic algebraic construction of the velocity functions v_i for the hyperbolicity analysis as follows. Many models (proposed choices of $v_i(\Phi)$) can be written as

$$v_i = v_i(p_1, \ldots, p_m), \quad p_l = p_l(\Phi), \quad m \ll N,$$

i.e., the velocity v_i of species i does not depend on each of the N components $\phi_1, \ldots, \phi_N$ of Φ individually, but rather on a small number $m \ll N$ of functions $p_1(\Phi), \ldots, p_m(\Phi)$. One then obtains that $\mathcal{J}_{\boldsymbol{f}}(\Phi)$ is a rank-m perturbation of the diagonal matrix $\boldsymbol{D} := \mathrm{diag}(v_1, \ldots, v_N)$. Precisely, one can write

$$\mathcal{J}_{\boldsymbol{f}} = \boldsymbol{D} + \boldsymbol{B}\boldsymbol{A}^{\mathrm{T}}, \quad \begin{cases} \boldsymbol{B} := (B_{il}) = (\phi_i \partial v_i / \partial p_l), & 1 \leq i, j \leq N, \\ \boldsymbol{A} := (A_{jl}) = (\partial p_l / \partial \phi_j), & 1 \leq l \leq m. \end{cases}$$

The following theorem indicates how this stucture can be exploited to facilitate the location of eigenvalues.

Theorem 3.1 (The secular equation [86]). *A number $\lambda \notin \{v_1, \ldots, v_N\}$ is an eigenvalue of the matrix $\boldsymbol{D} + \boldsymbol{B}\boldsymbol{A}^{\mathrm{T}}$ if and only if $R(\lambda) = 0$ (the "secular equation"), where we define*

$$R(\lambda) := \det\left[\boldsymbol{I} + \boldsymbol{A}^{\mathrm{T}}(\boldsymbol{D} - \lambda\boldsymbol{I})^{-1}\boldsymbol{B}\right] = 1 + \sum_{i=1}^{N} \frac{\gamma_i}{v_i - \lambda},$$

$$\gamma_i := \sum_{r=1}^{\min\{N,m\}} \sum_{i \in I \in S_r^N, J \in S_r^m} \frac{\det \boldsymbol{A}^{I,J} \det \boldsymbol{B}^{I,J}}{\prod_{l \in I, l \neq i}(v_l - v_i)},$$

where S_r^N is the set of all subsets of $\{1, \ldots, N\}$ with r elements, and S_r^m is defined analogously.

From Theorem 3.1 one may deduce the following result.

Corollary 3.1 (Interlacing property). *If $\gamma_i \cdot \gamma_j > 0$ for all i, j, then $\boldsymbol{D} + \boldsymbol{B}\boldsymbol{A}^{\mathrm{T}}$ is diagonalizable with real eigenvalues $\lambda_1, \ldots, \lambda_N$. Let $\tilde{\gamma} := \sum_{i=1}^{N} \gamma_i$. Then*

$$M_1 := v_N + \tilde{\gamma} < \lambda_N < v_N < \lambda_{N-1} < \ldots < \lambda_1 < v_1,$$

$$v_N < \lambda_N < v_{N-1} < \lambda_{N-1} < \ldots < v_1 < \lambda_1 < M_2 := v_1 + \tilde{\gamma}.$$

One may easily verify that the MLB model for equal-density particles, as described by (3.5), is a case of $m = 2$ with $\gamma_i < 0$ follows easily; thus, in this case (BSM) is strictly hyperbolic for all $\Phi > 0$. The eigenvalues satisfy the interlacing property. On the other hand, for the models by Batchelor and Wen [93], Davis and Gecol [94] and others one can prove definite sign of γ_i only if $\delta_N > \delta_{\min,\text{model}}(\boldsymbol{\delta}, \phi_{\max}) > 0$, that is for a finite range of particle size ratios. For a given eigenvalue $\lambda \notin \{v_1, \ldots, v_N\}$, the eigenvectors can be calculated efficiently when the interlacing property is in effect.

3.5. **SPEC-INT and COMP-GLF numerical schemes.** We now consider the numerical approximation of discontinuous solutions of (BSM). A conservative, fully discrete scheme for the computation of $\Phi_i^n \approx \Phi(x_i = (i + \frac{1}{2})\Delta x, t_n = n\Delta t)$ can be written as

$$\Phi_i^{n+1} = \Phi_i^n - \frac{\Delta t}{\Delta x}\big(\hat{\boldsymbol{f}}_{i+1/2} - \hat{\boldsymbol{f}}_{i-1/2}\big),$$

$$\hat{\boldsymbol{f}}_{i+1/2} = \hat{\boldsymbol{f}}\big(\Phi_{i-s+1}^n, \ldots, \Phi_{i+s}^n\big), \quad i = 0, \ldots, M-1; \quad \hat{\boldsymbol{f}}_{-1/2} = \hat{\boldsymbol{f}}_{M-1/2} = \boldsymbol{0},$$

where $\hat{\boldsymbol{f}}_{i+1/2}$ is the numerical flux vector associated with the cell interface x_{i+1}. In general, the basic idea of construction of numerical schemes consists in applying an ODE solver (in our case, a third-order Kunge-Kutta TVD method) to the spatially semi-discretized equations [95].

To compute $\hat{\boldsymbol{f}}_{i+1/2}$, one may use the eigenstructure of $\mathcal{J}_{\boldsymbol{f}}(\Phi_{i+1/2})$, where $\Phi_{i+1/2} := \frac{1}{2}(\Phi_i + \Phi_{i+1})$, given by the right and left eigenvectors:

$$\boldsymbol{R}_{i+1/2} = [\boldsymbol{r}_{i+1/2,1}, \ldots, \boldsymbol{r}_{i+1/2,N}], \quad \big(\boldsymbol{R}_{i+1/2}^{-1}\big)^{\mathrm{T}} = [\boldsymbol{l}_{i+1/2,1}, \ldots, \boldsymbol{l}_{i+1/2,N}].$$

From a local flux splitting

$$\boldsymbol{f}^{-,k} + \boldsymbol{f}^{+,k} = \boldsymbol{f}, \quad \pm\lambda_k(\mathcal{J}_{\boldsymbol{f}^{\pm,k}}(\Phi)) \geq 0, \quad \Phi \approx \Phi_{i+1/2}, \quad k = 1, \ldots, N,$$

we can define $g_j^{\pm,k} := \boldsymbol{l}_{i+1/2,k}^{\mathrm{T}} \cdot \boldsymbol{f}^{\pm,k}(\Phi_j)$, and use upwind-biased reconstructions $\mathcal{R}^{\pm}$ (e.g., the WENO method), to calculate

$$\hat{g}_{i+1/2,k} = \mathcal{R}^+\big(g_{i-s+1}^{+,k}, \ldots, g_{i+s-1}^{+,k}; x_{i+1/2}\big) + \mathcal{R}^-\big(g_{i-s+2}^{-,k}, \ldots, g_{i-s}^{-,k}; x_{i+1/2}\big),$$

$$\hat{\boldsymbol{f}}_{i+1/2} = \boldsymbol{R}_{i+1/2}\hat{\boldsymbol{g}}_{i+1/2} = \sum_{k=1}^{n} \hat{g}_{i+1/2,k}\boldsymbol{r}_{i+1/2,k}.$$

The component-wise global Lax-Friedrichs (COMP-GLF) scheme is based on the alternative of setting $\boldsymbol{R}_{i+1/2} = \boldsymbol{I}_N$, where $\boldsymbol{I}_N$ is the $N \times N$ identity matrix, and utilizing a global flux splitting $\boldsymbol{f}^- + \boldsymbol{f}^+ = \boldsymbol{f}$, where $\pm\lambda_k(\mathcal{J}_{\boldsymbol{f}^{\pm}}(\Phi)) \geq 0$ for all k. This results in the choice

$$g_j^{\pm,k} = \boldsymbol{e}_k^{\mathrm{T}}\boldsymbol{f}^{\pm}(\Phi_j) = f_k^{\pm}(\Phi_j),$$

which leads to a high-order extension of the Lax-Fiedrichs scheme.

A more sophisticated scheme is based on spectral properties of the flux Jacobian in conjunction with the interlacing property (Corollary 3.1), to which we refer as SPEC-INT scheme. To outline it, we assume that $\mathcal{S}_{i+1/2}$ is the segment joining states Φ_i and Φ_{i+1}. If $\lambda_k(\mathcal{J}_{\boldsymbol{f}}(\Phi)) > 0$ (resp., < 0) on $\mathcal{S}_{i+1/2}$ then we upwind (no need for flux splitting). However, if $\lambda_k(\mathcal{J}_{\boldsymbol{f}}(\Phi))$ changes sign on $\mathcal{S}_{i+1/2}$, then we use a local Lax-Friedrichs flux splitting with numerical viscosity parameter α_k:

$$\boldsymbol{f}^{\pm,k}(\Phi) = \boldsymbol{f}(\Phi) \pm \alpha_k\Phi, \quad \alpha_k \overset{!}{\geq} \max_{\Phi \in \mathcal{S}_{i+1/2}} \big|\lambda_k\big(\mathcal{J}_{\boldsymbol{f}}(\Phi)\big)\big|.$$
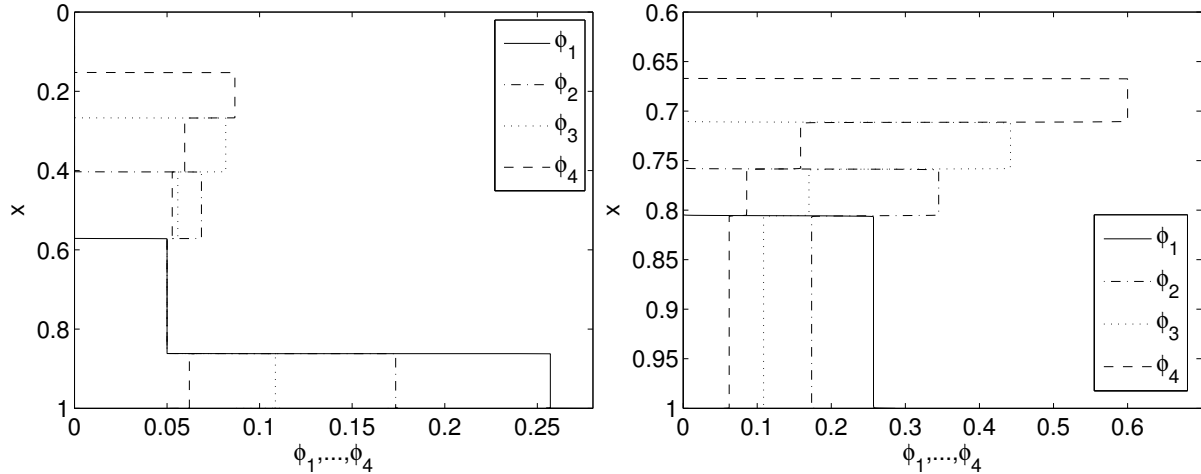
FIGURE 34. Example 1 (settling of a suspension of $N = 4$ solid species): reference solution with $M = M_{\mathrm{ref}} = 6400$ at simulated times $t = 50\,\mathrm{s}$ and $t = 300\,\mathrm{s}$ [78].

The computation of this parameter depends decisively on the result of Corollary 3.1. While by preliminary tests it had turned out that the amount of numerical viscosity is insufficient for the usual choice

$$\alpha_k = \max\big\{\big|\lambda_k\big(\mathcal{J}_{\boldsymbol{f}}(\Phi_i)\big)\big|, \big|\lambda_k\big(\mathcal{J}_{\boldsymbol{f}}(\Phi_{i+1})\big)\big|\big\},$$

much better results in terms of resolution an efficiency have been obtained by exploiting the interlacing property stated in the corollary. For example, for the MLB model with equal-density particles the interlacing property provides the easily computable bound

$$\max_{\Phi\in\mathcal{S}_{i+1/2}}|\lambda_k(\Phi)| \leq \alpha_k := \max\bigg\{\max_{\Phi\in\mathcal{S}_{i+1/2}}\big|v_k(\Phi)\big|, \max_{\Phi\in\mathcal{S}_{i+1/2}}\big|v_{k+1}(\Phi)\big|\bigg\}.$$

This choice of $\alpha_1, \ldots, \alpha_N$ defines the scheme SPEC-INT.

3.6. **Numerical experiments.** We here present some selected numerical examples from [78] and [96]. We refer to these papers for a detailed presentation and broader discussion. In Example 1, we consider a suspension of $N = 4$ equal-density particle species with the normalized sizes $d_1 = 1$, $d_2 = 0.8$, $d_3 = 0.6$, and $d_4 = 0.4$, and set $\phi_{\max} = 0.6$. The initial composition is $\phi_i^0 = 0.05$ for $i = 1, \ldots, 4$. Numerical results are shown in Figures 34 and 35.

Example 2 is motivated by data from [68] and concerns the settling of a suspension with $N = 7$ solid species (size classes). We consider the parameters $\phi_{\max} = 0.6$ and the hindered settling factor $V(\phi) = (1 - \phi)^3$. The initial conditions ϕ_i^0, real particle sizes d_i, and normalized squared particle sizes δ_i are given here:

i	1	2	3	4	5	6	7
$\phi_i^0[10^{-2}]$	0.2365	1.1039	3.5668	3.8776	6.0436	10.890	4.2718
$d_i\,[10^{-5}\,\mathrm{m}]$	290	250	210	170	130	90	50
δ_i	1.0000	0.7432	0.5244	0.3436	0.2010	0.0963	0.0297

We use Adaptive Mesh Refinement (AMR) to locally enhance resolution and efficiency. The final scheme is named SPEC-INT-AMR. Numerical results from [96] are shown in Figures 36 and 37.
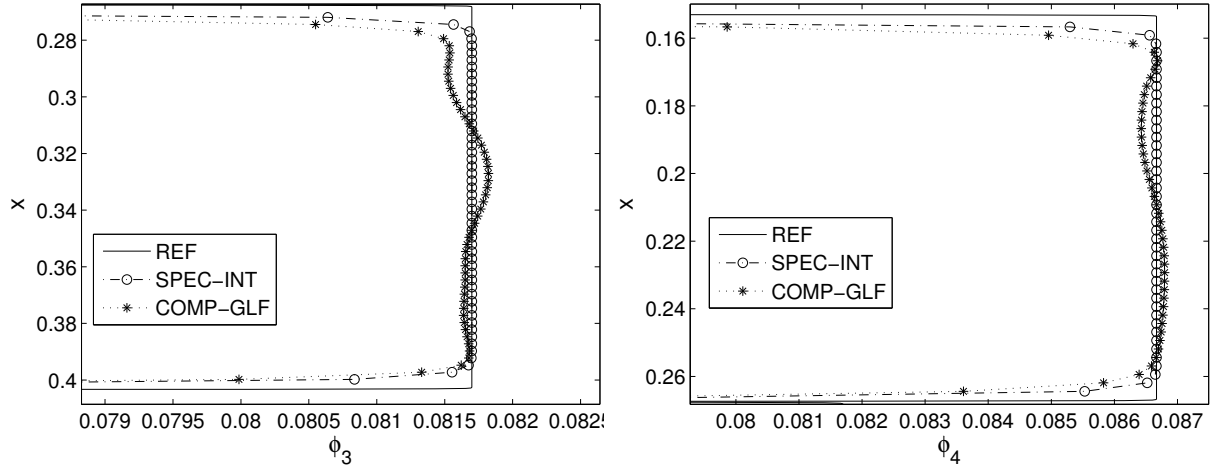
FIGURE 35. Example 1 (settling of a suspension of $N = 4$ solid species): solution for ϕ_3 and ϕ_4 with $M = 400$ at simulated time $t = 50\,\mathrm{s}$ [78].
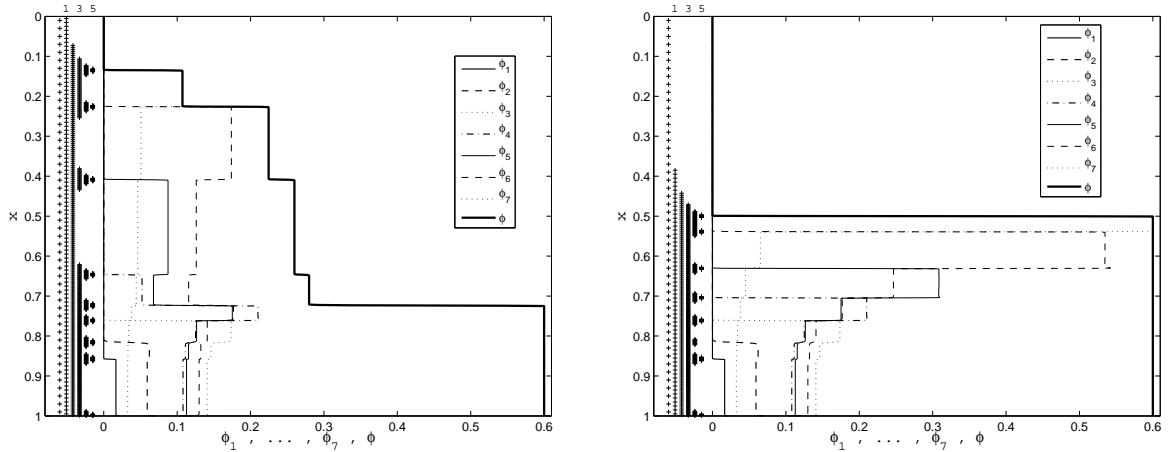
FIGURE 36. Example 2 (settling of a suspension of $N = 7$ solid species): numerical solutionx at $t = 400\,\mathrm{s}$ and $t = 2500\,\mathrm{s}$ obtained by SPEC-INT-AMR with $L + 1 = 6$ levels; the coarsest grid has 50 subintervals [96].

3.7. **Implicit-explicit (IMEX) methods for a diffusively corrected model.** The diffusively corrected model (including the effect of sediment compressibility) leads to a strongly degenerate hyperbolic-parabolic system of PDEs (DCM). Explicit schemes applied to the model require the strong stability step size constraint

$$\alpha \frac{\Delta t}{\Delta x} + \beta \frac{\Delta t}{\Delta x^2} \leq 1,$$

which is avoided by so-called implicit-explicit Runge-Kutta (IMEX-RK) discretizations that are implicit for diffusive term and explicit for the convective term, both of the semi-discrete (spatially discretized) formulation. In [97] the authors developed a new nonlinear solver for the regularization
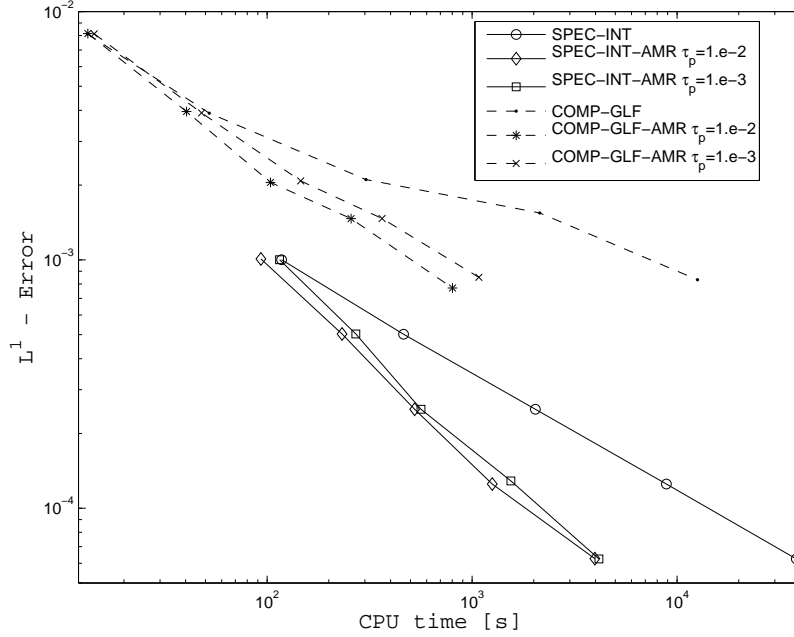
FIGURE 37. Example 2 (settling of a suspension of $N = 7$ solid species): approximate L^1 errors versus CPU time for SPEC-INT-AMR and COMP-GLF-AMR at $t = 2500\,\mathrm{s}$. The referece solution was computed with SPEC-INT on a fixed grid with 12800 subintervals [96].

of the algebraic systems arising with IMEX methods. Alternatively, one can design linearly implicit (less accurate, but easier to implement) IMEX-RK schemes to solve the problem [84, 85].

3.8. **Spatial discretization.** The spatial discretization of (DCM) is achieved through discretizing $\partial_x \boldsymbol{f}(\Phi)$ discretized by $\frac{1}{\Delta x}(\Delta^- \boldsymbol{f})(\boldsymbol{\Phi})$, where the numerical flux is a fifth-order WENO reconstructions of characteristic fluxes (WENO-SPEC or SPEC-INT, see Section 3.5 and [78]). Moreover, $\partial_x(\boldsymbol{B}(\Phi)\partial_x\Phi)$ is discretized by a standard second-order scheme, i.e.,

$$\partial_x\big(\boldsymbol{B}(\Phi)\partial_x\Phi\big)(x_i,t) \approx \frac{1}{\Delta x^2}\big(\boldsymbol{B}_{i-1/2}\boldsymbol{\Phi}_{i-1} - (\boldsymbol{B}_{i-1/2} + \boldsymbol{B}_{i+1/2})\boldsymbol{\Phi}_i + \boldsymbol{B}_{i+1/2}\boldsymbol{\Phi}_{i+1}\big)(t),$$

$$\boldsymbol{B}_{i+1/2} := \frac{1}{2}\big(\boldsymbol{B}(\boldsymbol{\Phi}_i) + \boldsymbol{B}(\boldsymbol{\Phi}_{i+1})\big), \quad \boldsymbol{\Phi}_i(t) \approx \Phi(x_i,t) \in \mathbb{R}^N;$$

Modifications to these formulas apply for $i = 1$ and $i = M$ to account for boundary conditions. BCs. For $\boldsymbol{\Phi} = (\boldsymbol{\Phi}_1, \ldots, \boldsymbol{\Phi}_M)^{\mathrm{T}} \in \mathbb{R}^{MN}$, we can now define the $M \times M$ block tridiagonal matrix $\boldsymbol{\mathcal{B}} = \boldsymbol{\mathcal{B}}(\boldsymbol{\Phi})$, with blocks of size $N \times N$, as $\boldsymbol{\mathcal{B}}_{i,i} = -(\boldsymbol{B}_{i-1/2} + \boldsymbol{B}_{i+1/2})$, $\boldsymbol{\mathcal{B}}_{i,i-1} = \boldsymbol{B}_{i-1/2}$, etc.

3.9. **Time discretization.** Within Semi-implicit IMEX-RK schemes, the convective term is treated explicitly, and the diffusive term is treated implicitly. One combines explicit Runge-Kutta (ERK) scheme with a diagonally implicit Runge-Kutta (DIRK) scheme to handle the former and the latter, respectively. Both schemes are assumed to be given by the usual Butcher arrays, that is

$$\frac{\tilde{\boldsymbol{c}} \mid \tilde{\boldsymbol{A}}}{\mid \tilde{\boldsymbol{B}}^{\mathrm{T}}} = s\text{-stage ERK}, \qquad \frac{\boldsymbol{c} \mid \boldsymbol{A}}{\mid \boldsymbol{B}^{\mathrm{T}}} = s\text{-stage DIRK}.$$

A common example is the second-order scheme IMEX-SSP2(3,3,2) (see [98]):

$$\frac{\tilde{\boldsymbol{c}}\;\big|\;\tilde{\boldsymbol{A}}}{\big|\;\tilde{\boldsymbol{B}}^{\mathrm{T}}} = \begin{array}{c|ccc} 0 & 0 & 0 & 0 \\ \frac{1}{2} & \frac{1}{2} & 0 & 0 \\ 1 & \frac{1}{2} & \frac{1}{2} & 0 \\ \hline & \frac{1}{3} & \frac{1}{3} & \frac{1}{3} \end{array}, \qquad \frac{\boldsymbol{c}\;\big|\;\boldsymbol{A}}{\big|\;\boldsymbol{B}^{\mathrm{T}}} = \begin{array}{c|ccc} \frac{1}{4} & \frac{1}{4} & 0 & 0 \\ \frac{1}{4} & 0 & \frac{1}{4} & 0 \\ 1 & \frac{1}{3} & \frac{1}{3} & \frac{1}{3} \\ \hline & \frac{1}{3} & \frac{1}{3} & \frac{1}{3} \end{array}.$$

Nonlinearly implicit IMEX-RK (NI-IMEX-RK) methods (as studied in [97]) are based on the semidiscrete formulation rewritten as follows:

$$\frac{\mathrm{d}\boldsymbol{\Phi}}{\mathrm{d}t} = C(\boldsymbol{\Phi}) + D(\boldsymbol{\Phi}),$$

$$C(\boldsymbol{\Phi}) := -\frac{1}{\Delta x}(\Delta^{-}\boldsymbol{f})(\boldsymbol{\Phi}), \quad D(\boldsymbol{\Phi}) := \frac{1}{\Delta x^{2}}\boldsymbol{\mathcal{B}}(\boldsymbol{\Phi})\boldsymbol{\Phi},$$

where $C(\boldsymbol{\Phi})$ and $D(\boldsymbol{\Phi})$ represent the spatial discretizations of the convective and diffusive parts of (DCM), respectively. For this setting the simplest IMEX scheme is

$$\boldsymbol{\Phi}^{n+1} = \boldsymbol{\Phi}^{n} - \frac{\Delta t}{\Delta x}(\Delta^{-}\boldsymbol{f})(\boldsymbol{\Phi}^{n}) + \frac{\Delta t}{\Delta x^{2}}\boldsymbol{\mathcal{B}}(\boldsymbol{\Phi}^{n+1})\boldsymbol{\Phi}^{n+1},$$

where $\boldsymbol{\Phi}^{n} \approx \boldsymbol{\Phi}(t^{n})$. For general pairs of RK schemes, the computations of a NI-IMEX-RK scheme necessary to advance an $\boldsymbol{\Phi}^{n}$ from time t^{n} to $t^{n+1} = t^{n} + \Delta t$ are given in the following algorithm:

> Input: approximate solution vector $\boldsymbol{\Phi}^{n}$ for $t = t_{n}$
> **do** $i = 1, \ldots, s$
>   solve for $\boldsymbol{\Phi}^{(i)}$ the nonlinear equation
> $$\boldsymbol{\Phi}^{(i)} = \boldsymbol{\Phi}^{n} + \Delta t\left(\sum_{j=1}^{i-1} a_{ij}K_{j} + a_{ii}D(\boldsymbol{\Phi}^{(i)}) + \sum_{j=1}^{i-1}\tilde{a}_{ij}\tilde{K}_{j}\right)$$
> $K_{i} \leftarrow D(\boldsymbol{\Phi}^{(i)}),\ \tilde{K}_{i} \leftarrow C(\boldsymbol{\Phi}^{(i)})$
> **enddo**
> $$\boldsymbol{\Phi}^{n+1} \leftarrow \boldsymbol{\Phi}^{n} + \Delta t\sum_{j=1}^{s} b_{j}K_{j} + \Delta t\sum_{j=1}^{s}\tilde{b}_{j}\tilde{K}_{j}$$
> Output: approximate solution vector $\boldsymbol{\Phi}^{n+1}$ for $t = t^{n+1} = t^{n} + \Delta t$.

This algorithm [99] requires in each step solving a nonlinear system of the type

$$\boldsymbol{\Psi}_{i}(\boldsymbol{u}) := \boldsymbol{u} - a_{ii}\Delta t D(\boldsymbol{u}) - \boldsymbol{r}_{i} = \boldsymbol{0}, \quad i = 1, \ldots, s,$$

for $\boldsymbol{u} = \boldsymbol{\Phi}^{(i)} \in \mathbb{R}^{MN}$, where

$$\boldsymbol{r}_{i} = \boldsymbol{\Phi}^{n} + \Delta t\left(\sum_{j=1}^{i-1} a_{ij}K_{j} + \sum_{j=1}^{i-1}\tilde{a}_{ij}\tilde{K}_{j}\right).$$

To apply the standard Newton-Raphson iterative method, one must require that the function $\boldsymbol{B}$ or $\boldsymbol{\mathcal{B}}$ is at least of class C^{1}. However, our degenerate model does not naturally satisfy this assumption. To this end, we devised NI-IMEX-RK schemes [97] that are based on replacing $\boldsymbol{B}$ by smooth approximation $\boldsymbol{B}_{\varepsilon}$ (and $\boldsymbol{\mathcal{B}}$ by $\boldsymbol{\mathcal{B}}_{\varepsilon}$), where $\boldsymbol{B}_{\varepsilon} \to \boldsymbol{B}$ and $\boldsymbol{\mathcal{B}}_{\varepsilon} \to \boldsymbol{\mathcal{B}}$ as $\varepsilon \to 0$. One then applies a nonlinear solver combined with smoothing and a damped Newton-Raphson method with line search strategy (see [97] for details).

The necesessity to solve nonlinear algebraic systems within each IMEX step circumvented by linearly implicit Runge-Kutta methods (LI-IMEX-RK methods). To formulate them, we start from the semidiscrete formulation in the form

$$\frac{\mathrm{d}\boldsymbol{\Phi}}{\mathrm{d}t} = \mathcal{C}(\boldsymbol{\Phi}) + \mathcal{D}(\boldsymbol{\Phi}, \boldsymbol{\Phi}),$$

$$\mathcal{C}(\boldsymbol{\Phi}) := -\frac{1}{\Delta x}(\Delta^- \boldsymbol{f})(\boldsymbol{\Phi}), \quad \mathcal{D}(\boldsymbol{\Phi}^*, \boldsymbol{\Phi}) := \frac{1}{\Delta x^2}\boldsymbol{\mathcal{B}}(\boldsymbol{\Phi}^*)\boldsymbol{\Phi},$$

where we distinguish between stiff and nonstiff dependence on $\boldsymbol{\Phi}$ in the spatially discretized form $\mathcal{D}(\boldsymbol{\Phi}^*, \boldsymbol{\Phi})$ of the diffusion term. We write

$$\frac{\mathrm{d}\boldsymbol{\Phi}}{\mathrm{d}t} = \mathcal{C}(\boldsymbol{\Phi}^*) + \mathcal{D}(\boldsymbol{\Phi}^*, \boldsymbol{\Phi}) =: \mathcal{K}(\boldsymbol{\Phi}^*, \boldsymbol{\Phi}),$$

where $\boldsymbol{\Phi}^*$ is treated explicitly as argument of $\boldsymbol{f}$ and $\boldsymbol{\mathcal{B}}$, while $\boldsymbol{\Phi}$ is implicit in the term to which $\boldsymbol{\mathcal{B}}$ is applied. The simplest first-order LI-IMEX-RK scheme is then given by

$$\boldsymbol{\Phi}^{n+1} = \boldsymbol{\Phi}^n - \frac{\Delta t}{\Delta x}(\Delta^- \boldsymbol{f})(\boldsymbol{\Phi}^n) + \frac{\Delta t}{\Delta x^2}\boldsymbol{\mathcal{B}}(\boldsymbol{\Phi}^n)\boldsymbol{\Phi}^{n+1}.$$

In the general case, a linearly implicit IMEX-RK scheme is defined by the following algorithm:

Input: approximate solution vector $\boldsymbol{\Phi}^n$ for $t = t^n$

do $i = 1, \ldots, s$

$$\boldsymbol{\Phi}^{*(i)} \leftarrow \boldsymbol{\Phi}^n + \Delta t \sum_{j=1}^{i-1} \tilde{a}_{ij} K_j, \quad \hat{\boldsymbol{\Phi}}^{(i)} \leftarrow \boldsymbol{\Phi}^n + \Delta t \sum_{j=1}^{i-1} a_{ij} K_j$$

solve for K_i the linear equation

$$K_i = \mathcal{C}\big(\boldsymbol{\Phi}^{*(i)}\big) + \frac{1}{\Delta x^2}\boldsymbol{\mathcal{B}}\big(\boldsymbol{\Phi}^{*(i)}\big)\big(\hat{\boldsymbol{\Phi}}^{(i)} + \Delta t a_{ii} K_i\big), \qquad (*)$$

enddo

$$\boldsymbol{\Phi}^{n+1} \leftarrow \boldsymbol{\Phi}^n + \Delta t \sum_{j=1}^{s} b_j K_j \qquad (**)$$

Output: approximate solution vector $\boldsymbol{\Phi}^{n+1}$ for $t = t^{n+1} = t^n + \Delta t$.

The property $\boldsymbol{\Phi}^{*,n+1} = \boldsymbol{\Phi}^{n+1}$ is guaranteed for $b_i = \tilde{b}_i$ for $i = 1, \ldots, s$ [100].

3.10. **Numerical experiments.** We compare numerical results with those obtained from the well-known explicit Kurganov-Tadmor (KT) scheme [101]. We set $\Delta x = L/M$ and in each iteration, the time step Δt is determined by

$$\frac{\Delta t}{\Delta x} \max_{1 \leq j \leq M} \varrho\big(\mathcal{J}_{\boldsymbol{f}}\big(\Phi_j^n\big)\big) + \frac{\Delta t}{2\Delta x^2} \max_{1 \leq j \leq M} \varrho\big(\boldsymbol{B}\big(\Phi_j^n\big)\big) = C_{\mathrm{cfl}_1}$$

for the KT scheme and

$$\frac{\Delta t}{\Delta x} \max_{1 \leq j \leq M} \varrho\big(\mathcal{J}_{\boldsymbol{f}}\big(\Phi_j^n\big)\big) = C_{\mathrm{cfl}_2}$$

for the semi-implicit schemes, where $\varrho(\cdot)$ is the spectral radius. In the numerical examples we choose C_{cfl_*} as the largest multiple of 0.05 that yields oscillation-free numerical solutions. In all cases, the reference solution for numerical tests is computed by the KT scheme with $M_{\mathrm{ref}} = 25600$. The numerical examples are based on the results of [84, 85].

In Example 3 we consider $N = 3$ and focus on the comparison of LI- and NI-IMEX-SSP2 schemes, based on using the model parameters $\phi_{\mathrm{max}} = 0.66$, $n_{\mathrm{RZ}} = 4.7$, $\sigma_0 = 180 \, \mathrm{Pa}$, $\phi_c = 0.2$, $k = 2$, $\mu_{\mathrm{f}} = 10^{-3} \, \mathrm{Pa\,s}$, $d = 1.19 \times 10^{-5} \, \mathrm{m}$, $\overline{\rho}_{\mathrm{s}} = 1800 \, \mathrm{kg/m^3}$, and $g = 9.81 \, \mathrm{m/s^2}$. The initial
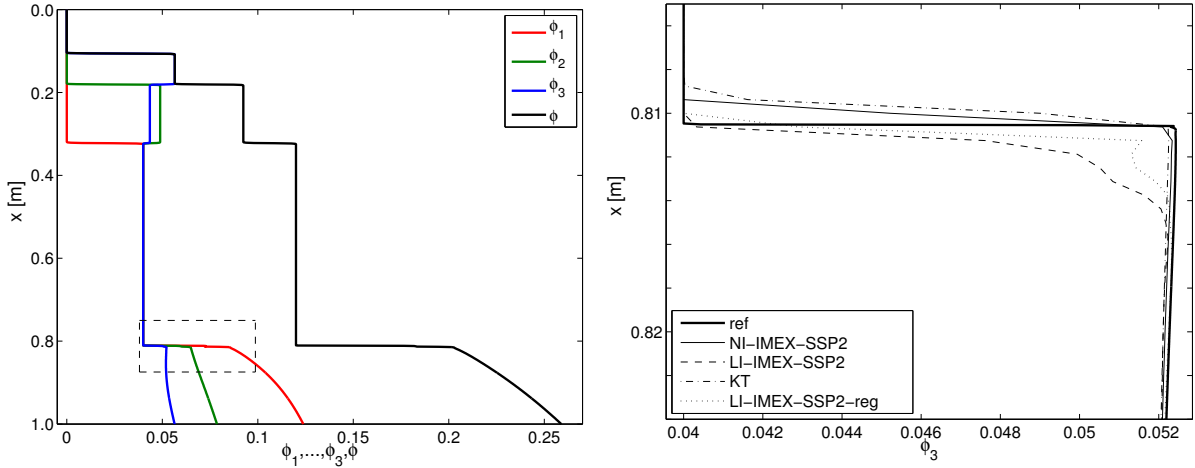
FIGURE 38. Example 3 (settling of a tridisperse suspension ($N = 3$), including the effect of sediment compressibility): (left) numerical results by LI-IMEX-SSP2 at simulated time $T = 4000\,\mathrm{s}$, (right) enlarged view [84, 85].

FIGURE 39. Example 3 (settling of a tridisperse suspension ($N = 3$), including the effect of sediment compressibility): numerical solution at simulated time $T = 4000\,\mathrm{s}$, efficiency plot based on numerical results for $\Delta x = 1/M$ with $M = 100,\ 200,\ 400,\ 800$ and 1600 [84, 85].

concentration is $\Phi_0 = (0.04, 0.04, 0.04)^{\mathrm{T}}$ in a vessel of height $\mathcal{L} = 1\,\mathrm{m}$ with $\boldsymbol{\delta} = (1, 0.5, 0.25)^{\mathrm{T}}$. For
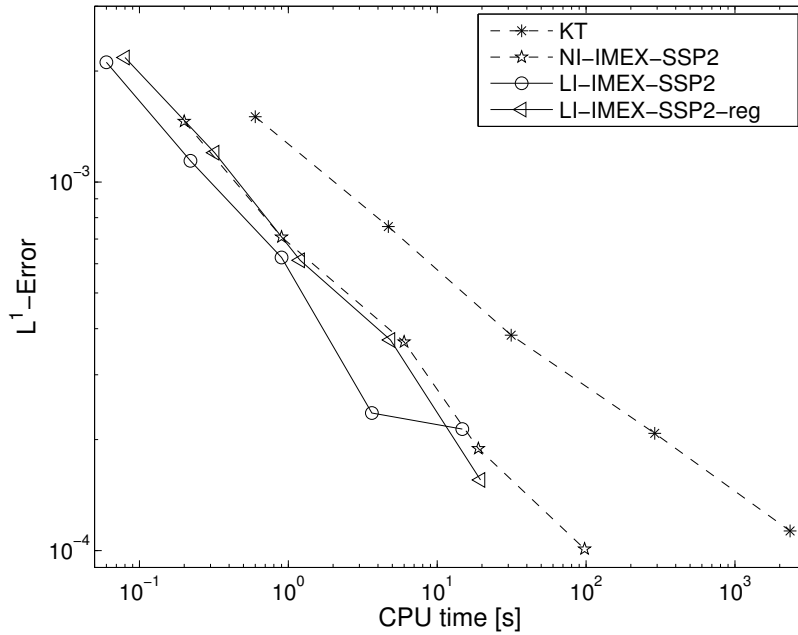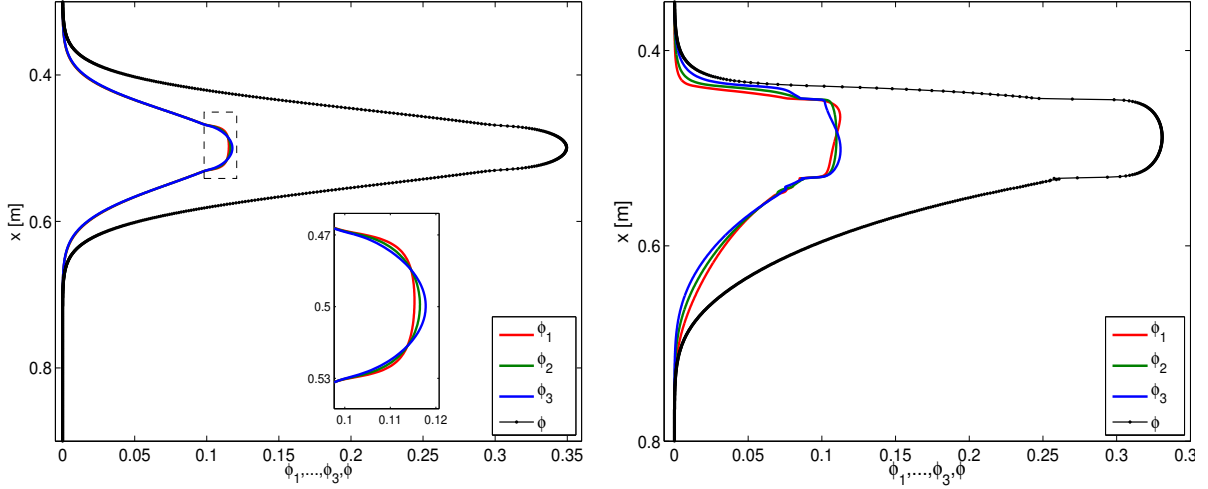
FIGURE 40. Example 4: (settling of a tridisperse suspension ($N = 3$), including the effect of sediment compressibility, smooth initial datum): numerical results produced by LI-IMEX-SSP2-reg with $M = 1600$ at simulated times (left) $T = 20\,\mathrm{s}$ and (right) $T = 500\,\mathrm{s}$ [84].

the nonlinearly implicit scheme, NI-IMEX-SSP2, the regularization is achieved by utilizing

$$\sigma_{\mathrm{e}}(\phi; \varepsilon) = \sigma_{\mathrm{e}}(\phi) \exp\big(-\varepsilon/(\phi - \phi_{\mathrm{c}})^2\big), \quad \varepsilon > 0,$$

where ε decreases gradually from $\varepsilon_0 = 10^{-4}$ to $\varepsilon_{\min} = 10^{-6}$, tol $= 10^{-8}$. The schemes LI-IMEX-SSP2 and KT do not include regularization of the diffusive term. For the schemes NI-IMEX-SSP2 and LI-IMEX-SSP2, we set $C_{\mathrm{cfl}_2} = 0.7$, and for KT, $C_{\mathrm{cfl}_1} = 0.25$. The scheme LI-IMEX-SSP2-reg consists in applying the scheme LI-IMEX-SSP2 to the regularized diffusion term with $\varepsilon_{\min} = 10^{-6}$.

In Example 4 we again consider $N = 3$ and the parameters $d_1 = 1.0$, $d_2 = 0.8$ and $d_3 = 0.7$, with a smooth initial concentration profile $\phi_i(x) = 0.12 \exp(-200(x - 0.5)^2)$. The numerical results produced by the scheme LI-IMEX-SSP2-reg with $M = 1600$ are taken at $T = 20\,\mathrm{s}$ (when the solution profiles are still smooths) and $T = 500\,\mathrm{s}$ (after discontinuities have formed). The corresponding numerical errors are given here [84]:

|	$T = 20\,\mathrm{s}$				$T = 500\,\mathrm{s}$	
	based on reference soln.		based on interpolation		based on reference soln.	
M	$e_M^{\mathrm{tot}}(T)$	$\theta_M(T)$	$\hat{\theta}_M(T)$	$\tilde{e}_M^{\mathrm{tot}}(T)$	$e_M^{\mathrm{tot}}(T)$	$\theta_M(T)$
50	1.38e-04	0.14	-0.33	8.41e-05	2.27e-03	1.59
100	1.25e-04	1.45	1.48	1.06e-04	7.49e-04	0.95
200	4.58e-05	1.80	1.68	3.80e-05	3.86e-04	1.11
400	1.30e-05	1.88	1.76	1.19e-05	1.78e-04	0.91
800	3.54e-06	1.87	1.87	3.52e-06	9.49e-05	1.05
1600	9.66e-07	2.00	1.98	9.63e-07	4.56e-05	1.01
3200	2.40e-07	2.06	—	2.44e-07	2.26e-05	1.01
6400	5.73e-08	—	—	—	1.12e-05	—
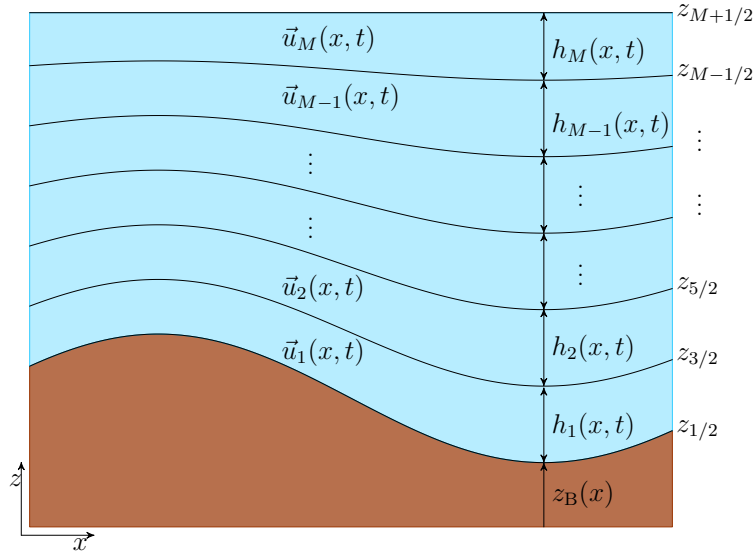
FIGURE 41. Multilayer approach for one horizontal and one vertical space dimension (coordinates x and z, respectively) [103].

3.11. **A multilayer shallow water system of polydisperse sedimentation.** Models for the settling of a polydisperse suspensions in two or three space dimensions are usually given by (3.1)–(3.3) or a similar coupled transport-flow problem. Roughly speaking, such problems are defined by a transport equation (for the solids concentrations) strongly coupled to a version of the Navier-Stokes equation for the mixture velocity and the pressure. Since the computational effort to solve these multi-dimensional coupled problems is considerable, one seeks to define easier-to-solve lower-dimensional models. The well-known Saint-Venant (shallow water) approach is based on a vertically integrated version of the flow equations that can be applied when vertical fluctuations of variables are negligible.

To handle mostly horizontal flows combined with polydisperse sedimentation, a new computational multilayer Saint-Venant approach was developed [102] and recently modified [103]. In general, a multilayer Saint-Venant model is less expensive than the full 3D model from the computational point of view, but still keeps information on the vertical distribution of the mixture. Such an approach (as opposed to a standard single-layer approach) is appropriate in the presence large friction coefficients, significant water depth, or wind effects [104–106]. This approach results in a number of coupled Saint-Venant system, one for each layer [107], see Figure 41.

The steps of the formulation of the final solvable multiplayer model are fairly complicated [102]. They include integrating the balance equations for the solid and liquid phases over each layer, neglecting vertical fluctuations of horizontal velocities and concentrations inside each layer, and assuming that the pressure is hydrostatic. We assume that the suspension body is subdivided into M layers. Furthermore, if $h = h(x, t)$ denotes the total height of the suspension body at horizontal position x at time t, then we assume that the height of layer α, $\alpha = 1, \ldots, M$, is a fixed fraction l_α of h, such that $h_\alpha = l_\alpha h$ for $l_\alpha > 0$, $\alpha = 1, \ldots, M$, with $l_1 + \cdots + l_M = 1$. We assume that the bottom and surface heights are $z_B := z_{1/2}$ and $z_S := z_{M+1/2}$, such that $h = z_S - z_B = h_1 + \cdots + h_M$. (again, see Figure 41). The governing model can then be written as follows, where $\alpha = 1, \ldots, M$

counts the layer under consideration and $j = 1, \ldots, N$ indicates the solid particle species:

$$\partial_t r_{j,\alpha} + \partial_x \left(\frac{r_{j,\alpha} q_\alpha}{m_\alpha} \right)$$

$$= \frac{1}{l_\alpha} \big(\tilde{\phi}_{j,\alpha+1/2} G_{\alpha+1/2} - \tilde{\phi}_{j,\alpha-1/2} G_{\alpha-1/2} \big) - \frac{\rho_j}{l_\alpha} \big(\tilde{f}_{j,\alpha+1/2} - \tilde{f}_{j,\alpha-1/2} \big), \quad j = 1, \ldots, N,$$

$$\partial_t q_\alpha + \partial_x \left(\frac{q_\alpha^2}{m_\alpha} + h \left(p_{\mathrm{S}} + \frac{g}{2} l_\alpha m_\alpha + g \sum_{\beta=\alpha+1}^{M} l_\beta m_\beta \right) \right)$$

$$= \left(p_{\mathrm{S}} + g \sum_{\beta=\alpha+1}^{M} l_\beta m_\beta \right) \partial_x h - g m_\alpha \partial_x z_b - g m_\alpha l_{\alpha-1} \partial_x h + \frac{1}{l_\alpha} \big(\tilde{u}_{\alpha+1/2} G_{\alpha+1/2} - \tilde{u}_{\alpha-1/2} G_{\alpha-1/2} \big),$$

$$\partial_t \bar{m} + \partial_x \left(\sum_{\beta=1}^{M} l_\beta q_\beta \right) = G_{M+1/2} - G_{1/2}, \quad \bar{m} := h \sum_{\beta=1}^{M} \bar{\rho}_\beta l_\beta = \sum_{\beta=1}^{M} l_\beta m_\beta.$$

Here $\rho_1, \ldots, \rho_N$ are the densities of the solid species, ρ_0 is the density of the fluid, g is the acceleration of gravity, $\phi_{j,\alpha}$ denotes the volume fraction of species j in layer α, $r_{j,\alpha} := \rho_j \phi_{j,\alpha} h$, u_α is the horizontal velocity of the mixture in layer α, $\bar{\rho}_\alpha := \rho_0 \phi_{0,\alpha} + \rho_1 \phi_{1,\alpha} + \cdots + \rho_N \phi_{N,\alpha}$ is the density of layer α, $q_\alpha := \bar{\rho}_\alpha h u_\alpha$, and $m_\alpha := \bar{\rho}_\alpha h$. Moreover,

$$\tilde{u}_{\alpha+1/2} := \frac{1}{2} \left(\frac{q_{\alpha+1}}{m_{\alpha+1}} + \frac{q_\alpha}{m_\alpha} \right), \quad \tilde{\phi}_{j,\alpha+1/2} := \frac{1}{2} \left(\frac{r_{j,\alpha+1}}{m_{\alpha+1}} + \frac{r_{j,\alpha}}{m_\alpha} \right),$$

and $G_{j,\alpha+1/2}$ are intra-layer mass fluxes defined inter alia by the modified MLB velocities. The model that is eventually solved can be written as a balance equation involving non-conservative products,

$$\partial_t \boldsymbol{w} + \partial_x \boldsymbol{\mathcal{F}}(\boldsymbol{w}) = \boldsymbol{\mathcal{S}}(\boldsymbol{w}, \partial_x \boldsymbol{w}) + \boldsymbol{\mathcal{G}}(\boldsymbol{w}, \partial_x \boldsymbol{w}),$$

$$\boldsymbol{w} = (\bar{m}, q_1, \ldots, q_M, r_{1,1}, \ldots, r_{N,1}, \ldots, \ldots, r_{1,M}, \ldots, r_{N,M})^{\mathrm{T}},$$

for whose numerical solution specialized numerical methods are available.

3.12. **Numerical experiments.** In the present numerical simulation we have used the global constants $g = 9.8 \, \mathrm{m/s^2}$ (acceleration of gravity), $\phi_{\max} = 0.68$, and we have employed the Richardson-Zaki hindered settling factor with $n_{\mathrm{RZ}} = 4.7$, viscosity and density of the pure fluid are $\mu_0 = 0.02416 \, \mathrm{Pa\,s}$ and $\rho_0 = 1208 \, \mathrm{kg/m^3}$, respectively, and we are assumed that the all species have the same density $\rho_1 = \rho_2 = \rho_3 = 2790 \, \mathrm{kg/m^3}$.

The (horizontal) x-interval $[0, L]$ has been discretized into C subintervals $[x_{i-1/2}, x_{i+1/2}] = [(i - 1)\Delta x, i\Delta x]$ of length $\Delta x = L/C$, centered at $x_i = (i - 1/2)\Delta x$, $i = 1, \ldots, C$, and in the vertical direction we have used $M = 10$ layers. Finally, we use

$$\frac{\Delta t}{\Delta x} \max_{1 \leq i \leq C} \max\{|S_{\mathrm{R},i+1/2}|, |S_{\mathrm{L},i+1/2}|\} = C_{\mathrm{cfl}},$$

as C_{cfl} condition, where $S_{\mathrm{R},i+1/2}$ and $S_{\mathrm{L},i+1/2}$ are the bounds of the eigenvalues. Here we have considered $C_{\mathrm{cfl}} = 0.5$.

In this numerical test we simulate polidisperse sedimentation process over a horizontal channel with a bump of length $L = 1 \, \mathrm{m}$. We use $N = 3$ solids species dispersed in a viscous fluid with diameters $d_1 = 4.96 \times 10^{-4} \, \mathrm{m}$, $d_2 = 1.25 \times 10^{-4} \, \mathrm{m}$, $d_3 = 1.0 \times 10^{-4} \, \mathrm{m}$ respectively. The bottom
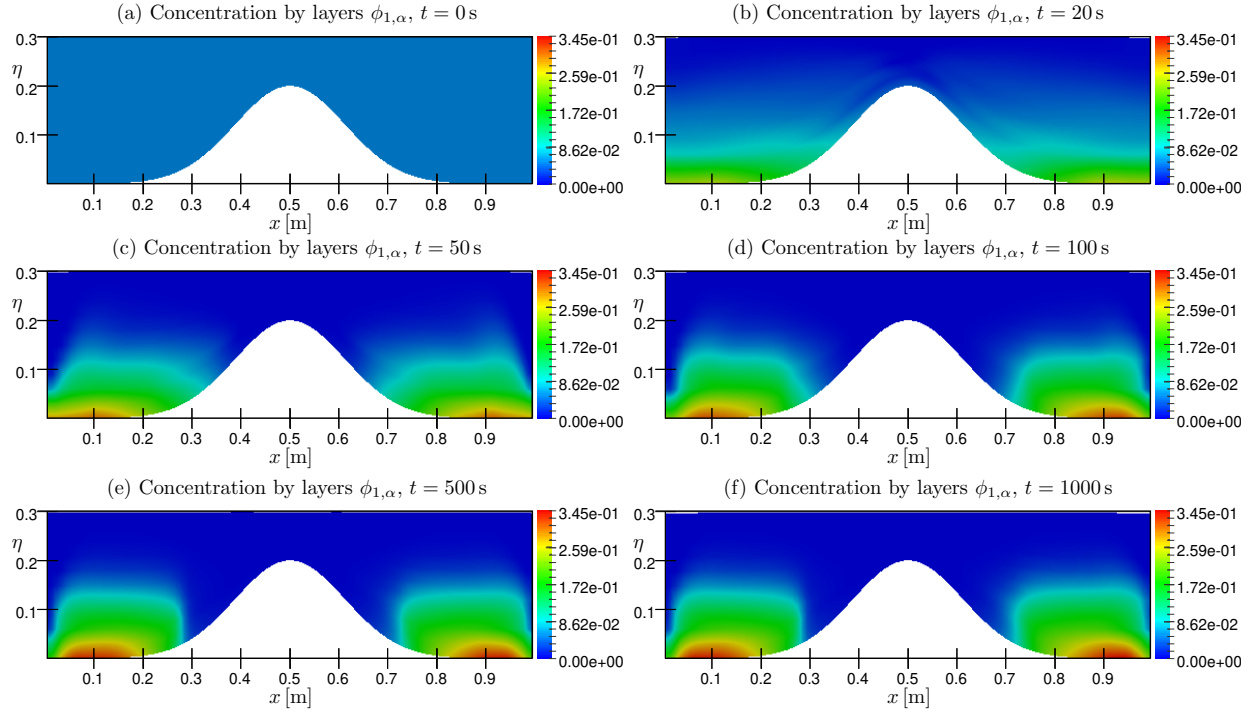
FIGURE 42. Example 5: Concentration of ϕ_1 by color in a domain with a bump, $\eta(x) = z_\mathrm{B}(x) + h(x)\,\mathrm{m}$, at simulated times $T = 0\,\mathrm{s}$, $20\,\mathrm{s}$, $50\,\mathrm{s}$, $100\,\mathrm{s}$, $500\,\mathrm{s}$ and $T = 1000\,\mathrm{s}$.

elevation is given by $z_\mathrm{B}(x) = 0.2\exp(-40(x-0.5)^2)\,\mathrm{m}$ for $x \in [0, L]$, the initial condition for the height is $h(t=0) = 0.3 - z_\mathrm{B}$, and for the concentration of each species

$$\phi_{i,\alpha} = \frac{1}{M}\sum_{\beta=1}^{M}\phi_{i,\beta}(0,x) \quad \text{for all } i = 1,\ldots,3,\ u_\alpha(0,x) = 0 \quad \text{for all } \alpha = 1,\ldots,M \text{ and all } x \in [0, L],$$

with $\sum_{\beta=1}^{M}\phi_{1,\beta}(0,x) = 0.05$, $\sum_{\beta=1}^{M}\phi_{2,\beta}(0,x) = 0.025$, $\sum_{\beta=1}^{M}\phi_{3,\beta}(0,x) = 0.01$. The sediment concentrations are vertically uniformly distributed at each point x. We use a closed basin as boundary condition.

In Figures 42–44 we can see the concentrations of the each solid species ϕ_1, ϕ_2, ϕ_3 respectively. The behavior of the particles of the different species is what we expected, the bigger particles are deposited faster than other particles over the bottom, in this case to both sides of the bump, where we can find high concentration of species 1 (ϕ_1) in short time, as we can see in Figures 42 (a)–(f). The others smaller particles initially remain in suspension, but at larger simulated times these particles begin to settle and position itself in places where the concentration of species 1 is small (see Figures 43 and 44). Finally the global behavior of all particles dispersed in the fluid (the sum of the concentrations of the all species) and the velocity field is displayed in Figure 45, in this picture, we can see how these are deposited on the bottom in both side of the bump and also as some particles of species 2 and species 3 are kept in suspension in small concentration yet. In the same figure we show the velocity field of the mixture and its magnitude, which is a consequence of the particles movement. Recirculations appear to both sides of the bump too. In the first times high
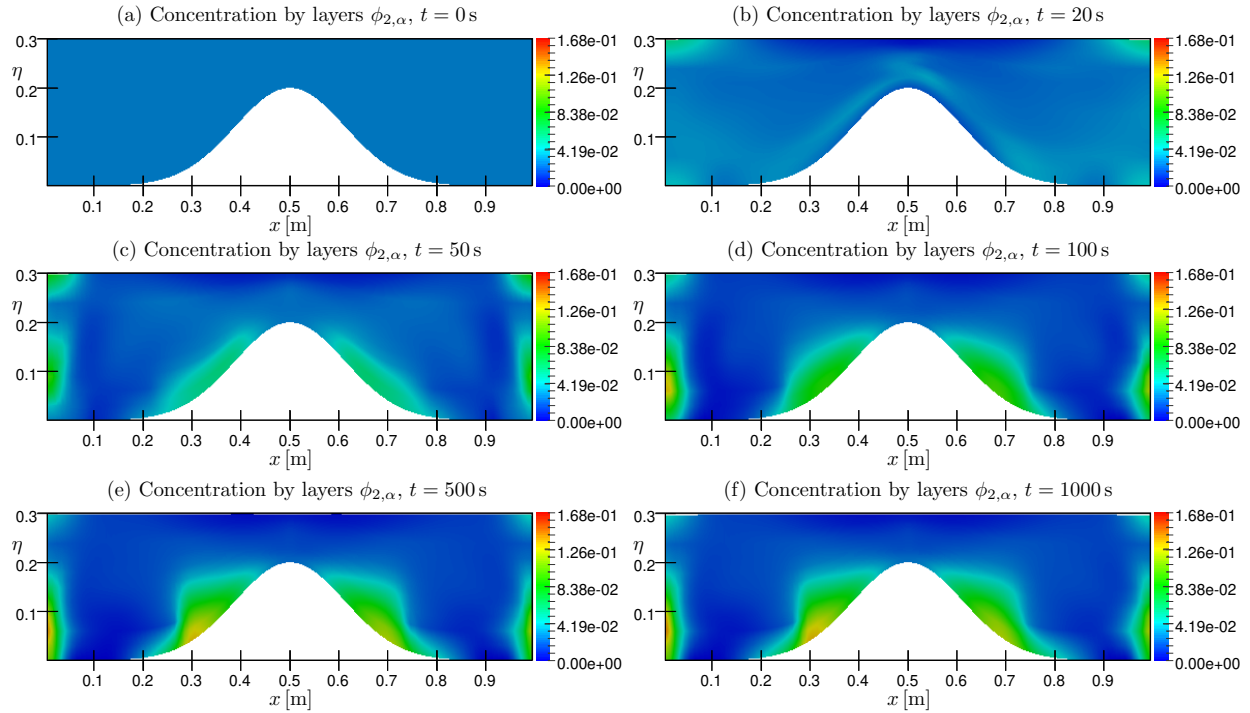
FIGURE 43. Example 6: Concentration of ϕ_2 by color in a domain with a bump, $\eta(x) = z_{\mathrm{B}}(x) + h(x)\,\mathrm{m}$, at simulated times $T = 0\,\mathrm{s}$, $20\,\mathrm{s}$, $50\,\mathrm{s}$, $100\,\mathrm{s}$, $500\,\mathrm{s}$ and $T = 1000\,\mathrm{s}$.

velocities appear avoiding that some particles settle rapidly. At larger times the velocity decreases and the particles settle.

3.13. **Conclusions on this section.** To conclude this contribution, we mention that the issue of hyperbolicity, outlined in Section 3.3, is still an open problem for some important models of polydisperse sedimentation, including the model by Patwardhan and Tien [108] which is supported by some experimental evidence. On the other hand, the schemes developed for one-dimensional sedimentation can also be applied to other models, for instance to mult-class extensions of the well-known Lighthill-Whitham-Richards kinematic traffic model (see [83, 109]). The latter models form a case of the theory of Section 3.3 for $m = 1$, and admit a separable entropy so that even entropy-stable schemes can be defined [110]. However, no entropy function is known for polydisperse sedimentation models shown here. The mathematical theory is still incomplete.

No well-posedness theory is available for strongly degenerate convection-diffusion systems of the type (DCM). In fact, the IMEX-RK approach is justified by convergence of the scheme to the same solutions that are approximate by the KT scheme.

We metion that the multilayer shallow water system for polydisperse sedimentation is currently being extended to two horizontal space dimensions. The current model should be furthermore be refined by mechanisms of sediment erosion and variation of topography due to sediment deposit.
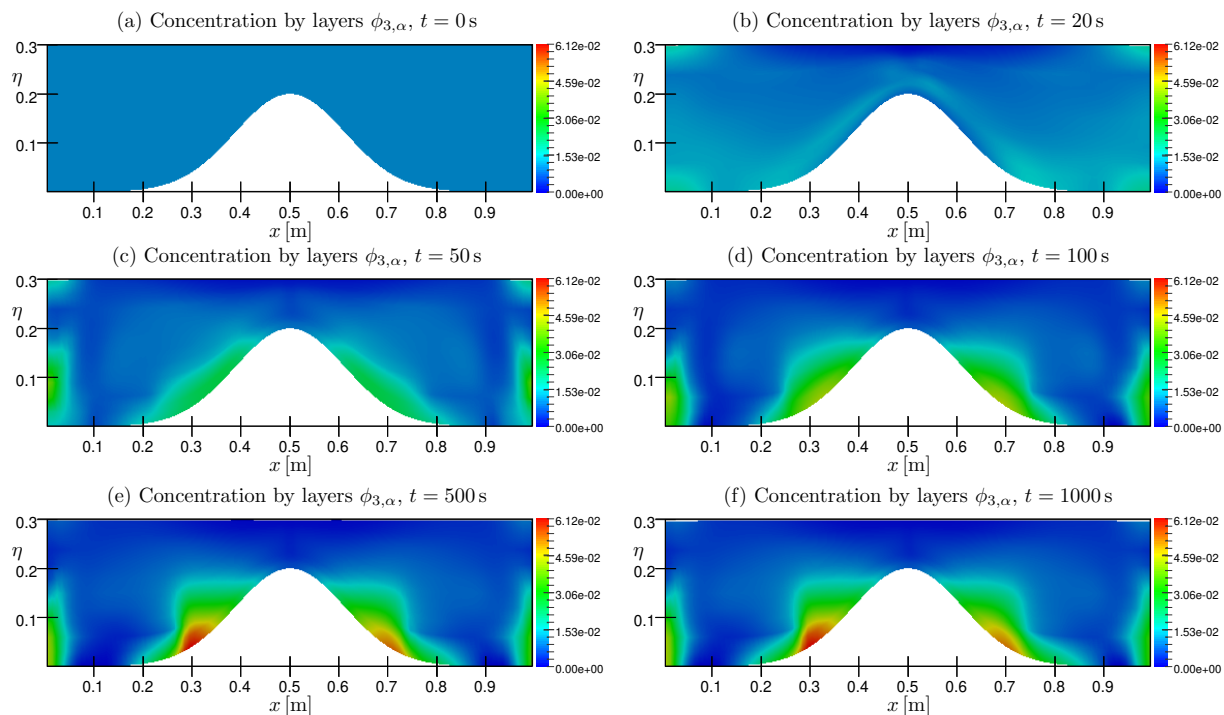
(a) Concentration by layers $\phi_{3,\alpha}$, $t = 0\,\text{s}$

(b) Concentration by layers $\phi_{3,\alpha}$, $t = 20\,\text{s}$

(c) Concentration by layers $\phi_{3,\alpha}$, $t = 50\,\text{s}$

(d) Concentration by layers $\phi_{3,\alpha}$, $t = 100\,\text{s}$

(e) Concentration by layers $\phi_{3,\alpha}$, $t = 500\,\text{s}$

(f) Concentration by layers $\phi_{3,\alpha}$, $t = 1000\,\text{s}$

FIGURE 44. Example 7: Concentration of ϕ_3 by color in a domain with a bump, $\eta(x) = z_{\text{B}}(x) + h(x)\,\text{m}$, at simulated times $T = 0\,\text{s}$, $20\,\text{s}$, $50\,\text{s}$, $100\,\text{s}$, $500\,\text{s}$ and $T = 1000\,\text{s}$.

REFERENCES

[1] R. Bürger and W.L. Wendland, Sedimentation and suspension flows: Historical perspective and some recent developments, *J. Eng. Math.* **41** (2001), 101–116. f

[2] F. Concha and R. Bürger, A century of research in sedimentation and thickening, *KONA Powder and Particle* **20** (2002), 38–70.

[3] A.J. Wilson, *The Living Rock*, Woodhead Publishing, Cambridge, 1994.

[4] J.V.N. Dorr, The use of hydrometallurgical apparatus in chemical engineering, *J. Ind. Eng. Chem.* **7** (1915), 119–130.

[5] J.V.N. Dorr, The advantageous use of continuous operation, *Chem. Met. Eng.* **31** (1924), 463–464.

[6] J.V.N. Dorr, *Cyanidation and Concentration of Gold and Silver Ores*, McGraw-Hill Book Co. Inc., New York, 1936.

[7] H.S. Coe and G.H. Clevenger, Methods for determining the capacity of slimesettling tanks, *Trans. AIME* **55** (1916), 356–385.

[8] G.G. Stokes, On the effect of the internal friction on the motion of pendulums, *Trans. Cambridge Phil. Soc.* **9** (1851), 8–106.

[9] A. Einstein, Eine neue Bestimmung der Moleküeldimensionen, *Ann. Phys.* **19** (1906), 289–306; A. Einstein, Berichtigung zu meiner Arbeit: "Eine neue Bestimmung ...", *Ann. Phys.* **34** (1911), 591–592.

[10] H.H. Steinour, Rate of sedimentation. Nonflocculated suspensions of uniform spheres, *Ind. Engrg. Chem.* **36** (1944), 618–624.

[11] H.H. Steinour, Rate of sedimentation. Suspensions of uniform-size angular particles, *Ind. Engrg. Chem.* **36** (1944), 840–847.

[12] H.H. Steinour, Rate of sedimentation. Concentrated flocculated suspensions of powders, *Ind. Engrg. Chem.* **36** (1944), 901–907.
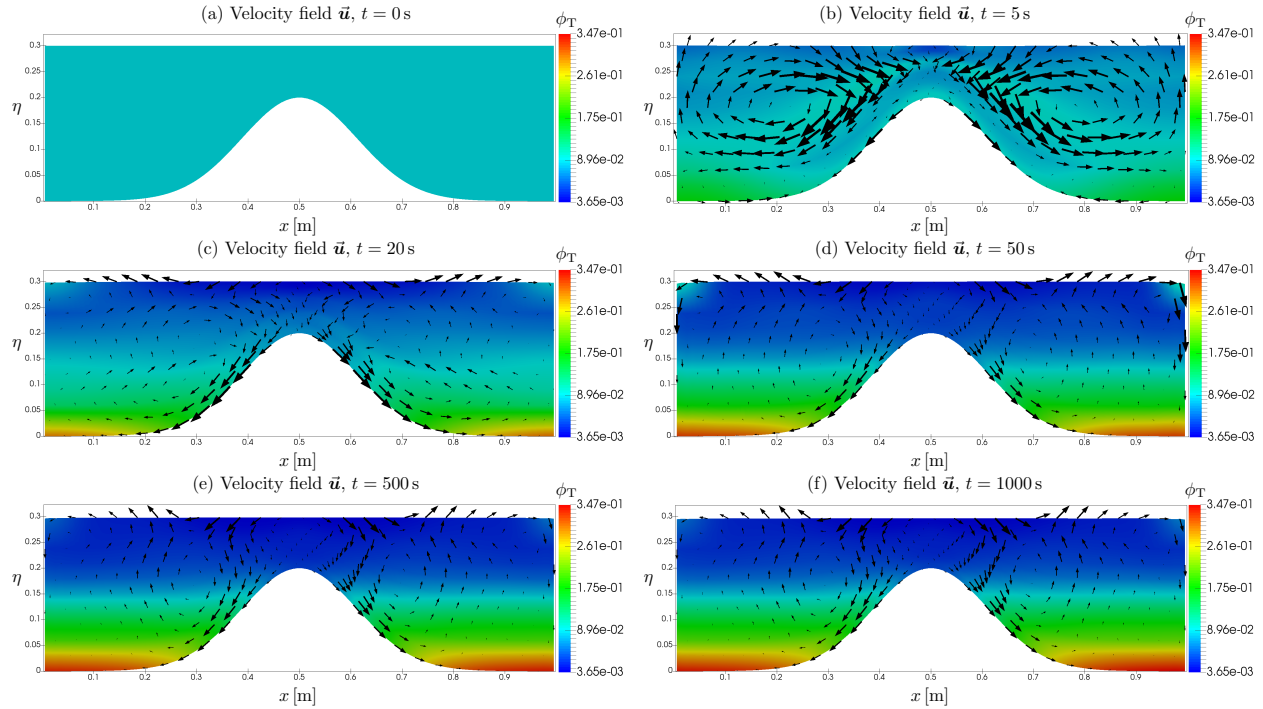
FIGURE 45. Example 8: Velocity field $\vec{u}$ over concentration $\phi_{\mathrm{T}} = \phi_1 + \phi_2 + \phi_3$, $\eta(x) = z_{\mathrm{B}}(x) + h(x)$m in different times.

[13] J.F. Richardson and W.N. Zaki, Sedimentation and fluidization: Part I, *Trans. Instn. Chem. Engrs. (London)* **32** (1954), 35–53.

[14] R. Bürger and E.M. Tory, On upper rarefaction waves in batch settling, *Powder Technol.* **108** (2000), 74–87.

[15] G.J. Kynch, A theory of sedimentation, *Trans. Farad. Soc.* **48** (1952), 166–176.

[16] P. Grassmann and R. Straumann, Entstehen und Wandern von Unstetigkeiten der Feststoffkozentration in Suspensionen, *Chem.-Ing.-Techn.* **35** (1963), 477–482.

[17] G.B. Wallis. A simplified one-dimensional representation of two-component vertical flow and its application to batch sedimentation. In: Proc. of the Symposium on the Interaction between Fluids and Particles, London, June 20–22, 1962. Institution of Chemical Engineers, London, 9–16, 1962.

[18] D.P. Ballou, Solutions to non-linear hyperbolic Cauchy problems without convexity conditions, *Trans. Amer. Math. Soc.* **152** (1970), 441–460.

[19] K.S. Cheng, Constructing solutions of a single conservation law, *J. Differential Equations* **49** (1983), 344–358.

[20] T.P. Liu, Invariants and asymptotic behavior of solutions of a conservation law, *Proc. Amer. Math. Soc.* **71** (1978), 227–231.

[21] M.C. Bustos, F. Concha, R. Bürger, and E.M. Tory, *Sedimentation and Thickening. Phenomenological Foundation and Mathematical Theory*, Kluwer Academic Publishers, Dordrecht, 1999.

[22] M.C. Bustos and F. Concha, On the construction of global weak solutions in the Kynch theory of sedimentation, *Math. Meth. Appl. Sci.* **10** (1988), 245–264.

[23] S. Diehl, *Shock Behaviour of Sedimentation in Wastewater Treatment*, M. Sc. Thesis, University of Lund, Sweden, 1988.

[24] S. Diehl, Shock-wave behaviour of sedimentation in wastewater treatment: a rich problem. In: K. Åström, L.-E. Persson, and S.D. Silvestrov (eds.), *Analysis for Science, Engineering and Beyond*, Springer Proc. in Math. 6, Springer-Verlag, Berlin, Chapter 7, 175–214.

[25] A. Coronel, F. James, and M. Sepúlveda, Numerical identification of parameters for a model of sedimentation processes, *Inverse Problems* **19** (2003), 951–972.

[26] S. Diehl, Estimation of the batch-settling flux function for an ideal suspension from only two experiments, *Chem. Eng. Sci.* **62** (2007), 4589–4601.

[27] P. Grassia, S.P. Usher, and P.J. Scales, Closed-form solutions for batch settling height from model settling flux functions. *Chem. Eng. Sci.* **66** (2011), 964–972.

[28] H.-K. Rhee, R. Aris, and N.R. Amundson, *First-Order Partial Differential Equations. Volume 1: Theory and Applications of Single Equations*, Prentice Hall, Englewood Cliffs, NJ, 1986.

[29] G.B. Wallis, *One-Dimensional Two-Phase Flow*, McGraw-Hill, 1969.

[30] S. Berres, R. Bürger, K.H. Karlsen, and E.M. Tory, Strongly degenerate parabolic-hyperbolic systems modeling polydisperse sedimentation with compression, *SIAM J. Appl. Math.* **64** (2003), 41–80.

[31] R. Bürger, W.L. Wendland and F. Concha, Model equations for gravitational sedimentation-consolidation processes, *ZAMM Z. Angew. Math. Mech.* **80** (2000), 79–92.

[32] R. Bürger, K.H. Karlsen, and J.D. Towers, A model of continuous sedimentation of flocculated suspensions in clarifier-thickener units, *SIAM J. Appl. Math.* **65** (2005), 882–940.

[33] R. Bürger and A. Narváez, Steady-state, control, and capacity calculations for flocculated suspensions in clarifier-thickeners, *Int. J. Mineral Process.* **84** (2007), 274–298.

[34] R. Bürger, P.E. Méndez, and R. Ruiz-Baier, Convergence of $\boldsymbol{H}$(div)-conforming schemes for a new model of sedimentation in circular clarifiers with a rotating rake. Preprint; submitted (2019).

[35] B.R. Gladman, M. Rudman, and P.J. Scales, The effect of shear on gravity thickening: Pilot scale modelling, *Chem. Eng. Sci.* **65** (2010), 4293–4301.

[36] D.R. Lester, M. Rudman, and P.J. Scales, Macroscopic dynamics of flocculated colloidal suspensions, *Chem. Eng. Sci.* **65** (2010), 6362–6378.

[37] M. Rudman, K. Simic, D.A. Paterson, P. Strode, A. Brent, and I.D. Šutalo, Raking in gravity thickeners, *Int. J. Mineral Process.* **86** (2008), 114–130.

[38] I.D. Šutalo, D.A. Paterson, and M. Rudman, Flow visualization and computational prediction in thickener rake models, *Minerals Eng.* **16** (2003), 93–102.

[39] R. Bürger, K.H. Karlsen, H. Torres, and J.D. Towers, Second-order schemes for conservation laws with discontinuous flux modelling clarifier-thickener units, *Numer. Math.* **116** (2010), 579–617.

[40] R. Bürger, S. Diehl, S. Farås, I. Nopens and E. Torfs, 'A consistent modelling methodology for secondary settling tanks: A reliable numerical method', *Water Sci. Tech.* **68** (2013), 192–208.

[41] R. Bürger, J. Careaga, S. Diehl, C. Mejías, I. Nopens, E. Torfs, and P.A. Vanrolleghem, Simulations of reactive settling of activated sludge with a reduced biokinetic model, *Computers & Chemical Eng.* **92** (2016), 216–229.

[42] R. Bürger, S. Diehl, and C. Mejías, A difference scheme for a degenerating convection-diffusion-reaction system modelling continuous sedimentation, *ESAIM: Math. Model. Numer. Anal.* **52** (2018), 365–392.

[43] S. Diehl, Continuous sedimentation of multi-component particles, *Math. Meth. Appl. Sci.* **20** (1997), 1345–1364.

[44] M. Henze, C.P.L. Grady, W. Gujer, G.V.R. Marais, and T. Matsuo. *Activated Sludge Model no. 1*, Science Technical Report no. 1. International Association for Water Quality (IAWQ), London, 1987.

[45] R. Bürger, K.H. Karlsen, N.H. Risebro, and J.D. Towers, Well-posedness in BV_t and convergence of a difference scheme for continuous sedimentation in ideal clarifier-thickener units, *Numer. Math.* **97** (2004), 25–65.

[46] K.H. Karlsen, N.H. Risebro, and J.D. Towers, Upwind difference approximations for degenerate parabolic convection-diffusion equations with a discontinuous coefficient, *IMA J. Numer. Anal.* **22** (2002), 623–664.

[47] S. Diehl, Numerical identification of constitutive functions in scalar nonlinear convection-diffusion equations with application to batch sedimentation, *Appl. Numer. Math.* **95** (2015), 154–172.

[48] R. Bürger, J. Careaga, and S. Diehl, A simulation model for settling tanks with varying cross-sectional area, *Chem. Eng. Commun.* **204** (2017), 1270–1281.

[49] R. Bürger, J.J.R. Damasceno and K.H. Karlsen, A mathematical model for batch and continuous thickening in vessels with varying cross section, *Int. J. Mineral Process.* **73** (2004), 183–208.

[50] E. Torfs, T. Maere, R. Bürger, S. Diehl, and I. Nopens, Impact on sludge inventory and control strategies using the Benchmark Simulation Model No. 1 with the Bürger-Diehl settler model, *Water Sci. Tech.* **71** (2015), 1524–1535.

[51] E. Torfs, M.C. Martí, F. Locatelli, S. Balemans, R. Bürger, S. Diehl, J. Laurent, P.A. Vanrolleghem, P. François, and I. Nopens, Concentration-driven models revisited: towards a unified framework to model settling tanks in water resource recovery facilities, *Water Sci. Tech.* **75** (2017), 539—51.

[52] E. Torfs, S. Balemans, F. Locatelli, S. Diehl, R. Bürger, J. Laurent, P. François, and I. Nopens, On constitutive functions for hindered settling velocity in 1-D settler models: Selection of appropriate model structure, *Water Res.* **110** (2017), 38–47.

[53] R. Bürger, J. Careaga, and S. Diehl, Entropy solutions of a scalar conservation law modeling sedimentation in vessels with varying cross-sectional area, *SIAM J. Appl. Math.* **77** (2017), 789–811.

[54] R. Bürger, J. Careaga, and S. Diehl, Flux identification of scalar conservation laws from sedimentation in a cone, *IMA J. Appl. Math.* **83** (2018), 526–552.

[55] G. Anestis, *Eine eindimensionale Theorie der Sedimentation in Absetzbehältern veränderlichen Querschnitts und in Zentrifugen*, PhD Thesis, TU Vienna, Austria, 1981.

[56] L.C. Evans, *Partial Differential Equations*, Second Printing, American Mathematical Society, Providence, RI, USA, 2002.

[57] H. Holden and N.H. Risebro, *Front Tracking for Hyperbolic Conservation Laws*, 2nd ed., Springer-Verlag, Berlin, 2015.

[58] S.N. Kružkov, First order quasilinear equations in several independent variables, *Math. USSR Sbornik* **10**, No. 2 (1970), 217–243.

[59] M.G. Crandall and A. Majda, Monotone difference approximations for scalar conservation laws, *Math. Comp.* **34** (1980), 1–21.

[60] R. Bürger and S. Diehl, Convexity-preserving flux identification for scalar conservation laws modelling sedimentation, *Inverse Problems* **29** (2013), paper 045008 (30pp).

[61] D.A. White and N. Verdone, Numerical modelling of sedimentation processes, *Chem. Eng. Sci.* **55** (2000), 2213–2222.

[62] R. Bürger, J. Careaga, S. Diehl, R. Merckel, and J. Zambrano, Estimating the hindered-settling flux function from a batch test in a cone, *Chem. Eng. Sci.* **192** (2018), 244–253.

[63] R. Bürger, R. Donat, P. Mulet, and C.A. Vega, Hyperbolicity analysis of polydisperse sedimentation models via a secular equation for the flux Jacobian, *SIAM J. Appl. Math.* **70** (2010), 2186–2213.

[64] R. Bürger, K.H. Karlsen, E.M. Tory, and W.L. Wendland, Model equations and instability regions for the sedimentation of polydisperse suspensions of spheres, *ZAMM Z. Angew. Math. Mech.* **82** (2002), 699–722.

[65] S. Berres, R. Bürger, and E.M. Tory, Applications of polydisperse sedimentation models, *Chem. Eng. J.* **111** (2005), 105–117.

[66] L.A. Amy, P.J. Talling, V.O. Edmonds, E.J. Sumner, and A. Lesueur, An experimental investigation od sand-mud suspension settling behaviour: implications for bimodal mud contents of submarine flow deposits, *Sedimentology* **53** (2006), 1411–1434.

[67] R.M. Dorrell, A.J. Hogg, and D. Pritchard, Polydisperse suspensions: erosion, deposition, and flow capacity, *J. Geophys. Res.* **118** (2013), 1939–1955.

[68] R. Dorrell, A.J. Hogg, E.J. Sumner, and P.J. Talling, The structure of the deposit produced by sedimentation of polydisperse suspensions, *J. Geophys. Res.* **116** (2011), paper F01024.

[69] R. Simura and K. Ozawa, Mechanism of crystal redistribution in a sheet-like magma body: Constraints from the Nosappumisaki and other Shoshonite intrusions in the Nemuro prenisula, Northern Japan, *J. Petrology* **47** (2006), 1809–1851.

[70] A. Abeynaike, A.J. Sederman, Y. Khan, M.L. Johns, J.F. Davidson, and M.R. Mackley, The experimental measurement and modelling of sedimentation and creaming for glycerol/biodiesel droplet dispersions, *Chem. Eng. Sci.* **79** (2012), 125–137.

[71] S. Qian, R. Bürger, and H.H. Bau, Analysis of sedimentation biodetectors, *Chem. Eng. Sci.* **60** (2005), 2585–2598.

[72] B.H. Kim and M.S. Klima, Development and application of a dynmaic model for hindered-settling column separations, *Minerals Eng.* **17** (2004), 403–410.

[73] W.K. Sartory, Three-component analysis of blood sedimentation by the method of characteristics, *Math. Biosci.* **33** (1977), 145–165.

[74] M. Gray, Z. Xu, and J. Masliyah, Physics in the oil sands of Alberta, *Physics Today* **62** (2009), No. 3, 31–35.

[75] R. Bürger, S. Diehl, M.C. Martí, P. Mulet, I. Nopens, E. Torfs, and P.A. Vanrolleghem, Numerical solution of a multi-class model for batch settling in water resource recovery facilities, *Appl. Math. Modelling* **49** (2017), 415–436.

[76] E.B. Shin, H.S. Yoon, Y.D. Lee, Y.S. Pae, S.W. Hong, and B.H. Joo, The effects of particle size distribution on the settleability of CSO pollutants, *Wat. Sci. Tech.* **43** (5) (2001), 103–110.

[77] R. Bürger, R. Donat, P. Mulet, and C.A. Vega, On the hyperbolicity of certain models of polydisperse sedimentation, *Math. Meth. Appl. Sci.* **35** (2012), 723–744.

[78] R. Bürger, R. Donat, P. Mulet, and C.A. Vega, On the implementation of WENO schemes for a class of polydisperse sedimentation models, *J. Comput. Phys.* **230** (2011), 2322–2344.

[79] R. Bürger, J. Careaga, S. Diehl, C. Mejías, and R. Ruiz-Baier, 'Convection-diffusion-reaction and transport-flow problems motivated by models of sedimentation: some recent advances'. In: B. Sirakov, P. N. de Souza and M. Viana (eds.), *Proceedings of the International Congress of Mathematicians, Rio de Janeiro 2018, Vol. IV: Invited Lectures*, World Scientific, Singapore, 3489–3514 (2018).

[80] J.H. Masliyah, Hindered settling in a multiple-species particle system, *Chem. Eng. Sci.* **34** (1979), 1166–1168.

[81] M.J. Lockett and K.S. Bassoon, Sedimentation of binary particle mixtures, *Powder Technol.* **24** (1979), 1–7.

[82] W. Schneider, G. Anestis, and U. Schaflinger, Sediment composition due to settling of particles of different sizes, *Int. J. Multiphase Flow* **11** (1985), 419–423.

[83] S. Benzoni-Gavage and R.M. Colombo, An n-populations model for traffic flow, *Eur. J. Appl. Math.* **14** (2003), 587–612.

[84] S. Boscarino, R. Bürger, P. Mulet, G. Russo, and L.M. Villada, Linearly implicit IMEX Runge-Kutta methods for a class of degenerate convection-diffusion problems, *SIAM J. Sci. Comput.* **37** (2015), B305–B331.

[85] S. Boscarino, R. Bürger, P. Mulet, G. Russo, and L.M. Villada, On linearly implicit IMEX Runge-Kutta Methods for degenerate convection-diffusion problems modelling polydisperse sedimentation, *Bull. Braz. Math. Soc. (N. S.)* **47** (2016), 171–185.

[86] J. Anderson, A secular equation for the eigenvalues of a diagonal matrix perturbation, *Linear Algebra Appl.* **246** (1996), 49–70.

[87] R. Donat and P. Mulet, A secular equation for the Jacobian matrix of certain multi-species kinematic flow models, *Numer. Methods Partial Differential Equations* **26** (2010), 159–175.

[88] G.S. Jiang and C.-W. Shu, Efficient implementation of Weighted ENO schemes, *J. Comput. Phys.* **126** (1996), 202–228.

[89] X.-D. Liu, S. Osher, and T. Chan, Weighted essentially non-oscillatory schemes, *J. Comput. Phys.* **115** (1994), 200–212.

[90] C.-W. Shu, High order weighted essentially nonoscillatory schemes for convection dominated problems, *SIAM Rev.* **51** (2009), 82–126.

[91] Y.-T. Zhang and C.-W. Shu, ENO and WENO schemes, Chapter 5 in R. Abgrall and C.-W. Shu (eds.), *Handbook of Numerical Methods for Hyperbolic Problems: Basic and Fundamental Issues*. Handbook of Numerical Analysis vol. 17, North Holland, (2016), 103–122.

[92] G.K. Batchelor and R.W. Janse van Rensburg, Structure formation in bidisperse sedimentation, *J. Fluid Mech.* **166** (1986), 379–407.

[93] G.K. Batchelor and C.S. Wen, Sedimentation in a dilute polydisperse system of interacting spheres. Part 2. Numerical results, *J. Fluid Mech.* **124** (1982), 495–528.

[94] R.H. Davis and H. Gecol, Hindered settling function with no empirical parameters for polydisperse suspensions, *AIChE J.* **40** (1994), 570–575.

[95] C.-W. Shu and S. Osher, Efficient implementation of essentially non-oscillatory shock capturing schemes, *J. Comput. Phys.* **77** (1988), 439–471.

[96] R. Bürger, P. Mulet and L.M. Villada, Spectral WENO schemes with Adaptive Mesh Refinement for models of polydisperse sedimentation, *ZAMM Z. Angew. Math. Mech.* **93** (2013), 373–386.

[97] R. Bürger, P. Mulet and L.M. Villada, Regularized nonlinear solvers for IMEX methods applied to diffusively corrected multispecies kinematic flow models, *SIAM J. Sci. Comput.* **35** (2013), B751–B777.

[98] L. Pareschi and G. Russo, Implicit-explicit Runge-Kutta schemes and applications to hyperbolic systems with relaxation, *J. Sci. Comput.* **25** (2005), 129–155.

[99] U.M. Ascher, S.J. Ruuth, and R.J. Spiteri, Implicit-explicit Runge-Kutta methods for time-dependent partial differential equations, *Appl. Numer. Math.* **25** (1997), 151–167.

[100] S. Boscarino, P.G. Le Floch, and G. Russo, High-order asymptotic-preserving methods for fully nonlinear relaxation problems, *SIAM J. Sci. Comput.* **36** (2014), A377–A395.

[101] A. Kurganov and E. Tadmor, New high-resolution central schemes for nonlinear conservation laws and convection-diffusion equations, *J. Comput. Phys.* **160** (2000), 241–282.

[102] E.D. Fernández-Nieto, E.H. Koné, T. Morales de Luna, and R. Bürger, A multilayer shallow water system for polydisperse sedimentation, *J. Comput. Phys.* **238** (2013), 281–314.

[103] R. Bürger, E.D. Fernández-Nieto, and V. Osores, A dynamic multilayer shallow water model for polydisperse sedimentation, *ESAIM: Math. Model. Numer. Anal.* **53** (2019), 1391–1432.

[104] E. Audusse and M.-O. Bristeau, Finite-volume solvers for a multilayer Saint-Venant system, *Int. J. Appl. Math. Comput. Sci.* **17** (2007), 311–319.

[105] E. Audusse, M.-O. Bristeau, M. Pelanti, and J. Sainte-Marie, Approximation of the hydrostatic Navier-Stokes system for density stratified flows by a multilayer model: kinetic interpretation and numerical solution, *J. Comput. Phys.* **230** (2011), 3453–3478.

[106] J. Sainte-Marie, Vertically averaged models for the free surface non-hydrostatic Euler system: derivation and kinetic interpretation, *Math. Models Methods Appl. Sci.* **21** (2011), pp. 459–490.

[107] E. Audusse, A multilayer Saint-Venant model: derivation and numerical validation, *Discrete Contin. Dyn. Syst. Ser. B* n **5** (2005), 189–214.

[108] V.S. Patwardhan and C. Tien, Sedimentation and liquid fluidization of solid particles of different sizes and densities, *Chem. Eng. Sci.* **40** (1985), 1051–1060.

[109] G.C.K. Wong and S.C.K. Wong, A multi-class traffic flow model—an extension of LWR model with heterogeneous drivers, *Transp. Res. A* **36** (2002), 827–841.

[110] R. Bürger, H. Torres, and C.A. Vega, An entropy stable scheme for the multiclass Lighthill-Whitham-Richards traffic model, *Adv. Appl. Math. Mech.* **11** (2019), 1022–1047.